INFORMATION TO USERS

This material was produced from a microfilm copy of the original document. While the most advanced technological means to photograph and reproduce this document have been used, the quality is heavily dependent upon the quality of the original submitted.

The following explanation of techniques is provided to help you understand markings or patterns which may appear on this reproduction.

1. The sign or "target" for pages apparently lacking from the document photographed is "Missing Page(s)". If it was possible to obtain the missing page(s) or section, they are spliced into the film along with adjacent pages. This may have necessitated cutting thru an image and duplicating adjacent pages to insure you complete continuity.

2. When an image on the film is obliterated with a large round black mark, it is an indication that the photographer suspected that the copy may have moved during exposure and thus cause a blurred image. You will find a good image of the page in the adjacent frame.

3. When a map, drawing or chart, etc., was part of the material being photographed the photographer followed a definite method in "sectioning" the material. It is customary to begin photoing at the upper left hand corner of a large sheet and to continue photoing from left to right in equal sections with a small overlap. If necessary, sectioning is continued again — beginning below the first row and continuing on until complete.

4. The majority of users indicate that the textual content is of greatest value, however, a somewhat higher quality reproduction could be made from "photographs" if essential to the understanding of the dissertation. Silver prints of "photographs" may be ordered at additional charge by writing the Order Department, giving the catalog number, title, author and specific pages you wish reproduced.

5. PLEASE NOTE: Some pages may have indistinct print. Filmed as received.

Xerox University Microfilms
300 North Zeeb Road
Ann Arbor, Michigan 48106

MULTIPARTICLE LOW REYNOLDS NUMBER FLOW WITH BIORHEOLOGICAL APPLICATIONS

by

SAM LEICHTBERG

A dissertation submitted to the Graduate Faculty in Engineering in partial fulfillment of the requirements for the degree of Doctor of Philosophy, The City University of New York.

1975

This manuscript has been read and accepted for the Graduate Faculty in Engineering in satisfaction of the dissertation requirement for the degree of Doctor of Philosophy.

5/21/75
date

Sheldon Weinbaum
Chairman of Examining Committee

5/22/75
date

Jacques E. Benveniste
Executive Officer

Michael J. Gluckman

Thomas A. Hewett

Robert Pfeffer

Sheldon Weinbaum, Chairman

Supervisory Committee

The City University of New York

DEDICATION

This thesis is dedicated to my wonderful wife, Judy, whose help and encouragement made this achievement possible, and whose patience, love and understanding made the transit bearable.

ABSTRACT

MULTIPARTICLE LOW REYNOLDS NUMBER FLOW
WITH BIORHEOLOGICAL APPLICATIONS

by

Sam Leichtberg

Adviser: Professor Sheldon Weinbaum
Co-Adviser: Professor Robert Pfeffer

This thesis deals with the axisymmetric creeping motion of finite chains of spheres in infinite as well as in bounded media, and offers a strong theoretical application to blood flow in the microcirculation.

Time-dependent motions of chains containing three or more spheres in an infinite medium are presented, demonstrating the lack of a stable steady-state configuration for such chains due to the continually changing multiparticle interactions. The relative magnitudes of the forces relating to particle acceleration are examined. The Basset force is found to be the most important of the unsteady forces, casting a significant influence on the long-time-scale transient motion. A critical initial-spacing criterion for the near approach of spheres is discovered. The theoretical time-dependent predictions compare very favorably with experimental data.

Quasi-steady state drag and velocity calculations, as well as correlations for wall correction factors, are presented for multiparticle Stokès flow inside a long cylindrical tube. The results demonstrate the interparticle interaction effects, the sphere-wall interactions, and the effects of wall damping on the interparticle shielding phenomenon. An exact description

of time-dependent motion in a bounded medium is not attempted, due to practical limitations imposed by computer execution times. Instead, a first-order approximation is investigated: the zero-drag motion of a chain of spheres in an unbounded Poiseuille flow. The qualitative conclusions drawn from all the problems considered in this thesis are drawn together to predict a new hydrodynamical mechanism for the formation of rouleaux of red blood cells in the microcirculation. This theory predicts that individual red cells in finite chains of identical cells travel at different velocities, approaching each other closely enough for short-range forces to dominate.

ACKNOWLEDGEMENT

I wish to thank Professor Sheldon Weinbaum and Professor Robert Pfeffer for their continuous guidance and their many contributions in directing this research.

This research was supported by the National Science Foundation, Grant no. GK-40802. In addition, I was supported for one year by an NDEA Title IV Graduate Fellowship. These are gratefully acknowledged.

TABLE OF CONTENTS

LIST OF TABLES

LIST OF FIGURES

Figure | page

CHAPTER III

CHAPTER IV

CHAPTER V

NOMENCLATURE

$A(\lambda)$	arbitrary function
a	sphere radius
B_{nj}	arbitrary constant
$B(\lambda)$	arbitrary function
b	center-to-center spacing of trailing doublet, in sphere diameters
c	center-to-center spacing of leading doublet, in sphere diameters
D,d	inter-sphere spacing
D_{nj}	arbitrary constant
ds	differential surface element
E^2	Stokesian linear differential operator
F	force
F_D, F_{VM}, F_B	viscous drag, virtual mass and Basset forces
$F_n(z)$	a known function
$G_{nj}^{(k)}(\lambda)$	a known function
g	acceleration of gravity
$H(\lambda)$, $h_i^{(k)}(R,\lambda)$	known functions
h_k	metrical coefficient
I_o, I_1	modified Bessel functions of the first kind
$\vec{i}_k$	unit vector
j	sphere number
K_o, K_1	modified Bessel functions of the second kind
k_I, k_{II}, k_{III}	wall correction factors for 1,2,3 spheres
L	length
M	order of truncation; number of boundary points per sphere
N	number of spheres in a chain
n	order of multipole

$P_n(x)$	Legendre polynomial
p	pressure
Q	flow discharge rate
R, r, r_j	cylindrical, spherical and relative-spherical radial coordinates
R_o	tube radius
Re, Re_∞	Reynolds number
$S_{nj}^{(k)}(R,z)$, $T_{nj}^{(k)}(R,z)$	known functions
t	time
t^*	short initial time scale
U	sphere velocity
U_t	terminal settling velocity of an isolated sphere
U_I, U_{II}	terminal settling velocity of one and two spheres in a bounded medium; with ∞ $(U_{I\infty}, U_{II\infty})$ in an unbounded medium
V, v	fluid velocity field
V, V_o	centerline fluid velocity of undisturbed Poiseuille flow
z	axial coordinate
z_j	relative axial coordinate, z-jd
α	angle, or known function
β, γ	known functions
ϵ	error
ζ	$\cos\theta$
θ, θ_j	circumferential and relative-circumferential spherical coordinates
λ	drag correction factor, or variable of integration
μ	fluid viscosity
ν	fluid kinematic viscosity
ξ	known function

δ	density
$T(\lambda)$	known function
τ	time
$\Phi(\lambda)$	known function
ϕ	velocity potential, or known function
ψ	stream function
ω	frequency
$\mathcal{Y}_N(x)$	Gegenbauer function of order n, degree $-\frac{1}{2}$

Superscripts

U	relating to the motion of a sphere in a bounded quiescent fluid
V	relating to the Poiseuille flow past a stationary sphere
~	Chapter II - dimensionless variable
~	Chapter III - dimensional variable

CHAPTER I

INTRODUCTION

Multiparticle flows in the presence of body forces and hydrodynamic interparticle interactions have important applications in bio-mechanical and technological suspension studies.

The present study investigates the quasi-steady and time-dependent creeping flows past finite chains of identical spheres in infinite and bounded media. In the cases of spheres falling along their line of centers and of neutrally-buoyant spheres moving along the centerline of an otherwise-parabolic velocity profile (Poiseuille flow), chains of three or more spheres are shown to translate in an unstable manner. Different spheres in the chain move with different velocities. Therefore, such chains have no stable steady state configuration since the quasi-steady state Stokes drag on each sphere continues to vary because of multi-particle interaction effects that continually change as a function of particle spacing and velocity.

The unequal hydrodynamic interactions are shown to exert a significant influence on the inter-particle relative velocities in infinite media as well as in cylindrically bounded flows in which the tube diameter exceeds twice the particle size. These results are used to postulate a new hydrodynamical mechanism which helps explain the long-range forces which operate in the microcirculation to form rouleaux, or axial trains, of nearly-contiguous red blood cells.

This thesis is presented in the form of three independent papers each of which will be submitted for publication in a scientific journal. Each of the three main chapters (II, III, IV), therefore, has its own abstract, introduction, reference list and page numbering.

Some of the research for chapter II had been conducted earlier by Professor M.J. Gluckman, particularly the work pertaining to section II-3.B. It is included in this thesis for the sake of completeness.

CHAPTER II

A STUDY OF UNSTEADY FORCES AT LOW REYNOLDS NUMBER: A STRONG INTERACTION THEORY FOR THE COAXIAL SETTLING OF THREE OR MORE SPHERES

Abstract

Unsteady multiparticle creeping motions are complicated by the appearance of Basset, virtual mass and acceleration forces and by the difficulty of calculating fluid-particle interactions for three or more closely spaced particles. The present theoretical and experimental investigation explores the importance of each of these complicating features by examining in detail the gravitational-hydrodynamic interaction between three or more spheres falling along a common axis. The strong interaction theory developed to describe this motion accurately satisfies the viscous boundary conditions along the surface of each sphere and includes all the unsteady force terms in the equations of motion for the spheres. The experimental measurements for the three sphere chain are in excellent agreement with theoretical predictions provided the Basset force is retained in the dynamic force balance. These results indicate, in general, that the Basset force is the most important unsteady force in gravitational flows at low Reynolds numbers in which the flow configuration is slowly changing due to fluid-particle interactions. The unsteady theory for small but finite Reynolds numbers shows that lowest order departures from the flow configuration predicted by quasi-steady zero Reynolds number theory will occur due to the integrated effect of the Basset force if the duration of the interaction is of $O(Re_\infty^{-\frac{1}{2}}\ a/U_t)$ or longer, where Re_∞ is based on the terminal settling velocity U_t and radius a of the sphere. This condition is satisfied in most sedimentation problems of interest. Virtual mass and particle acceleration forces, on the other hand, are of negligible importance except for a short-lived initial transient period. An intriguing new feature of the three-sphere motion for large times was discovered. One finds that there is a critical initial

spacing criterion which determines whether the two leading spheres in the chain will asymptotically approach a zero or a finite fluid gap as time goes to infinity. Numerical solutions for longer chains show that there is a tendency for the leading third of the chain to break up into doublets and triplets whereas the spheres in the latter third of the chain tend to space out separately.

1. Introduction

The motion of particles at low Reynolds number through fluid media under the action of gravitational forces, hydrodynamic interactions, or a combination of both, is important in the mechanics of aerosols and suspensions, and various bio-mechanical applications, e.g., the axial clustering of red blood cells in the microcirculation, Leichtberg, Weinbaum and Pfeffer (1975). Efficiencies of spray scrubber devices, settling velocities of suspensions, and agglomeration rates of aerosol particles in the atmosphere all depend on the relative motion of suspension particles.

Existing theoretical analyses of the behavior of finite clusters of particles in unbounded creeping flow have been confined largely to various two sphere configurations or larger dilute systems where particle interactions are weak.

The stimulus for much of the work on two spheres is the well known exact solution by Stimson and Jeffery (1926) for two identical spheres translating along their line of centers. This exact solution involves mapping the single sphere solution into spherical bipolar coordinates, a technique which was later extended to a variety of other two body configurations by other authors. Experimental investigations of the two-sphere problem by Bart (1959) and Happel and Pfeffer (1960) have shown excellent agreement with the theoretical results at low Reynolds numbers ($Re < 0.1$).

The related problem of the interaction of three or more spheres has received much less attention. One interesting study is that of Hocking (1964) for three spheres falling side by side. The analysis is based on a quasi-steady first order reflection theory and thus most accurate for large sphere spacings. The fundamental difference between particle interactions involving two

and three or more identical spheres is that the two sphere problem at very low Re is a constant flow configuration in which the sphere spacing does not change, since the Stokes quasi-steady state drag on each sphere is the same. In contrast, three or more spheres have no steady state configuration since the quasi-steady state Stokes drag on each sphere continues to vary because multiparticle interaction effects continually change as a function of particle spacing and velocity.

Perhaps the simplest three-sphere strong interaction problem that can be examined both theoretically and experimentally is the axial settling of three identical spheres in a gravitational field. Because of its simplicity the coaxial three sphere configuration affords a convenient comparison between theory and experiment in which the unsteady effects of the virtual mass and Basset forces can be carefully examined over a long time scale with large particle displacements. The theoretical and experimental results presented in this investigation are, to the authors' knowledge, the first carefully documented confirmation of the presence of the Basset force effect. These results show that for slowly changing multiparticle gravitational motions the Basset force is the most important inertial effect at low but nonzero Reynolds numbers.

The qualitative behavior of the coaxial three-sphere problem with an initial configuration as shown in Figure 1a was first investigated experimentally by Happel and Pfeffer (1960). They observed that if three spheres were released from rest, 1 and 2 would fall as a doublet initially and thus travel at a velocity that Stokes theory predicts would be 55 percent greater than the settling velocity of an isolated sphere of the same diameter. The flow configuration shown in Figure 1a, therefore, does not persist.

As spheres 1 and 2 approach sphere 3, sphere 2 starts to accelerate due to its combined interaction with spheres 1 and 3, as shown in Figure 1b. Finally, as sphere 2 approaches sphere 3, 2 and 3 form a doublet which continues to move away from sphere 1, Figure 1c, as long as the spheres are allowed to settle without approaching or impinging on any boundaries. An intriguing new facet of the three-sphere interaction problem that was discovered during the course of the present investigation is the "critical initial spacing" condition described in section 7. One finds that the gap between the two leading spheres of three-sphere and longer chains can asymptote with time either to zero or to some finite non-zero gap, depending on the initial configuration. A "critical spacing" curve separates the sets of initial configurations which produce these two different asymptotic behaviors.

In principal the quasi-steady state Stokes drag on a sphere in strong interaction can be determined by one of several approaches: the method of reflections, finite element methods, or the boundary method used in this work. The method of reflections, developed by Smoluchowski (1911) and used widely by others, is most satisfactory for weak interactions in which only a single reflection from each boundary is required. The method converges very slowly for close sphere spacings and is very laborious to apply when multiple reflections from more than two solid bodies are considered. Several investigators have recently applied finite-element methods to multiparticle slow flows. For example, Skalak, Chen and Chien (1972) have used the method to model capillary blood flow. The red cells are simulated by bi-concave disk-shaped solid particles which are equally spaced and axi-symmetrically located in a circular tube. This method is a very promising technique for studying irregular but identical particles

with periodic spacing, but it cannot be applied in its present form to transient interaction problems or to steady flow problems with non-periodic particle boundary conditions.

Of the three methods the one that offers the greatest flexibility, ease of application, and accuracy for treating closely spaced multiparticle flows is the discrete point boundary method developed in Gluckman, Pfeffer and Weinbaum (1971) and Gluckman, Weinbaum and Pfeffer (1972). In Gluckman, Pfeffer and Weinbaum (1971) it is shown that the disturbances due to each submerged sphere or spheroid in an arbitrary coaxial distribution of spheres or spheroids can be exactly represented by an infinite series of multilobular disturbances, or multipoles, located at the origin of each object. These disturbances are described by the simply separable singular solutions of the axisymmetric Stokes equation written in a local spherical or spheroidal coordinate system corresponding to the surface of each object. Solutions to any degree of accuracy can be obtained depending on the order of truncation or number of multipoles retained in the solution. Since the method is one of truncation rather than iteration, in which all particles are treated simultaneously for interactions of any order, the solution procedure converges extremely rapidly and provides good drag estimates even for the lowest order truncation. For example, in the most extreme case of two spheres touching, the first, third and fifth order truncation solutions yield an approximation for the drag on each sphere which is within 2.5 percent, 0.14 percent and 0.001 percent of the exact solution, respectively. In Gluckman, Weinbaum and Pfeffer (1972) this theory is extended to treat the axisymmetric flow past an arbitrary body of revolution.

Section 2 briefly summarizes the dynamic equation of motion for a single sphere, while Section 3 describes how each of the force components must be modified for a multiparticle system. The quasi-steady solutions for axisymmetric creeping flow with particle interaction are presented in Section 4. Section 5 describes the near collision behavior of two spheres that approach each other with a finite relative velocity. The numerical solution of the non-linear dynamic equations of motion is discussed in Section 6. Sections 7 and 8 present the results for three-sphere and longer chains, respectively, which are settling coaxially under the effect of gravity.

2. Formulation of the Dynamic Equations of Motion for a Single Sphere

The momentum equation for unsteady creeping motion is:

$$\frac{\partial \bar{V}}{\partial t} = -\frac{1}{\rho}\nabla p + \nu\nabla^2\bar{V} . \tag{2.1}$$

To eliminate the pressure one takes the curl of (2.1)

$$\frac{\partial(\text{curl } \bar{V})}{\partial t} = \nu\nabla^2(\text{curl } \bar{V}) . \tag{2.2}$$

Landau and Lifshitz (1959) present an elegant analysis of equation (2.2) and solve it for the case of a single sphere moving slowly with velocity U(t) in a viscous fluid. The solution is found by representing the velocity U(t) as a Fourier integral,

$$U(t) = \int_{-\infty}^{\infty} U_\omega e^{-i\omega t}\, d\omega$$

where U_ω is the solution to (2.1) for a sphere oscillating with frequency ω. The expression for the drag force F on the sphere is given in terms of U(t) as

$$F = 6\pi\mu Ua + \frac{2}{3}\pi\rho a^3\frac{dU}{dt} + 6\pi\mu a^2\frac{1}{\sqrt{\pi\nu}}\int_o^t \frac{dU}{d\tau}\frac{d\tau}{\sqrt{t-\tau}} \tag{2.3}$$

Equation (2.3) shows that there are three basic contributions to the drag force on a sphere undergoing an arbitrary slow motion in a viscous fluid. The first term in equation (2.3) represents the steady state component of the drag force, or Stokes drag term due to viscous dissipation. The remaining two terms in (2.3) represent unsteady contributions to the drag force. The first of these two terms is the virtual or hydrodynamic mass contribution. This term is also present for an ideal fluid and is related to the

kinetic energy associated with the fluid that is displaced by the sphere. The last term in equation (2.3) has been identified as the Basset force after Basset (1888), see Brenner (1961). This force is attributed to the unsteady inertial term in (2.1); its importance will be discussed in greater detail in Section 7.

The complete equation of motion for the unsteady settling of a single sphere at low Re in an unbounded viscous fluid is obtained by adding the static or gravity forces to the three dynamic forces in (2.3) and equating these forces to the acceleration force of the sphere.

$$M \frac{dU}{dt} = Mg - M'g - F_D - F_{VM} - F_B, \tag{2.4}$$

where M = mass of sphere = $\frac{4}{3}\pi a^3 \rho_s$,

M' = mass of displaced fluid = $\frac{4}{3}\pi a^3 \rho$,

F_D = Stokes drag force = $6\pi\mu a U$,

F_{VM} = retarding virtual mass force due to the energy of the displaced fluid,

F_B = Basset force,

a = sphere radius,

ρ_s = sphere density,

ρ = fluid density,

μ = fluid viscosity,

ν = fluid kinematic viscosity = μ/ρ.

The simple summation of forces (2.4) is strictly valid only in the limit as Re approaches zero where the governing equation (2.1) is linear. For a single sphere, (2.4) can be written as follows:

$$\frac{4}{3}\pi a^3 \rho_s \frac{dU}{dt} = \frac{4}{3}\pi a^3 (\rho_s - \rho) g - 6\pi\mu U a - \frac{2}{3}\pi a^3 \rho \frac{dU}{dt} - 6\pi\mu a^2 \frac{1}{\sqrt{\pi\nu}} \int_0^t \frac{dU}{d\tau} \frac{d\tau}{\sqrt{t-\tau}} . \tag{2.5}$$

The terminal settling velocity U_t is found from (2.5) by setting $dU/dt = 0$,

$$U_t = \frac{2a^2(\rho_s-\rho)g}{9\mu} \tag{2.6}$$

In order to determine the relative magnitude of each of the terms appearing in (2.5) all the variables will be made dimensionless by introducing characteristic reference quantities. Denoting dimensionless variables by a tilda,

$$\tilde{U} = \frac{U}{U_t}$$

$$\tilde{t} = \frac{tU_t}{a} \tag{2.7}$$

$$\tilde{\rho} = \frac{\rho_s}{\rho} \ ,$$

and substituting in (2.5) one obtains,

$$Re_\infty(\tilde{\rho}+\tfrac{1}{2})\frac{d\tilde{U}}{d\tilde{t}} = 9(1-\tilde{U}) - \frac{9Re_\infty^{\frac{1}{2}}}{\sqrt{2\pi}}\int_0^{\tilde{t}}\frac{d\tilde{U}}{d\tilde{\tau}}\frac{d\tilde{\tau}}{\sqrt{\tilde{t}-\tilde{\tau}}} \tag{2.8}$$

where

$$Re_\infty = \frac{2aU_t}{\nu} = \frac{2a^2}{\nu}\Big/\frac{a}{U_t} \tag{2.9}$$

is the Reynolds number based on the sphere's diameter and terminal settling velocity.

The Reynolds number defined in (2.9) represents the ratio of two characteristic reference times, a molecular diffusion time a^2/ν, and a macroscopic time a/U_t characterizing the hydrodynamic-gravitational interaction. One, therefore, suspects that when $Re_\infty << 1$

there are two time scales in the proplem of spheres which start falling from rest. On the longer time scale $\tilde{t}$ defined in (2.7), whose dimensional characteristic time is a/U_t, the unsteady terms in (2.8) are higher order in Re_∞. To lowest order in an expansion of $\tilde{U}$, $\tilde{U} = \tilde{U}_o + Re_\infty^{\frac{1}{2}}\tilde{U}_1 + Re_\infty \tilde{U}_2$, equation (2.8) reduces to the steady state equation

$$\tilde{U}_o = 1. \tag{2.10}$$

For a single isolated sphere a constant settling velocity is achieved since in the absence of other boundaries the flow geometry is constant. The Stokes drag asymptotically approaches a constant value. Since $d\tilde{U}_o/d\tilde{t} = 0$, one finds to $0(Re_\infty^{\frac{1}{2}})$ that $\tilde{U}_1$ is zero. In contrast, as we shall discuss in Section 4, the solution for $\tilde{U}_o$ is not constant if three or more spheres are present since hydrodynamic interactions slowly change the sphere spacing and settling velocity as the motion progresses. The fascinating observation whose implications have not been studied before is that on the long time scale over which these hydrodynamic interactions occur, the Basset force term which is $0(Re_\infty^{\frac{1}{2}})$ dominates over both the inertial and virtual-mass terms which are $0(Re_\infty)$ in equation (2.8).

One can also show that on this long time scale, the convective $\vec{V}\cdot\nabla\vec{V}$ term in the Navier-Stokes equation is $0(Re)$ by comparison with the viscous and pressure terms, and thus may also be neglected in comparison with the Basset force to $0(Re_\infty^{\frac{1}{2}})$. The coaxial settling of three spheres thus provides a simple convenient experiment in which the presence of the Basset force can be experimentally verified and theoretically examined over a long time scale.

It is evident that (2.10) can not satisfy the initial condition, $\tilde{U} = 0$, and that a shorter time scale $t^* << \tilde{t}$ must exist, representing the initial period of rapid acceleration $d\tilde{U}/d\tilde{t} >> 0(1)$,

during which the spheres attain their quasi-steady settling velocity. Inspection of (2.8) suggests that we define this short time scale by

$$t^* = Re_\infty^{-1}\, \tilde{t} \ . \tag{2.11}$$

Substituting (2.11) in (2.8) one obtains

$$(\tilde{\rho} + \frac{1}{2})\, \frac{d\tilde{U}}{dt^*} = 9(1-\tilde{U}) - \frac{9}{\sqrt{2\pi}} \int_o^{t^*} \frac{d\tilde{U}}{dt^*}\, \frac{dt^*}{\sqrt{t^*-\tau^*}} \ . \tag{2.12}$$

One observes that all terms in (2.12) are $0(1)$ and must be retained. On the other hand, the non-linear $\vec{V}\cdot\nabla\vec{V}$ term in the Navier-Stokes equation is $0(Re)$ smaller than the viscous and unsteady inertia terms on this shorter time scale. It is therefore consistent to neglect convective inertial effects while retaining the unsteady inertial, virtual-mass and Basset forces in (2.12). Experimentally, the importance of the Basset force is difficult to isolate on this time scale since the initial transient phase is short lived and the other unsteady forces are of the same order.

3. Correction of the Dynamic Forces

In order to apply (2.5) to a low Re flow system with three or more spheres, each of the dynamic force contributions must be modified to take into account particle interaction effects. Each dynamic force correction will be considered separately in the next three subsections.

A. Stokes Drag Force, F_D

The viscous drag term used in the dynamic equations (2.5) and (2.8) is the well-documented Stokes drag force on a single sphere settling in an unbounded viscous fluid for Re $<<$ 1, $F_D = 6\pi\mu aU$. Since the drag force due to viscous dissipation is still proportional to the instantaneous velocity of the test sphere when more than one sphere is present in the system, this expression for the drag force can be simply modified to account for particle interaction effects on the drag force on each sphere by introducing an interaction parameter λ_j defined by

$$F_{D_j} = 6\pi\mu U_j a\lambda_j . \qquad (3.1)$$

λ_j is thus the ratio of the drag on the j^{th} sphere in an assemblage of particles to the drag on a single sphere of the same diameter, and is a function of all the sphere spacings and velocities.

The computation of λ_j has been the subject of extensive work; see, for example, Happel and Brenner (1965) and Gluckman, Pfeffer and Weinbaum (1971). Until recently only two techniques - the method of reflections and the point force method first introduced by Burgers (1938) - have been available for treating multiple particle interaction problems. The latter method is only valid for interactions at large distances, whereas the former solution procedure converges very slowly as the sphere spacing decreases.

The multipole truncation technique for multiple equally spaced coaxial spheres and spheroids developed in Gluckman, Pfeffer and Weinbaum (1971) is, however, ideally suited for this purpose for the reasons stated earlier.

The geometry being considered is shown in Figure 2 for N spheres. The exact solution for the stream function from Gluckman, Pfeffer and Weinbaum (1971) is given by the superposition of N infinite series representing the disturbance produced by each of the N spheres.

$$\psi = \sum_{j=1}^{N} \sum_{n=2}^{\infty} [B_{nj}\, r_j^{-n+1} + D_{nj}\, r_j^{-n+3}]\, \mathcal{J}_n(\zeta_j) \qquad (3.2)$$

where: $\mathcal{J}_n(\zeta_j)$ = Gegenbauer functions of the first kind

where: $\mathcal{J}_n(\zeta_j)$ = Gegenbauer functions of the first kind,

$r_j = [(z-z_j)^2 + R^2]^{\frac{1}{2}}$,

$\zeta_j = \cos\theta_j = (z-z_j)/r_j$,

z_j = z coordinate of center of sphere j,

B_{nj}, D_{nj} = constants.

Each term in the inner summation, termed a multipole, is a fundamental singular solution of the steady creeping motion equation obtained by dropping the unsteady term in equation (2.1) or (2.2). Each fundamental solution contains an amplitude function shown in brackets and a multilobular Gegenbauer function $\mathcal{J}_n(\zeta_j)$. The B_{nj} and D_{nj} coefficients which fix the strength of the multipole are determined by satisfying the no slip boundary conditions over the generating arcs of all spheres simultaneously, i.e.,

$$V_{rj} = U_j \cos\theta_j = \frac{1}{r_j^2 \sin\theta_j} \frac{\partial\psi}{\partial\theta_j}$$

$$V_{\theta j} = U_j \sin\theta_j = \frac{-1}{r_j \sin\theta_j} \frac{\partial\psi}{\partial r_j}, \quad j = 1,2,\ldots,N, \tag{3.3}$$

where the U_j represent the velocities of each sphere.

Differentiation of the stream function with respect to each sphere individually, as required for (3.3), is tedious, as there is a different origin for each sphere and ψ is a function of all the r_j's and θ_j's. For this reason it is simpler to use the cylindrical R-z coordinate system which has common coordinates for all spheres. Since the velocities V_{rj} and $V_{\theta j}$ are orthogonal and in the same plane, all other velocities originating from the same point as V_{rj} and $V_{\theta j}$ and in the same plane must be zero relative to an observer moving with sphere j. In particular, relative to that observer, V_z and V_R must be identically zero, and therefore, with reference to the quiescent fluid at infinity,

$$V_z = \frac{1}{R}\frac{\partial\psi}{\partial R} = U_j$$

$$V_R = -\frac{1}{R}\frac{\partial\psi}{\partial z} = 0 \qquad \text{on } r_j = a;\ j = 1,\ldots,N. \tag{3.4}$$

To satisfy the boundary conditions (3.4) exactly along the entire surface of each sphere would require the solution of an infinite array of unknown coefficients. However, solutions to any desired accuracy can be obtained by a uniform truncation of each of the infinite multipole series. The two unknown coefficients in each multipole permit one to satisfy the exact no slip boundary conditions (3.4) at one discrete point on the generating arc of

each sphere. Thus, if a spherical boundary is to be approximated by satisfying conditions (3.4) at M discrete points on its generating arc, M terms are retained in the multipole expansion for each sphere. This results in a set of 2xMxN simultaneous linear algebraic equations for the 2xMxN B_{nj} and D_{nj} unknown coefficients. The equation for any point m on the generating arc of the j^{th} sphere can be represented as follows:

$$v_z = \sum_{q=1}^{N} \sum_{n=2}^{M+1} \left[B'_{nqm} B_{nq} + D'_{nqm} D_{nq} \right] = U_j \qquad (3.5)$$

$$v_R = \sum_{q=1}^{N} \sum_{n=2}^{M+1} \left[B''_{nqm} B_{nq} + D''_{nqm} D_{nq} \right] = 0 \qquad (3.6)$$

$$\left. \begin{array}{l} 1 \le m \le M \\ j = 1, \ldots, N \end{array} \right\}$$

where

$$\begin{aligned} B'_{nqm} &= r_{qm}^{-n-1} P_n(\zeta_{qm}) \\ D'_{nqm} &= r_{qm}^{1-n} \left[P_n(\zeta_{qm}) + 2 \mathcal{J}_n(\zeta_{qm}) \right] \\ B''_{nqm} &= r_{qm}^{-n-1} \left[\frac{(n+1) \mathcal{J}_{n+1}(\zeta_{qm})}{\sin \theta_{qm}} \right] \\ D''_{nqm} &= r_{qm}^{1-n} \left[\frac{(n+1) \mathcal{J}_{n+1}(\zeta_{qm}) - 2 \zeta_{qm} \mathcal{J}_n(\zeta_{qm})}{\sin \theta_{qm}} \right] \end{aligned} \qquad (3.7)$$

The linear matrix of equations described by (3.5) and (3.6) can be solved by any standard matrix reduction technique.

Experience gained in Gluckman, Pfeffer, and Weinbaum (1971) has shown that the most accurate lowest order truncation solution for the viscous drag is obtained by choosing $\theta_j = \pi/2$ since this point controls the projected area of the boundary shape approximating the sphere. Additional points are selected as mirror image

pairs about the line $\theta_j = \pi/2$ in order to preserve the geometric symmetry of the spherical boundary shape about this line. A detailed discussion of the role and importance of the higher order multipoles as well as the convergence properties of the multipole truncation technique is given in this earlier paper.

The correction to the Stokes drag for a sphere in an assemblage (λ_j) is given by:

$$\lambda_j = \frac{D_{2j}}{1.5U_j a} \cdot \tag{3.8}$$

It can be surmised by an examination of (3.5), (3.6) and (3.8) that the λ_j are only functions of the distances between spheres and their relative velocities.

An examination of the λ_j for three spheres moving at the same velocity for various sphere spacings provides the basic physical insight into the qualitative experimental observations of Happel and Pfeffer (1960) shown in Figure 1. In the actual solution of the problem, of course, the different instantaneous values of sphere velocities must be taken into account in computing the instantaneous value of λ_j, and the number of spheres may exceed three. Curves of λ_j versus a spacing parameter b/(b+c) for two values of the overall spacing (b+c) are shown in Figure 3. As (b+c) decreases it can be seen that the λ_j decrease, showing that drag reduction effects increase as the spheres approach one another.

A number of interesting features emerge from an examination of Figure 3. First, the drag on the center sphere is always less than the drag on either of the outer spheres. This is due to the fact that the central sphere is being acted on directly by both outer spheres, whereas an outer sphere is being acted on directly

only by the central sphere and indirectly by the far sphere. This suggests that whatever the starting position of the three spheres, the central sphere will attempt to approach sphere 3. Therefore, one should always move to the right along the b/(b+c) axis as time progresses, due to the lower drag on the central sphere. Finally, it is of interest to note that as spheres 2 and 3 move away from the single sphere 1, λ_1 will approach unity, whereas λ_2 and λ_3 will approach a constant value which depends on the asymptotic spacing c_∞ after sphere 1 has been left far behind.

B. Virtual Mass Term, F_{VM}

Virtual mass has been defined by Darwin (1953) as the mass of fluid to be added to that of the solid in calculating its kinetic energy. Existing calculations of this additional apparent mass, as well as its derivation, have been based on arguments derived from ideal fluid theory. A rigorous treatment for viscous flow has never been presented. Kelvin's theorem of minimum energy states that a given potential flow will have less kinetic energy than any other flow which has the same normal velocity of the boundaries. In light of this theorem, it is especially intriguing that Landau and Lifshitz (1959) show that for the case of a single sphere moving with an arbitrary velocity $\vec{u}(t)$ in a real fluid at zero Re_∞ the virtual mass is identical to that for the given sphere moving in a potential flow with the same velocity. Although not completely valid for interaction problems, this conclusion will be used here and justified

at the end of this subsection in light of the previous order-of-magnitude analysis.

The calculation of the virtual mass for low Re_∞ interaction problems using potential flow theory is still a formidable task because of particle interaction effects, and has not previously been performed for a finite assemblage of more than two spheres, Milne-Thomson (1960). In general, the virtual mass V.M. of an object is given by

$$V.M. = kM' \ , \tag{3.9}$$

where M' is the mass of the fluid displaced by the object and k is a configuration parameter depending on the object shape and the interaction effects that arise from the presence of other boundaries. For a single sphere in an infinite medium, k = 0.5.

One can show using Green's theorem [e.g., p. 89 Milne-Thomson 1960] that when the motion is irrotational the kinetic energy of the fluid can be represented by:

$$T = -(\rho/2)\oint \phi \frac{\partial \phi}{\partial n} dA = -\pi\rho \oint \frac{\psi_p}{r\sin\theta} \frac{\partial \psi_p}{\partial n} ds \tag{3.10}$$

where ϕ = velocity potential,

dn = element of normal drawn into the fluid at the element dA of surface,

ψ_p = stream function in potential flow,

ds = element of integration path along the generating arc of a body of revolution,

and the integral is performed in a clockwise sense about all boundaries. The constant k is found by equating the time rate of change of kinetic

energy of the fluid to the work done by the external force F applied to the moving sphere, i.e.,

$$FU = \frac{dT}{dt} = kM' U \frac{dU}{dt}$$

$$k = \frac{2T}{M'U^2} . \tag{3.11}$$

One now wishes to evaluate the integral (3.10) for the flow kinetic energy for a three sphere system. The governing equation for the stream function in spherical polar coordinates for axially symmetrical potential flow is:

$$\frac{\partial^2 \psi_p}{\partial r^2} + \frac{\sin\theta}{r^2} \frac{\partial}{\partial \theta} \left(\frac{1}{\sin\theta} \frac{\partial \psi_p}{\partial \theta} \right) = 0 \tag{3.12}$$

The general solution to (3.12) is of the form

$$\psi_p = \sum_{n=2}^{\infty} B_n r^{-n+1} \mathcal{J}_n(\cos\theta)$$

The solution for the axisymmetric potential flow for a three sphere system is, therefore,

$$\psi_p = \sum_{j=1}^{3} \sum_{n=2}^{\infty} B_{nj} r_j^{-n+1} \mathcal{J}_n(\cos\theta_j), \tag{3.13}$$

where the r_j and θ_j coordinates are shown in Figure 2. Choosing as a reference a stationary fluid at infinity, the boundary conditions at $r_j = a$ are:

$$V_{rj} = U_j \cos\theta_j = \frac{1}{r_j^2 \sin\theta_j} \frac{\partial \psi_p}{\partial \theta_j} , \quad j=1,2,3. \tag{3.14}$$

The B_{nj} constants (j=1,2,3) occurring in equation (3.13) can be determined using the discrete point boundary method described in the previous subsection. A five-term truncation (n=2,...,6) of the series solution (3.13) which satisfied the normal velocity boundary conditions (3.14) at five points on the generating arc of each sphere was performed for this purpose.

The contribution to the kinetic energy integral (3.10) from each sphere is

$$T_j = \pi\rho\int_o^\pi \frac{a\psi_p}{r_j \sin\theta_j} \frac{\partial\psi_p}{\partial r_j} d\theta_j \,. \tag{3.15}$$

The values of T_j in equation (3.15) have been calculated for various sphere configurations using the aforementioned truncated series solution for ψ_p and the configuration parameters k_j evaluated from equation (3.11)

$$k_j = \frac{1}{\frac{4}{3}\pi a^3 \rho} \frac{2T_j}{U_j^2} \,. \tag{3.16}$$

The values of k_3 determined by the above procedure have been plotted in Figure 4 for the range $1 \le b \le 8$, $1 \le c \le 8$, where b and c are defined in the figure, assuming that all three spheres have the same velocity. This figure indicates that the maximum deviation from a single sphere value $k = \frac{1}{2}$ occurs, as would be expected, when the three spheres are touching. As the distance between spheres 3 and 2 increases, k_3 rapidly asymptotes to the single sphere value of $\frac{1}{2}$. The greatest deviation exhibited by k_3 from the value of $\frac{1}{2}$ is approximately ten percent. This deviation occurs only when spheres 2 and 3 are touching and drops off rapidly to approximately 2% when these spheres are two diameters apart. This exercise demonstrates that in a three sphere system and,

presumably, in systems of more than three spheres, particle interaction effects influence the virtual mass associated with each sphere to a relatively minor extent, even when the spheres are close together. Since the virtual mass forces are higher order in Re_∞ than the Basset force contribution on the long time scale characterizing the important particle interaction effects and are significant only for the short initial period of large accelerations, the values of k_j used were considered to be constant and equal to 1/2. By similar arguments, the assumption of using the potential flow value of 1/2 for Stokes flow is justifiable, although it is not strictly valid for viscous motion of multi-body systems. The errors introduced by these assumptions should be small, while the assumptions themselves allow computing times to be reduced substantially.

C. Basset Force, F_B

The Basset force exerted on a sphere moving with an arbitrary velocity U(t) can be constructed as a superposition integral in which the unit velocity impulsive motion of the sphere is treated as the basic solution. In the basic solution each segment of the solid boundary is treated locally as a Rayleigh problem for the impulsive motion of a flat plate. Unless the boundary continues to accelerate and generate vorticity the Basset force will decay as $1/\sqrt{t}$ during the initial period of acceleration, the total amount of vorticity being conserved but redistributed throughout the flow field. A precise treatment of this force for a multi-particle problem would require that this basic unit solution take into account the instantaneous boundaries of the other spheres. Since the Basset force is a higher order correction of $O(Re_\infty^{1/2})$ on the long time scale of significant interactions, and convective inertia terms of O(Re) have already been neglected in the Navier-Stokes equation, it would seem reasonable to use as a lowest order approximation the unit solution for a

single sphere. The close agreement between theory and experiment presented in Section 7 lends further support to this approximation.

The neglect of the boundaries of the other spheres in the unit solution for the Basset force on the short initial time scale of large accelerations can be argued on similar grounds. From equation (2.11) this time scale is already of 0 (Re $\tilde{t}$). Thus if the inner small time and outer large time solutions are to be valid to the same order in a matched asymptotic sense the use of the unit solution for a single sphere on the short time scale will introduce errors which are higher order than those already included in the model for the long time behavior. Thus, we shall approximate F_{Bj} on both time scales by its expression for a single sphere given in (2.5),

$$F_{Bj} = 6\pi\mu a^2 \frac{1}{\sqrt{\pi\nu}} \int_0^t \frac{dU_j}{d\tau} \frac{d\tau}{\sqrt{t-\tau}} . \tag{3.17}$$

It should be noted however, that although this approximation is valid for motion in an unbounded medium, the effect of an enclosing boundary on the Basset force may be significant, particularly for particles in close proximity to the wall. Transient motions in bounded media should therefore be handled more carefully.

4. Equations of Motion for Three or More Spheres

Based on the discussions presented in Sections 2 and 3, the equation of motion for any sphere j in an N-sphere chain can be represented, using equations (2.8) and (3.1), by

$$Re_\infty(\tilde{\rho}+\tfrac{1}{2})\frac{d\tilde{U}_j}{d\tilde{t}} = 9(1-\tilde{U}_j\lambda_j) - \frac{9Re_\infty^{\frac{1}{2}}}{\sqrt{2\pi}}\int_o^{\tilde{t}}\frac{d\tilde{U}_j}{d\tilde{\tau}}\frac{d\tilde{\tau}}{\sqrt{\tilde{t}-\tilde{\tau}}} \qquad (4.1)$$

$$j = 1,2,\ldots,N.$$

The position of each sphere is obtained by integrating

$$\frac{d\tilde{x}_j}{d\tilde{t}} = \tilde{U}_j \ , \ j = 1,2,\ldots,N, \qquad (4.2)$$

where $\tilde{x}_j$ is a dimensionless length z_j/a, subject to initial conditions based on the initial sphere spacing.

In accord with our previous analysis, sphere interaction effects in the N equations (4.1) are described by the λ_j factors applied to each Stokes drag term, whereas both the virtual mass and Basset forces are approximated by their single sphere expressions. This approximation should be valid to $0(Re_\infty^{\frac{1}{2}})$ on both the short and long time scales.

In the limit $Re_\infty = 0$, equations (4.1) and (4.2) reduce to

$$\tilde{U}_j\lambda_j = 1 \qquad (4.3)$$

$$j = 1,2,\ldots,N.$$

$$\frac{d\tilde{x}_j}{d\tilde{t}} = \frac{1}{\lambda_j} \qquad (4.4)$$

Equation (4.3) which replaces the single-sphere equation (2.10) describes the behavior on the long time scale to lowest order for

small but finite Re_∞. To this order, particle interaction effects contained in λ_j are undergoing changes of order unity.

The equations of motion, equations (4.1) and (4.2) or equations (4.3) and (4.4), were integrated numerically. Before describing the integration procedure and the results, we shall deviate briefly to consider the separate problem of two spheres undergoing a "near" collision in Stokes flow.

5. On the Near-Collision Approach of Two Spheres

The experimental observation of three-sphere chains by Happel and Pfeffer (1960) and the numerical results of the present work for all chains of more than two spheres indicate that the settling velocity of a chain's leading sphere is always exceeded by that of its immediate trailing neighbor, due to the latter's higher level of interaction with the other spheres. Thus, the gap separating the leading doublet monotonically decreases, and, if the initial configuration falls below the "critical spacing" curve in Figure 7, eventually tends to zero as the two spheres head toward an apparent collision.

The equations of motion (4.1) and (4.2) do not permit this impact since the sphere interaction parameter λ_j should approach infinity as the gap width goes to zero. An infinite force is theoretically required to remove the last element of fluid trapped in the narrowing gap, since, at the point of contact, the impact is seen locally as one between two parallel plane walls. Indeed, it is well known that the resistance to the approach of two surfaces is inversely proportional to the gap between them. Since the forces in the problem are bounded, it follows that the gap will tend to zero asymptotically, and that actual contact will not be made in any finite time.

The problem of two spheres approaching each other is identical to the problem of a single sphere falling toward a planar free surface. The exact solution for this problem has been developed by Brenner (1961) using the general bipolar coordinate solution of the creeping motion equation employed by Stimson and Jeffery (1926).

$$\lambda = \frac{4}{3}\sinh\alpha \sum_{n=1}^{\infty} \frac{n(n+1)}{(2n-1)(2n+3)} \left[\frac{4\cosh^2(n+\frac{1}{2})\alpha + (2n+1)^2\sinh^2\alpha}{2\sinh(2n+1)\alpha - (2n+1)\sinh 2\alpha} - 1 \right], \quad (5.1)$$

where $\alpha = \cosh^{-1}(\tilde{c})$

$\tilde{c} = c/a$

$2c$ = the center-to-center spacing between the spheres.

It is seen from (5.1) that as $\tilde{c} \to 1$ the drag force goes to infinity, as expected.

The multipole truncation technique, employed in this paper for calculating drag forces, does not exhibit the desired behavior as $c \to 1$, but predicts instead finite drag forces. Consequently, the numerical experiments show spheres N-1 and N in Figure 2 colliding with a finite relative velocity. This discrepancy in a technique which otherwise gives excellent results is due to the truncation feature in which boundary conditions are satisfied at discrete points rather than continuously on the sphere's generating arc. More specifically, the problem stems from the fact that the coefficient matrix in (3.5) and (3.6) is singular when the front and rear stagnation points are included in the set of boundary-condition points. Consequently, the no-slip conditions cannot be satisfied at the stagnation points, and, as a result, the solution (3.2) describes a zero streamline whose shape, shown in Figure 5, deviates from the spherical near the axis, where two small cusps appear.

It is evident that as $c \to 1$, the problem rapidly changes from the simple discrete point boundary value problem described in Section 3A to a lubrication film problem where the boundary conditions must be satisfied continuously rather than at discrete

points. The present truncation technique cannot detect this change in the nature of the interactive forces since the mathematical objects it describes are cusped. Clearly, the physical arguments relating to the approach of the blunt bodies do not apply to cusped or pointed ones, as these may collide with a finite velocity and a finite force even in creeping flows.

The ratio of the multipole truncation technique drag results to the exact drag (5.1) is plotted versus the dimensionless gap, $c - 1$, for two approaching spheres in Figure 6. In curve 1, boundary conditions were satisfied at nine points equally spaced on the generating arc at $\theta = 18^{\circ}, 36^{\circ}, \ldots, 162^{\circ}$. Twenty-one points were used for curve 2, similarly distributed. One concludes from Figure 6 that the agreement with (5.1) is excellent for large spacings, but breaks down as the gap narrows to about 0.1 diameters when nine points are used and about 0.03 diameters when twenty-one points are used. Both curves asymptote to zero as the gap vanishes and as the exact drag force becomes infinite. The improvement exhibited by curve 2 over curve 1 is attributed to the fact that, with more points on the generating arc, the lowest point moves from $\theta = 18^{\circ}$ in curve 1 to $\theta = 8.2^{\circ}$ in curve 2, thereby reducing the size of the cusp and allowing a closer approach before the solution breaks down.

With this in mind, drag calculations were made with five boundary points on each sphere, but with the first and last points one degree above the centerline, $\theta = 1^{\circ}, 45.5^{\circ}, 90^{\circ}, 134.5^{\circ}, 179^{\circ}$. The result, curve 3 of Figure 6, shows a very marked improvement, with nearly perfect agreement for gaps greater than 0.0005 diameter and a precipitous drop for smaller gaps. Reducing the angle further below 1° was not rewarded with additional accuracy, since the matrix equation given by (3.5)' and (3.6)' becomes ill-conditioned, approaching a singular state as the angle vanishes.

In accordance with the above discussion, the particle velocities calculated in the time-dependent solution are accurate up to a point in time just prior to the erroneously predicted collision. At that point it will be understood that the relative velocity between the two spheres drops rapidly toward zero and that contact can only be made after an infinite time. A similar behavior was reported by Wacholder and Sather (1974) in their theoretical asymptotic solutions for two unequal spheres settling under gravity. They found that as the large sphere catches up to the smaller one the duration of trajectory is infinite, the relative velocity vanishes with the clearance, and the hydrodynamic forces become infinite.

6. Numerical Integration Procedure

The time dependent velocities and trajectories of the N spheres of a given chain were calculated numerically by integrating the equations of motion, equations (4.1) and (4.2) for $0 < Re_\infty << 1$, or (4.3) and (4.4) for $Re_\infty \approx 0$. In either case, the system of 2N equations for $\tilde{U}_1, \tilde{U}_2, \ldots, \tilde{U}_N, \tilde{x}_1, \tilde{x}_2, \ldots, \tilde{x}_N$ is highly non-linear since each of the drag correction factors, λ_j, is a function of these dependent variables, all of which enter into the matrix equation given by equations (3.5) and (3.6).

For the sake of clarity, the integration procedure for the simpler equations (4.3) and (4.4), will be presented first. The initial conditions are set on the sphere spacings, while the initial velocities are calculated as those which satisfy (4.3) at the specified initial configuration. The system cannot be prescribed as starting from rest with $Re_\infty = 0$, since equation (4.3) is incapable of describing the short initial acceleration period.

The sphere velocities at a given time can be calculated from equations (4.3) at any given set of sphere positions or spacings as follows. Combining (4.3) with (3.8) yields

$$D_{2j} = 1.5a \ , \ j = 1,2,\ldots,N, \qquad (6.1)$$

implying that the sphere velocities are such that the viscous drag forces acting on the spheres are all equal and constant with time. This, of course, is not unexpected since in the absence of acceleration related forces the Stokes drag is balanced by the buoyancy force, which is constant and, for identical spheres, equal. If D_{2j} is replaced by (6.1) N times in each of the 2xMxN equations of (3.5) and (3.6), and if the N sphere velocities, $\tilde{U}_j$, are treated as unknowns, then a simple transposition of terms in (3.5) and (3.6) will result in a new set of linear simultaneous algebraic

equations for 2xMxN unknowns ($C_{2j}, \tilde{U}_j, C_{nj}, D_{nj}$, where n=3,4,...,M+1 and j=1,2,...,N), which is solvable by matrix reduction. Thus, the velocities which satisfy (4.3) can be calculated directly, given the configuration, $\tilde{x}_1, \tilde{x}_2, \ldots, \tilde{x}_N$ (which must be known for the evaluation of (3.7)).

The time integration is accomplished by approximating the $\tilde{U}_j(\tilde{t})$ curves as piece-wise linear, that is $d\tilde{U}_j/d\tilde{t}$ is treated as constant over each time interval. Accordingly, consider the k^{th} time step, $\tilde{t}_{k-1} \le \tilde{t} \le \tilde{t}_k$, where $\tilde{t}_k = \tilde{t}_{k-1} + \Delta\tilde{t}_k$, $k \ge 1$, $\tilde{t}_o = 0$, and Δt_k is generally varying with k. The acceleration is assumed constant over the interval

$$\left(\frac{d\tilde{U}_j}{d\tilde{t}}\right)_k = \frac{\tilde{U}_{j,k} - \tilde{U}_{j,k-1}}{\Delta\tilde{t}_k}, \quad j = 1,2,\ldots N, \quad \tilde{t}_{k-1} \le \tilde{t} \le \tilde{t}_k \tag{6.2}$$

Reasonable initial guesses for the $\tilde{U}_{j,k}$ (j=1,2,...,N), the sphere velocities at $\tilde{t} = \tilde{t}_k$, are

$$\tilde{U}_{j,k} = \tilde{U}_{j,k-1} + \left(\frac{d\tilde{U}_j}{d\tilde{t}}\right)_{k-1} \Delta\tilde{t}_k, \quad j = 1,2,\ldots,N. \tag{6.3}$$

These velocities are used to integrate (4.4),

$$\tilde{x}_{j,k} = \tilde{x}_{j,k-1} + \tfrac{1}{2}(\tilde{U}_{j,k} + \tilde{U}_{j,k-1})\Delta\tilde{t}_k, \quad j=1,2,\ldots,N. \tag{6.4}$$

The initial guesses for $\tilde{U}_{j,k}$ can now be improved by solving for the velocities from the matrix equation (3.5) and (3.6) as outlined above, using the latest values of $\tilde{x}_{j,k}$ from (6.4) as parameters. This process is then repeated in an iterative loop,

with alternate improvements on $\tilde{x}_{j,k}$ and $\tilde{U}_{j,k}$ $(j=1,2,\ldots,N)$ by (6.4) and by (6.1) and (3.5), (3.6), respectively, until satisfactory convergence is obtained.

The greatest error present in the above procedure is the one associated with the linearization of the $\tilde{U}_j(\tilde{t})$ curves over the $\Delta\tilde{t}_k$ interval in (6.4). Consequently, following convergence of the iteration procedure, the error's magnitude is estimated by $|\Delta\tilde{x}_j - \Delta\tilde{x}'_j|$, where $\Delta\tilde{x}_j$ is the calculated sphere displacement and $\Delta\tilde{x}'_j$ is an approximate displacement based on a non-zero constant second derivative $d^2\tilde{U}_j/d\tilde{t}^2$. If it is found that the percent error exceeds ϵ, a pre-set error limit, the time interval $\Delta\tilde{t}_k$ is halved and the computations repeated. If, on the other hand, the error is less than 0.1ϵ, $\Delta\tilde{t}$ is doubled $(\Delta\tilde{t}_{k+1} = 2\Delta\tilde{t}_k)$ before proceeding with the computation. In this manner, the time interval is variable, being continually optimized in order to minimize the computing time while maintaining a desired accuracy.

The integration of the more complicated equations (4.1) and (4.2) for $0 < Re_\infty << 1$ follows similar lines. Initial conditions are prescribed on the particle trajectories (initial configuration) as well as on the velocities $(\tilde{U}_{j,0} = 0,\ j=1,2,\ldots,N)$.

Considering the k^{th} time step, one approximates $(d\tilde{U}_j/d\tilde{t})_k$ by (6.2) and writes (4.1) in a finite difference form,

$$\tilde{U}_{j,k} = \frac{1 - \alpha_{j,k} + \beta_{j,k}}{\lambda_{j,k} + \gamma_k}\ , \tag{6.5}$$

or

$$\lambda_{j,k} = \frac{1 - \alpha_{j,k} + \beta_{j,k}}{\tilde{U}_{j,k}} - \gamma_k\ , \tag{6.6}$$

where

$$\alpha_{j,k} = \left(\frac{2Re_\infty}{\pi}\right)^{\frac{1}{2}} \sum_{i=1}^{k-1} \left(\frac{d\tilde{U}_j}{d\tilde{t}}\right)_i \left[(\tilde{t}_k - \tilde{t}_{i-1})^{\frac{1}{2}} - (\tilde{t}_k - \tilde{t}_i)^{\frac{1}{2}}\right]$$

$$\beta_{j,k} = \gamma_k U_{j,k-1}$$

$$\gamma_k = \frac{\frac{1}{9} Re_\infty (\tilde{\rho} + \frac{1}{2}) + (\frac{2}{\pi} Re_\infty \Delta\tilde{t}_k)^{\frac{1}{2}}}{\Delta\tilde{t}_k} .$$

When combined with (3.8), equation (6.6) becomes

$$D_{2j} = 1.5a(1-\alpha_{j,k} + \beta_{j,k}) - 1.5a\gamma_k \tilde{U}_{j,k} , \quad j=1,2,\ldots,N. \qquad (6.7)$$

The relation (6.7) is utilized in the same manner as (6.1) to transform (3.5) and (3.6) into a new matrix equation for the 2xMxN unknowns c_{2j}, $\tilde{U}_j$, c_{nj}, D_{nj} (n=3,4,...,M+1 and j=1,2,...,N). Thus, once more, the set of velocities which satisfies (4.1) can be calculated directly for any given configuration, $\tilde{x}_1, \tilde{x}_2, \ldots, \tilde{x}_N$.

The rest of the procedure is identical to that described previously, with an iterative solution converging on the final values of $\tilde{U}_{j,k}$ and $\tilde{x}_{j,k}$ (j=1,2,...,N). Equation (6.3) provides the initial guesses, which are alternatingly improved by (6.4) and by (6.7), (3.5), (3.6). Following convergence, Δt is either doubled, unchanged or halved (with the time-step calculation retried in the last case), depending on the estimated magnitude of the relative linearization error. Even with this step-size optimization, however, the matrix equation was solved 1,000 to 5,000 times during the $\tilde{\rho}-1 \ll 1$ experiments, requiring 10 to 45 seconds of IBM 370/168 computing time for three-sphere chains.

One notes that as $Re_\infty \to 0$, the integration procedure for (4.1) reduces to that for (4.3), since clearly (6.7) reduces to (6.1) as the Reynolds number vanishes, thus providing a proper limit behavior in which the short time scale of the initial acceleration period has been shrunk to zero.

7. Results for Three Coaxial Free Falling Spheres

In this section, the numerical results will be presented for three-sphere chains under a variety of Reynolds numbers and initial configurations. The initial spacings considered varied in the range $1 \leq \tilde{b}_o \leq 10$ and $1 \leq \tilde{c}_o \leq 10$, where

$$\tilde{b}_o = \tilde{b}(0) \qquad \tilde{c}_o = \tilde{c}(0)$$

$$\tilde{b}(t) = b(t)/a \qquad \tilde{c}(t) = c(t)/a$$

and b and c are center-to-center sphere spacings, defined in the insert of Figure 7. Results for $Re_\infty = 0$ numerical experiments are discussed in Subsections A and B. The effects of unsteady inertial forces are presented in Subsection C in conjunction with the results of the $0 < Re_\infty \ll 1$ runs.

While the numerical experiments presented herein corroborate the qualitative observations reported in Happel and Pfeffer (1960), there is no existing data to compare with the theory's quantitative predictions. For this reason, the authors have constructed a low Reynolds number settling apparatus for the purpose of obtaining detailed measurements in which unsteady inertial effects could be documented. The apparatus consisted of a 2-meter, clear, rigid cylinder with a constant diameter of 50 cm., which was filled with a highly viscous liquid (viscosity 18.5 gm/cm-sec, specific gravity 1.06). Small, identical, plastic spheres (specific gravity 1.147, diameter 0.905 cm.) were released into the fluid via a set of short, concentric, cylindrical guides protruding through the top plate. The spheres reaching the bottom of the apparatus were collected into an upright funnel and periodically removed through a two-valve arrangement. Accurate measurements of the particle trajectories as functions of time were made from large-scale projections of the filmed runs, taken at known regular intervals.

A comparison of the experimental observations with the theoretical predictions is presented in Subsection B.

A. Critical-Spacing Criterion for Near-Approach of Spheres

The qualitative behavior of three coaxial spheres falling at low Reynolds number was described in Section 1 for the case where spheres 2 and 3 asymptotically approach collision as illustrated in Figure 1. In simulating this behavior in the numerical experiments, a program-termination condition had to be incorporated, which takes into account that the multipole truncation procedure breaks down, for reasons discussed in Section 5, as the gap width goes to zero. Using Figure 6 as a guide, an effective collision was understood to have occurred if spheres 2 and 3 had approached to within a gap width of 0.05 diameters and had a finite relative velocity which, if extrapolated, would have taken the spheres through the contact condition $\tilde{c} = 1$. When this occurs it is understood that the limit has been reached and that the relative velocity $\tilde{U}_2 - \tilde{U}_3$ will asymptote rapidly to zero.

In other numerical experiments, however, the relative velocity $\tilde{U}_2 - \tilde{U}_3$ vanished before the effective collision distance $\tilde{c} = 1.05$ was obtained. In these situations one found that spheres 2 and 3 asymptotically approached a finite gap, while sphere 1 was already too far behind to have any appreciable interaction with them. The unequal interactions which sphere 1 has with the other two spheres causes sphere 2 to settle faster than sphere 3, but as the 2-3 doublet moves away from sphere 1, the relative velocity, $\tilde{U}_R \equiv \tilde{U}_2 - \tilde{U}_3$, decreases monotonically. One suspects, based on the following consideration of the two extreme cases $\tilde{b}_o = 1$ and $\tilde{b}_o \to \infty$ that there is a critical configuration condition which determines whether for a specified $\tilde{c}_o$ an effective collision between the two lead spheres will be achieved.

In the case of spheres 1 and 2 initially touching ($\tilde{b}_o=1$), sphere 2 will always close its gap with sphere 3, regardless of the initial spacing $\tilde{c}_o$. Even for an arbitrarily large $\tilde{c}_o$, spheres 1 and 2 can settle as an isolated doublet for as long as is necessary to approach and fall under the influence of sphere 1. On the other hand, if sphere 1 is initially very far away from sphere 2 ($\tilde{b}_o \to \infty$), the 2-3 doublet will forever be isolated and settle with $\tilde{U}_3 = \tilde{U}_2 > \tilde{U}_1$. We conclude, therefore, that for any initial spacing $\tilde{c}_o$ there must exist some critical initial spacing $\tilde{b}_o = \tilde{b}_{cr}$, such that when $\tilde{b}_o < \tilde{b}_{cr}$ the lubrication limit would be reached, and when $\tilde{b}_o > \tilde{b}_{cr}$ the relative velocity $\tilde{U}_R$ would vanish with the inter-particle gap still open.

Accordingly, a series of numerical experiments was conducted to determine $\tilde{b}_{cr}(\tilde{c}_o)$. The results are tabulated in Table 1 and are plotted in Figure 7 for $\tilde{\rho} = 1.1$ and $Re_\infty = 0.1$ and 0. Any combination of initial spacings located under the curve will result in a "near" collision.

Table 1

Values of Critical Spacing $\tilde{b}_{cr}$ for $\tilde{\rho} = 1.1$

$\tilde{c}_o$	$\tilde{b}_{cr}(Re_\infty = 0)$	$\tilde{b}_{cr}(Re_\infty = 0.1)$
1.2	6.428	6.545
1.6	2.845	2.995
2	2.102	2.273
3	1.553	1.659
4	1.355	1.470
7	1.170	1.301
10	1.113	1.246

B. Comparison of Theoretical and Experimental Results

As mentioned earlier in this section, experimental data were collected for the time-dependent settling of three coaxial spheres. The data for a typical run $Re_\infty = 0.011$, $\tilde{\rho} = 1.08$, $\tilde{b}_o = 1.63$, and $\tilde{c}_o = 7.38$ are compared with the theoretical predictions in Figure 8. The agreement between theory and experiment was found to be excellent provided the unsteady forces are retained in equation (4.1). One also observes in Figure 8 that the solution curve based on the full equation (4.1) is virtually indistinguishable from the solution curve obtained when the only unsteady force retained in equation (4.1) is the Basset force. In contrast, the $Re_\infty = 0$ theory based on equations (4.3) and (4.4), in which all unsteady forces are neglected, leads to discrepancies which progressively increase with time and are of the order of 20 percent at the end of the experimental run. The maximum deviation between theory and experiment when the Basset force effect is included is 2.9 percent*.

Figures 9 and 10 are velocity-time profiles for each sphere in a typical numerical experiment which leads to near collision, $\tilde{b}_o \approx 1$, $\tilde{c}_o = 10$, $\tilde{\rho} = 1.1$ at $Re_\infty = 0$ and $Re_\infty = 0.1$. After the initial unsteady period (which is shrunk to zero at $Re_\infty = 0$, Figure 9), spheres 1 and 2 possess essentially the same velocities, which are 30% to 40% greater than the velocity of sphere 3**. The velocity of sphere 2 does not vary greatly from this point to the end of the experiment. Sphere 3, however, begins to accelerate due to the reduction in its drag created by the approach of the

---

* Based on the theory presented in Leichtberg, Pfeffer and Weinbaum (1975), the wall correction factors are 1.057 on the central sphere and 1.069 on the outer ones. The pertinent quantity for Figure 8 is their difference, 1.2%, which was neglected.

** Note spheres 1 and 2 will not separate if b_o is identically unity since this problem is the inverse of the near collision problem for spheres 2 and 3 treated in Section 5. Spheres 1 and 2 are then started from an effective touching condition with $\tilde{b}_o = 1+\epsilon$, where $\epsilon \ll 1$.

doublet consisting of spheres 1 and 2. At the same time sphere 1 begins to decelerate due to the decrease in the drag reduction effect produced by sphere 2 separating and moving away from sphere 1. At some point in time, spheres 1 and 3 will have the same velocity indicating that the spacing parameters $\tilde{b}$ and $\tilde{c}$ are equal. From that point on the velocities of spheres 2 and 3 will approach each other while that of sphere 1 will decrease and asymptote to a value of $U_1/U_t = 1.0$, i.e., the terminal settling velocity of a single isolated sphere. The relative velocity curves for the same runs, $\tilde{U}_{2,3}(\tilde{t}) = \tilde{U}_2(\tilde{t}) - \tilde{U}_3(\tilde{t})$ and $\tilde{U}_{1,2} = \tilde{U}_1(\tilde{t}) - \tilde{U}_2(\tilde{t})$ are shown in Figure 11.

C. Effects of Unsteady Forces at Low Reynolds Number

The significant difference between the results of the $Re_\infty = 0$ and the $0 < Re_\infty \ll 1$ theoretical predictions shown in Figures 7, 10-12, and the close agreement between the experimental data and the theory for the full equation (4.1), as illustrated in Figure 8, strongly motivate a more detailed numerical study of the contributions of the various unsteady forces at low Re_∞ on both the short and long time scales.

Inspection of Figures 8, 9, and 10 reveals that the practical effect of the unsteady terms of the dynamic equations of motion is to reduce the relative velocity $\tilde{U}_{1,2}$ and hence the spacing $\tilde{b}$ between spheres 1 and 2. This, in turn, increases the relative velocity of approach between spheres 2 and 3, as shown in Figure 11, since the velocities of these two spheres are made unequal by their unequal interactions with sphere 1, the strength of the interaction being approximately inversely proportional to the spacing. The lubrication limit between spheres 2 and 3 is, therefore, reached sooner (if $\tilde{b}_o < \tilde{b}_{cr}$), as a result of including the unsteady and

inertial forces. As expected from the foregoing discussion, the effect of the unsteady forces, which increases with the Reynolds number, on the critical spacing curve is a modest increase in $\tilde{b}_{cr.}(\tilde{c}_o)$, as shown in Figure 7.

The two important order-of-magnitude deductions arrived at in Section 2 were that (i) all unsteady forces are of the same order (see equation (2.12)) on the initial short time scale of $0(Re_\infty \tilde{t})$ and that (ii) the Basset force, which is of $0(Re_\infty^{\frac{1}{2}})$, is the dominant unsteady force on the long time scale of $0(\tilde{t})$. The two-time-scale behavior is clearly exhibited by the velocity curves in Figures 9 and 10. One notes that after a short initial transient phase which is of $0(Re_\infty \tilde{t})$ the solution curves for the individual sphere velocities in Figure 10 approach the quasi-steady solutions for the $Re_\infty = 0$ case shown in Figure 9. Evidence supporting the second deduction has already been presented in Figure 8 where it was observed that very close agreement between theory and experiment could be obtained by neglecting all the unsteady forces except the Basset force in equation (4.1).

A more detailed insight into the importance of the various terms in (4.1) on the two time scales can be had by examining the relative magnitudes of the different unsteady forces acting on the three-sphere system at different times in typical numerical experiments at several values of Re_∞. Such data are presented in Table 2, where we have calculated the ratio of each of the unsteady forces to the buoyancy force B at different times for the case $\tilde{b}_o \approx 1$, $c_o = 10$, $\tilde{\rho} = 1.1$ at $Re_\infty = 0.1$ and 0.01 for each of the three spheres. Equation (4.1) can be written in terms of these force ratios as

$$\frac{F_D}{B} + (2\tilde{\rho}+1)\frac{F_{VM}}{B} + \frac{F_B}{B} = 1 \qquad (7.1)$$

Table 2

Forces Acting on the Three Sphere System for $\tilde{\rho} = 1.1$, $\tilde{b}_o \approx 1$, $\tilde{c}_o = 10$

Re_∞	t	F_D/B			F_{VM}/B			F_B/B		
		sphere 1	sphere 2	sphere 3	sphere 1	sphere 2	sphere 3	sphere 1	sphere 2	sphere 3
0.1	0.001	0.026	0.025	0.037	2.05×10^{-1}	2.05×10^{-1}	2.02×10^{-1}	0.318	0.319	0.317
	0.01	0.154	0.152	0.213	9.45×10^{-2}	9.48×10^{-2}	8.60×10^{-2}	0.544	0.545	0.512
	0.1	0.492	0.490	0.594	1.55×10^{-2}	1.56×10^{-2}	1.08×10^{-2}	0.458	0.460	0.371
	1	0.807	0.806	0.858	8.02×10^{-4}	8.05×10^{-4}	4.68×10^{-4}	0.190	0.191	0.140
	10	0.937	0.936	0.952	3.33×10^{-5}	3.51×10^{-5}	3.44×10^{-5}	0.063	0.064	0.048
	70	0.989	0.976	0.971	-5.95×10^{-5}	-1.42×10^{-5}	-2.59×10^{-6}	0.011	0.024	0.029
0.01	0.0001	0.026	0.025	0.037	2.05×10^{-1}	2.05×10^{-1}	2.05×10^{-1}	0.318	0.319	0.317
	0.001	0.154	0.152	0.213	9.45×10^{-2}	9.48×10^{-2}	8.60×10^{-2}	0.544	0.545	0.512
	0.01	0.494	0.492	0.596	1.53×10^{-2}	1.54×10^{-2}	1.07×10^{-2}	0.457	0.459	0.369
	0.1	0.807	0.806	0.858	8.00×10^{-4}	8.03×10^{-4}	4.60×10^{-4}	0.190	0.191	0.140
	1	0.937	0.937	0.954	2.93×10^{-5}	2.95×10^{-5}	1.75×10^{-5}	0.063	0.063	0.046
	10	0.980	0.980	0.985	1.47×10^{-6}	1.68×10^{-6}	2.73×10^{-6}	0.020	0.020	0.015
	70	0.997	0.993	0.991	-5.63×10^{-6}	-1.65×10^{-6}	-4.02×10^{-7}	0.003	0.007	0.009

One condludes from Table 2 that the Basset force decays much more slowly than the virtual mass and inertial forces, and that the sum of the latter, $(2\rho+1)F_{VM}/B$, is larger than the Basset force only at the very beginning of the short time scale. The virtual mass and inertial forces, which are directly related to the instantaneous value of the particle acceleration, lose their significance a very short time after the beginning of the run. The Basset force, on the other hand, is a lingering type of "memory" phenomenon, associated with the diffusion of the vorticity generated at an accelerating solid boundary. It is a function of the entire past history of the particle's motion, consequently tending to retain its importance even after the acceleration has ceased. On the long time scale $t > 0(Re_\infty)$ the Basset force is several orders of magnitude larger than the virtual mass and inertia forces. Since the behavior on this time scale dominates the overall motion when $0 < Re_\infty << 1$, it is not surprising that the solution curves shown in Figure 8 were almost the same whether or not the virtual mass and inertia terms were retained in the integration of (4.1).

Table 3 provides further interesting data, particularly regarding the two time scale motion of the spheres, for the $\tilde{b}_o \approx 1$, $\tilde{c}_o = 10$, $\tilde{\rho} = 1.1$ case at four different Reynolds numbers. Listed are values of (a) $\tilde{t}_s$, the duration of the initial acceleration period in the long time coordinate, defined as that point in time when the virtual mass force decays to less than one percent of the buoyancy force; (b) $\tilde{t}_L$, the time required for sphere 2 to approach sphere 3 to within 0.05 diameters ($\tilde{c} = 1.05$) and (c) the separation distance $2\tilde{b}(\tilde{t}_L)$ between spheres 1 and 2 at this time, which is given by $2\tilde{b}(\tilde{t}_L) = 2 + \int_o^{\tilde{t}_L} (\tilde{U}_2 - \tilde{U}_1)\, d\tilde{t}$.

Table 3

Short and Long Time Scale Behavior

$\tilde{b}_o \approx 1$, $\tilde{c}_o = 10$, $\tilde{\rho} = 1.1$

Re_∞	$\tilde{t}_s$	$\tilde{t}_L$	$2\tilde{b}(\tilde{t}_L)$
10^{-1}	1.36×10^{-1}	78.7	10.24
10^{-2}	1.43×10^{-2}	80.6	12.32
10^{-4}	1.37×10^{-4}	82.4	13.62
0	---	82.6	13.78

In view of the effect that the unsteady forces have on the relative velocities $U_{1,2}$ and $U_{2,3}$ observed in Figure 11, it is not surprising to see that the effect of increasing Re_∞ is to decrease both $\tilde{t}_L$ and $\tilde{b}(\tilde{t}_L)$. What is particularly striking are the large changes in sphere spacing that result over an extended run due to the accumulated effect of the Basset forces. Since the Basset force is of $0(Re_\infty^{\frac{1}{2}})$ these changes will be of $0(1)$ if the duration of an interaction $\tilde{t}_L$ is of $0(Re_\infty^{-\frac{1}{2}})$ or longer. One also observes in Table 3 that the virtual mass force decays to less than one percent of the buoyancy force when $\tilde{t}_s \approx 1.4\ Re_\infty$. Thus, in terms of the short time variable t* defined in equation (2.11), $t_s^* \approx 1.4$ independent of Re_∞. This behavior is consistent with our earlier observation that the governing equation (2.12) for a single sphere is independent of Re_∞ when written in terms of the stretched time coordinate t*. Such behavior, of course, does not persist when more than one sphere is present since the λ_j factors in equation (4.1) are implicit functions of Re_∞.

In concluding this section, we shall take note of the consequences of the reversible nature of a purely Stokes flow, i.e., $Re_\infty = 0$. Figure 12 presents the $\tilde{b}(\tilde{t})$ and $\tilde{c}(\tilde{t})$ curves for the $\tilde{b}_o \approx 1$, $\tilde{c}_o = 10$, $\tilde{\rho} = 1.1$ case at two Reynolds numbers, $Re_\infty = 0.1$ and 0. These curves, like all previous time plots, terminate at $\tilde{t} = \tilde{t}_L$, defined by $\tilde{c}(\tilde{t}_L) = 1.05$. Figures 9-12, however, have been extended (dotted lines) to include extrapolated sphere motion that would have ensued following the onset of lubrication-limit forces for $\tilde{c}(\tilde{t}) \leq 1.05$, as predicted by the present truncation method.

A striking feature of the two $Re_\infty = 0$ spacing curves of Figure 12 is the symmetry which exists about the half-time line, $\tilde{t} = 48.7$. The same symmetry exists for the three Re_∞ velocity curves in Figure 9. Thus, at $Re_\infty = 0$, the second half of the experiment is an identical duplicate of the first half, in reverse. An experiment which begins with $\tilde{b}_o \approx 1$ and $\tilde{c} = c_o$ will terminate with

$$\tilde{c} \approx 1 \ , \ \tilde{b} = c_o \ , \tag{7.2}$$

as seen in Figure 12, with the sphere velocities reversed accordingly, as seen in Figure 9. This phenomenon of reciprocity in the spheres' behavior at zero Reynolds number is due to the fact that in the absence of unsteady inertial forces the Stokes flow is completely reversible. This non-directional nature of a pure Stokes flow also explains why when two identical objects settle as an isolated doublet they have identical velocities, despite the fact that one is leading and the other trailing. At non-zero Reynolds numbers, the reciprocity no longer exists because of the unsteady forces, as observed for the $Re_\infty = 0.1$ curves in Figure 12.

The reciprocity principle was used as a check on the overall accuracy of the numerical procedures by running the $\tilde{b}_o \approx 1$ numerical experiment at $Re_\infty = 0$ and checking for compliance with the reciprocal terminal condition (7.2). It was found that the total accumulated error at the end of a run was 0.40%, 0.13%, and 0.06% for $\tilde{c}_o = 20$, 10, and 5, respectively.

8. Results for Chains of More Than Three Spheres

Numerical runs were conducted for chains of four to twenty-five settling spheres, using the theory and the numerical procedures developed in Sections 2-6. These runs showed a behavior pattern for long chains which strongly suggested that chains of non-touching spheres will generally tend to break up into smaller groups.

Consider a chain of N spheres, $N > 3$, equally spaced at $t = 0$, indexed from the trailing sphere ($j = 1$) to the leading sphere ($j = N$). Consider, too, an an accompanying example, Figure 13, which plots the time-dependent inter-sphere spacings $\tilde{D}_{j,j+1}(\tilde{t})$, $j=1,\ldots,6$, for a seven-sphere chain at $Re_\infty = 0$, with an equal initial sphere spacing $\tilde{D}_{j,j+1}(0) = 2$. In the initial equally-spaced configuration, the settling velocity is greatest for the central sphere, since it receives the maximum total interaction from all the other spheres. The velocity is lower for the other spheres, with the outer ones moving most slowly, their immediate neighbors somewhat faster, and so on. This neat ordering of the sphere velocities is valid only when all the spacings are equal, since at unequal spacings a central sphere may experience a greater drag force than one located closer to the end of the chain if the former is more isolated from its neighbors. However, for any combination of spacings, the outer spheres $j=1$ and $j=N$ necessarily experience less interaction than their immediate neighbors, $j=2$ and $j=N-1$. Hence, $U_2 > U_1$ and $U_{N-1} > U_N$. As a result, the spacing between spheres 1 and 2, D_{12}, is constantly increasing as sphere 1 becomes more isolated, while the spacing between spheres N-1 and N, $D_{N-1,N}$, continually decreases until the gap is nearly closed and spheres N-1 and N move as a steady doublet.

By this time, the spacing D_{12} has increased sufficiently to render sphere 1 fairly isolated, while the other spacings, $D_{23}, D_{34}, \ldots, D_{N-2,N-1}$, have changed by smaller amounts. The problem is now transformed to one of a chain of N-1 spheres headed by a doublet and trailed by a single, increasingly isolated sphere. Sphere 2 will now fall further behind, since it is now the trailing sphere of the chain. At the leading end of the chain the behavior depends on the spacings, as follows. If the spacing is such that U_{N-2} exceeds the velocity of the N - (N-1) doublet, then the spacing $D_{N-2,N-1}$ decreases steadily until a triplet is formed. If, on the other hand, the doublet's velocity exceeds U_{N-2}, the doublet will move on further ahead of the rest of the chain until the doublet is nearly isolated. At this point spheres N-2 and N-3 start behaving like the leading spheres of an N-3 sphere chain, forming a doublet, and the cycle of events continues.

The numerical experiments were not carried beyond this point due to computer time limitations, but the general pattern of the spheres' behavior is evident. The trailing third of a long chain of spheres will disintegrate into a series of single, isolated spheres. The leading half to two-thirds of the chain will break up into a series of doublets and triplets which, extrapolating the pattern of behavior for very long chains, would then recombine to form a series of shorter, unsteady chains.

Figure 13 illustrates the long chain behavior discussed above for the time period $0 \leq \tilde{t} \leq 30$. The spacing $\tilde{D}_{67}$ was artificially constrained to remain constant at 1.05 diameters after the gap narrowed to this lubrication limit.

9. Related Work and Concluding Remarks

The problem of the creeping motion of a finite chain of spheres in a cylindrically bounded medium has also been solved by the authors using similar procedures to those described herein and is currently being prepared for publication, Leichtberg, Pfeffer and Weinbaum (1975). This latter work is being used as the basis for a theoretical study of a possible hydrodynamic mechanism for the formation of rouleaux in the microcirculation. The authors have also been interested in the behavior of the three sphere problem for values of Re_∞ in the transition region where the length of the short time scale $\tilde{t}_s$ is of 0(1) or larger. An approximate semi-analytic theory was, therefore, developed for the Reynolds number range $1 < Re_\infty < 10$ where convective inertial effects are important but incipient wake bubble formation has not yet occurred. This study has been completed and will be reported elsewhere, Gluckman, Pfeffer, and Weinbaum (1975).

The most interesting new results of the investigation, which would appear to be of general validity for all multiparticle gravitational-Stokes flow interactions, is the importance of the Basset force in flow configurations which are slowly changing due to particle interactions. The theoretical and experimental results for the simple three-sphere geometry treated herein clearly show that lowest order departures from zero Reynolds number theory will result due to the cumulative effect of the Basset force, when the particle Reynolds number $2aU_t/\nu$ based on its terminal settling velocity U_t is $<< 1$ but the duration of the interaction is of $0(Re_\infty^{-\frac{1}{2}}\, a/U_t)$ or longer. Since particles in sedimenting flows usually sojourn many diameters before approaching boundaries, the above condition is encountered in most applications. Virtual mass and particle acceleration forces, on the other hand, are very short

lived and in many applications can be neglected entirely. The results also indicate that both the virtual mass and Basset forces are not significantly altered by multiparticle interaction effects and thus adequately approximated by their single particle representations for most engineering purposes.

The numerical results obtained in this study demonstrate that it is feasible with the present generation of computers to examine the fluid-particle interaction between moderate numbers of geometrically simple objects, provided a rapidly converging numerical technique can be devised for calculating the instantaneous quasi-steady state drag on each object. The multipole truncation technique developed in Gluckman, Pfeffer, and Weinbaum (1971) was well suited to this objective for the axisymmetric flow past spheres and spheroids. More than 10^4 quasi-steady three-sphere interactions with drag results accurate to better than 0.1 percent could be obtained in less than a minute on a moderate capacity present generation computer using this technique. The extension of this technique to truncated spherical harmonic representations of arbitrary three-dimensional multiple sphere configurations is currently in progress.

References

Bart, E. 1959 MCh.E. Thesis, New York University.

Basset, A.B. 1888 "Hydrodynamics", Deighton Bell, Cambridge, Dover, N.Y. 1961.

Brenner, H. 1961 Chem. Eng. Sci. 16, 242.

Burgers, J.M. 1938 "Second Report on Viscosity and Plasticity", Amsterdam, North Holland Publishing Co.

Darwin, C. 1953 Proc. Cambridge Phil. Soc. 49, 342.

Gluckman, M.J., Pfeffer, R. and Weinbaum, S. 1971 J. Fluid Mech. 50, 705.

Gluckman, M.J., Pfeffer, R. and Weinbaum, S. 1975 to be published.

Gluckman, M.J., Weinbaum, S. and Pfeffer, R. 1972 J. Fluid Mech. 55, 677.

Happel, J. and Brenner, H. 1965 "Low Reynolds Number Hydrodynamics", Prentice Hall, Inc.

Happel, J. and Pfeffer, R. 1960 A.I.Ch.E. Journal 6, 129.

Hocking, L.M. 1964 J. Fluid Mech. 20, 129.

Landau, L.D. and Lifshitz, E.M. 1959 Vol. 6 of Course of Theoretical Physics, Addison-Wesley Series in Advanced Physics.

Leichtberg, S., Pfeffer, R. and Weinbaum, S. 1975 "Stokes Flow Past Finite Coaxial Clusters of Spheres in a Circular Cylinder", to be published.

Leichtberg, S., Weinbaum, S. and Pfeffer, R. 1975 "A Theory for the Coaxial Slow Viscous Motion of Finite Clusters of Spheres in Unbounded Poiseuille Flow and its Application to Rouleaux Formation", to be published.

Milne-Thomson, L.M. 1960 Theoretical Hydrodynamics, 4th Edition, The MacMillan Co.

Oberbeck, H.A. 1876 Crelle 81, 62.

Skalak, R., Chen, P.H. and Chien, S. 1972 Biorheology 9, 67.

Smoluchowski, M. 1911 Bull. Inter. Acad. Polonaise Sci. Lett. 1A.

Stimson, M. and Jeffery, G.B. 1926 Proc. Royal Soc. A111.

Stokes, G.G. 1851 Trans. Cambr. Phil. Soc. 9(2), 8.

Wacholder, E. and Sather, N.F. 1974 J. Fluid Mech. 65, 417.

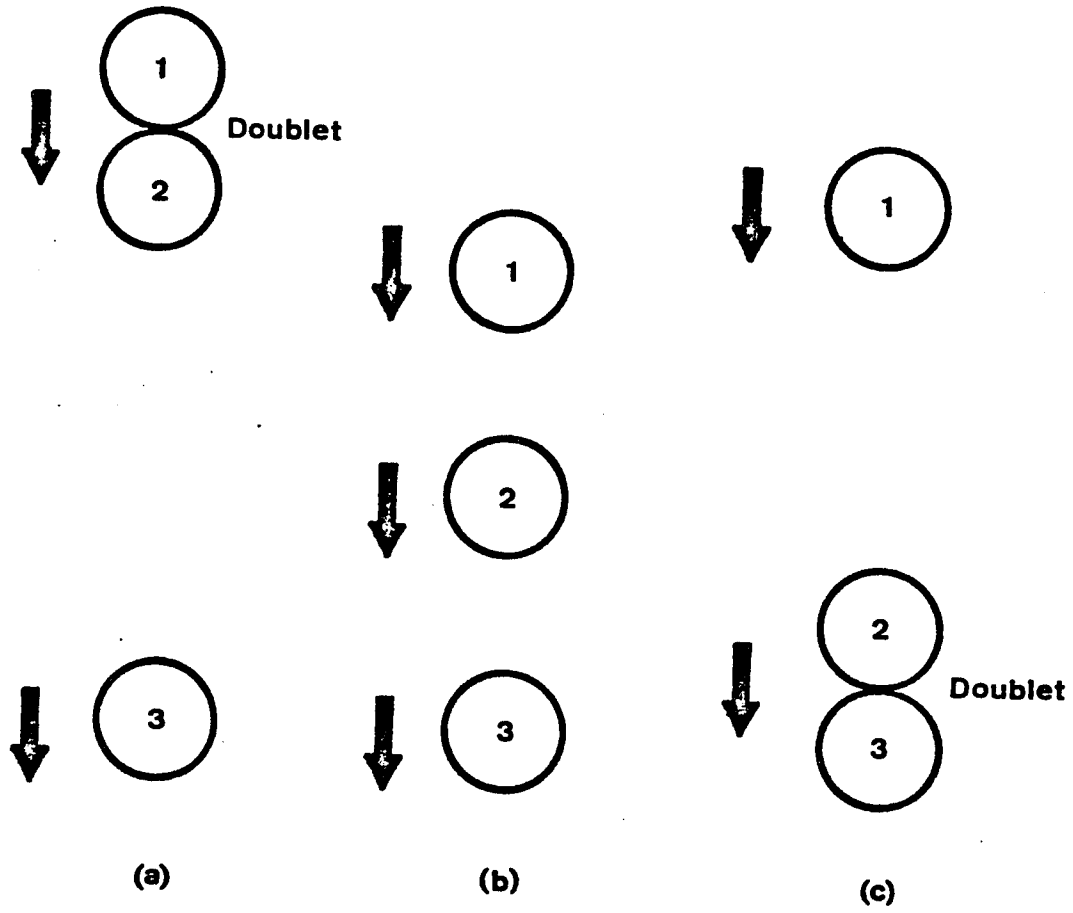

Figure 1. Gravity settling of three spheres.

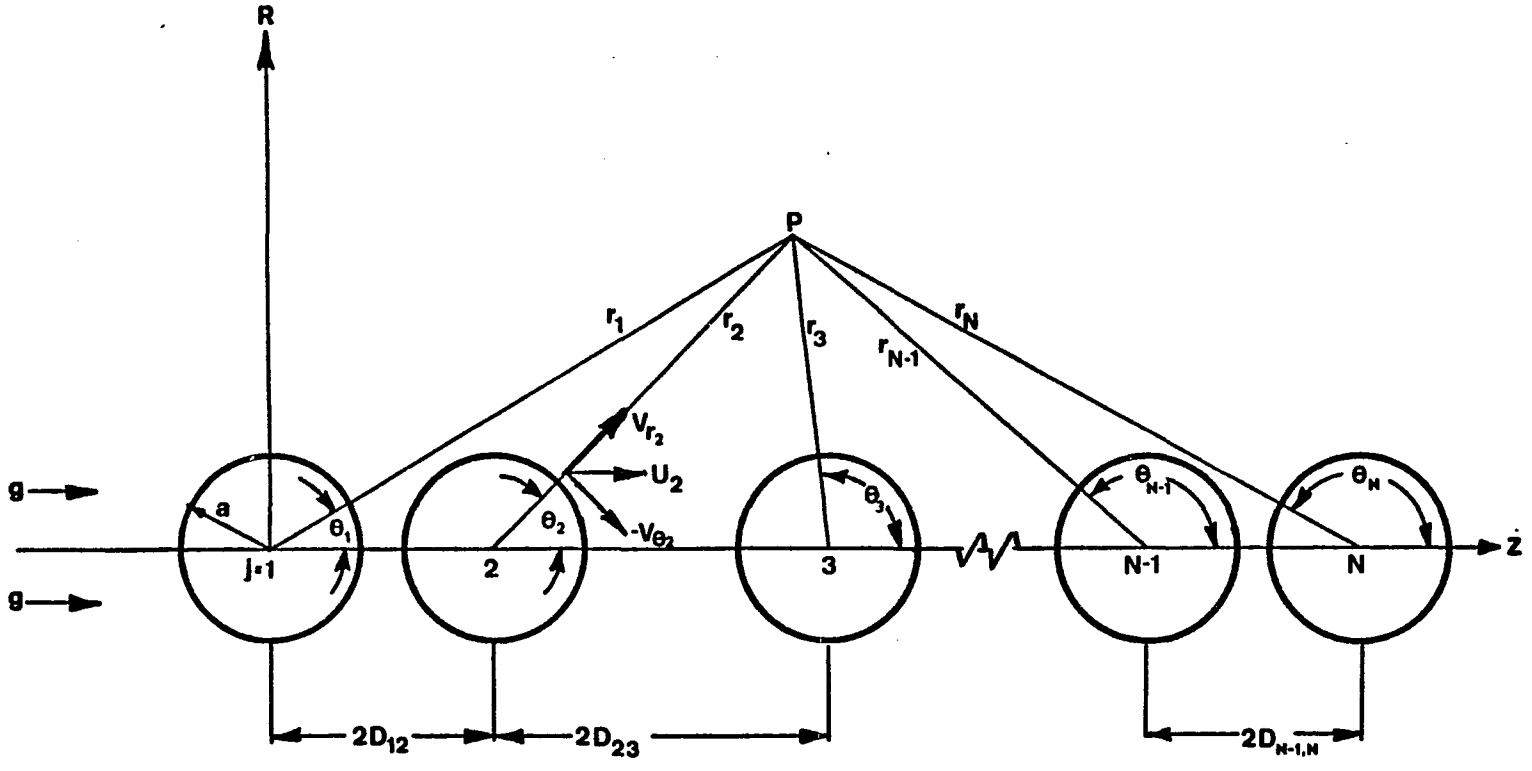

Figure 2. Geometry of N-sphere system.

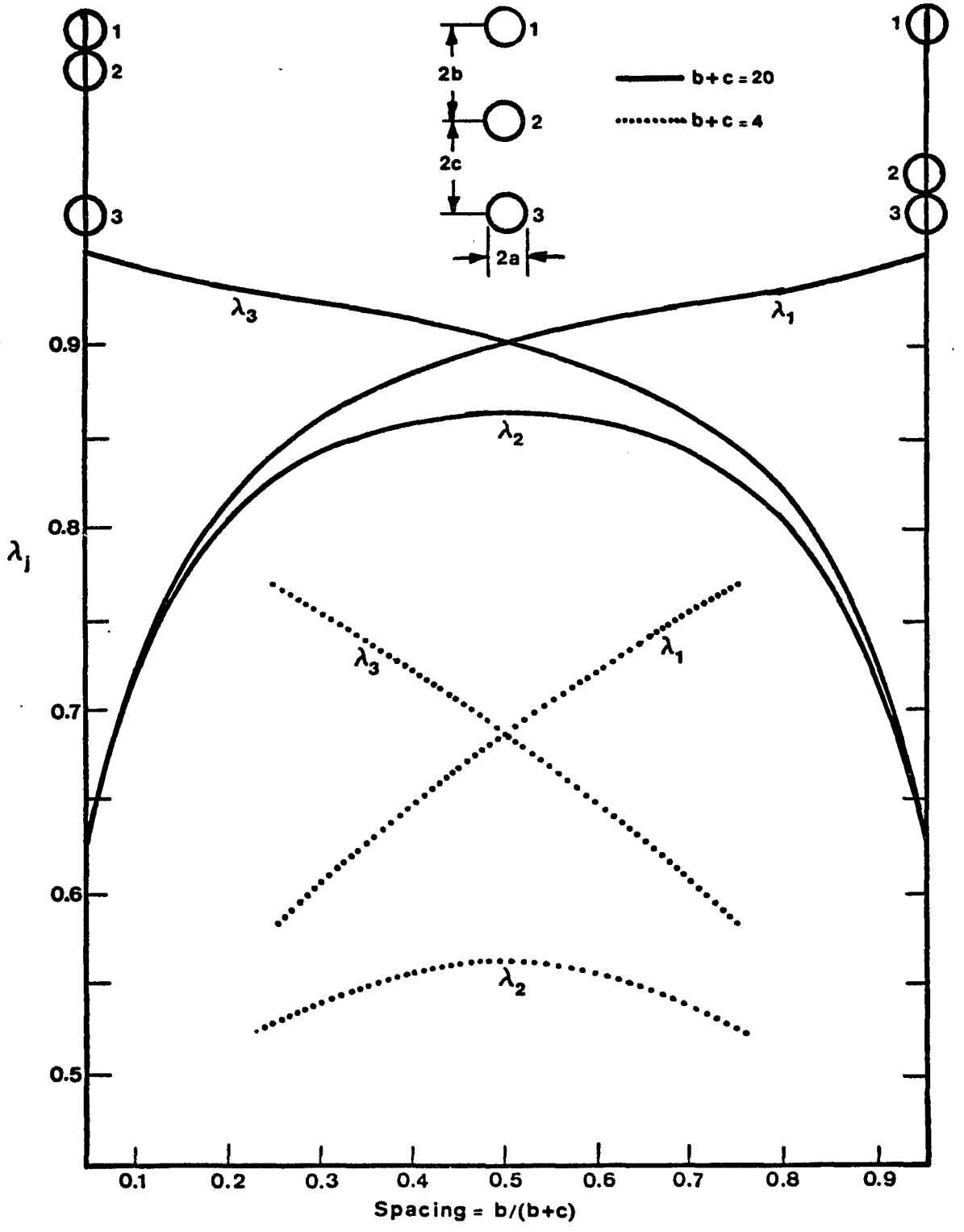

Figure 3. λ_j vs. spacing for three spheres.

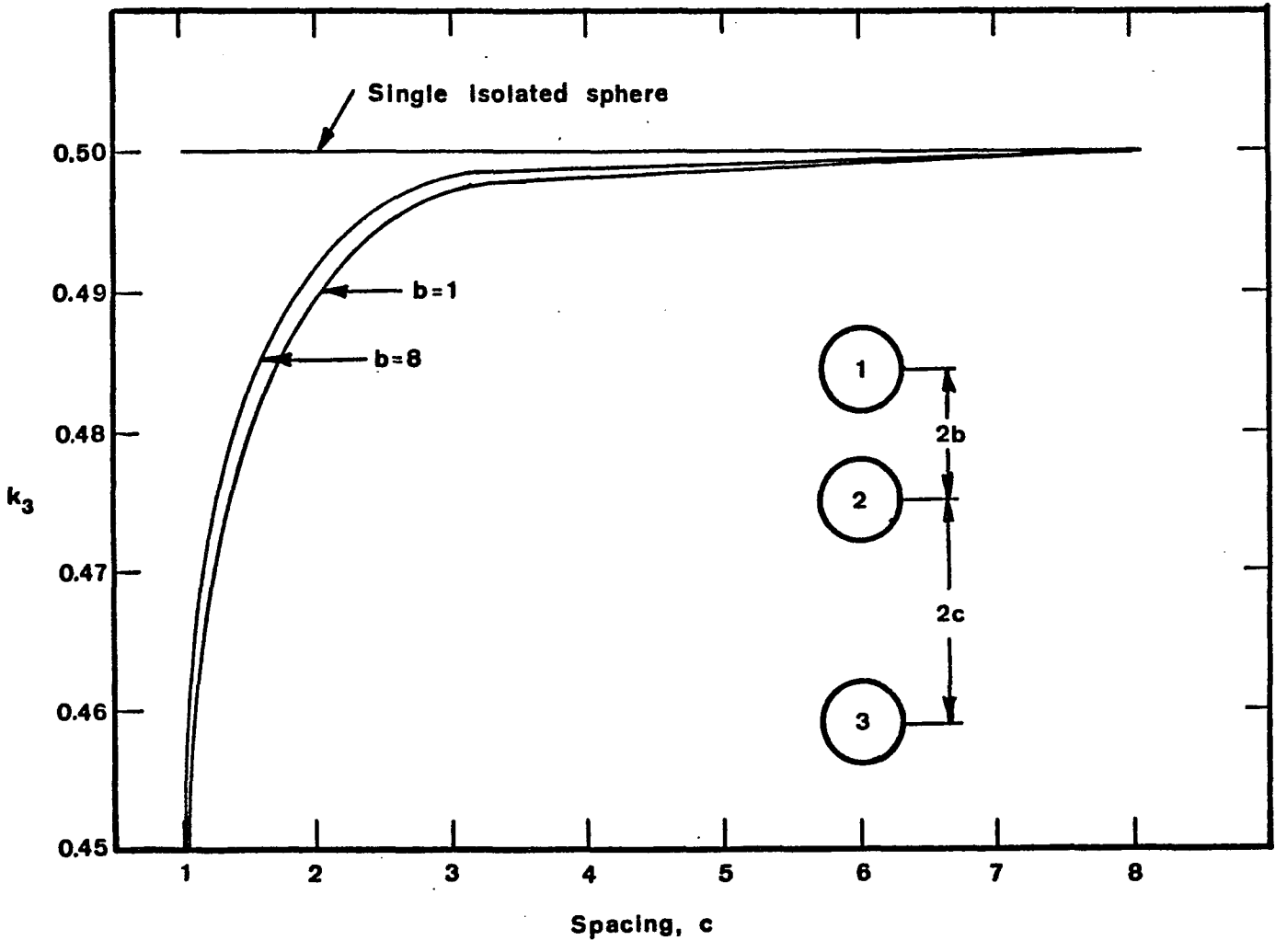

Figure 4. Deviation in virtual mass parameter k_3 vs. system geometry.

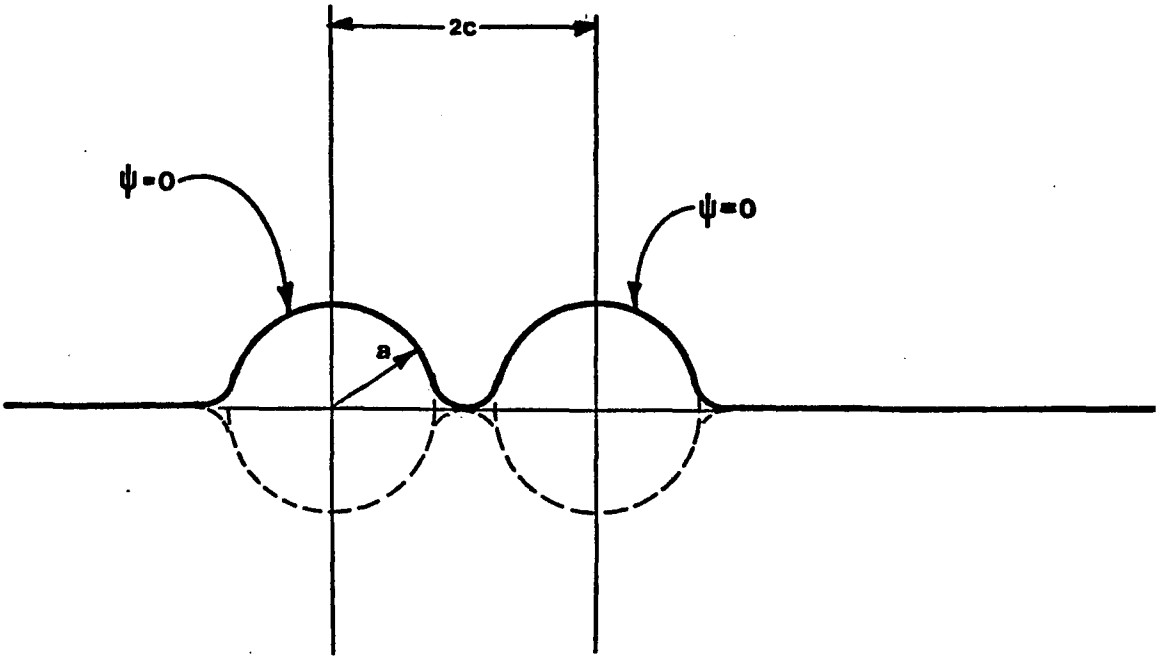

Figure 5. Deviation in the $\psi = 0$ streamline predicted by truncation technique.

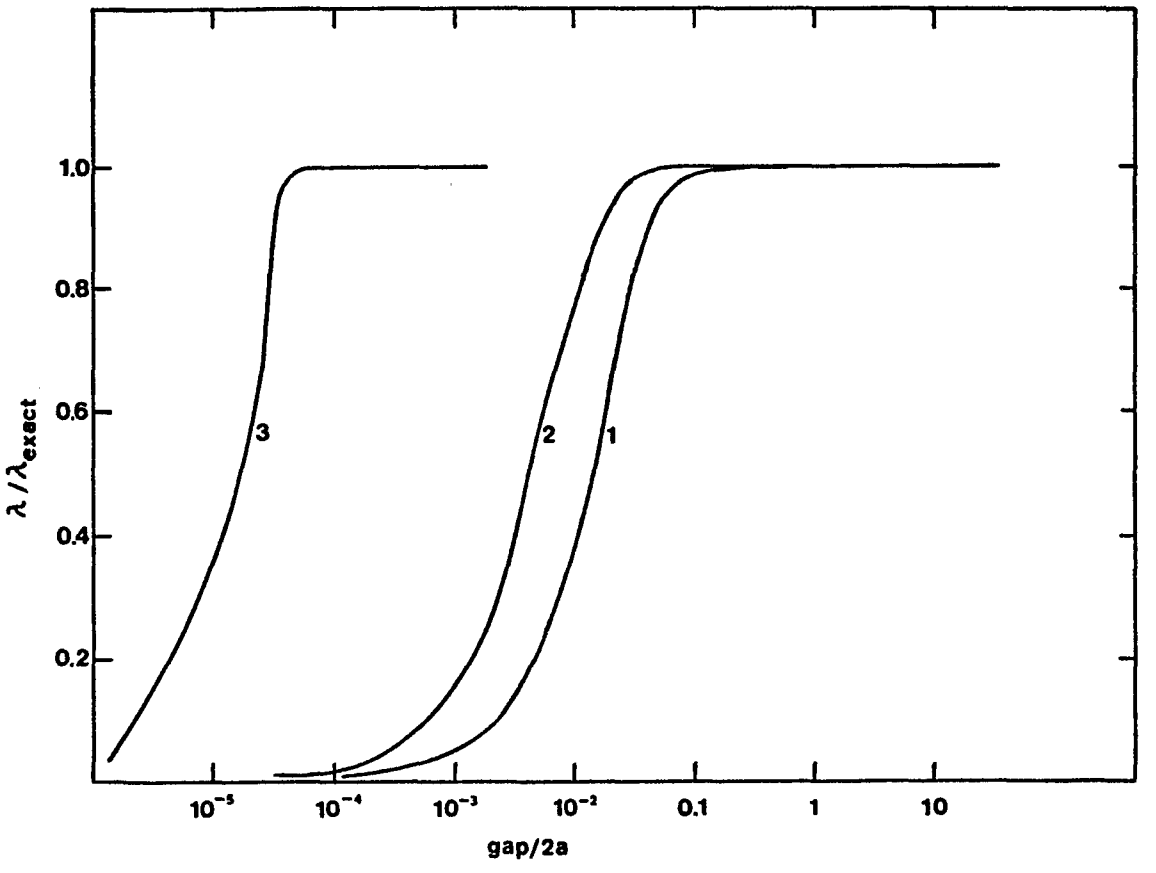

Figure 6. Comparison of predicted and exact drags; (1) 9 points, (2) 21 points, (3) 5 points starting at one degree.

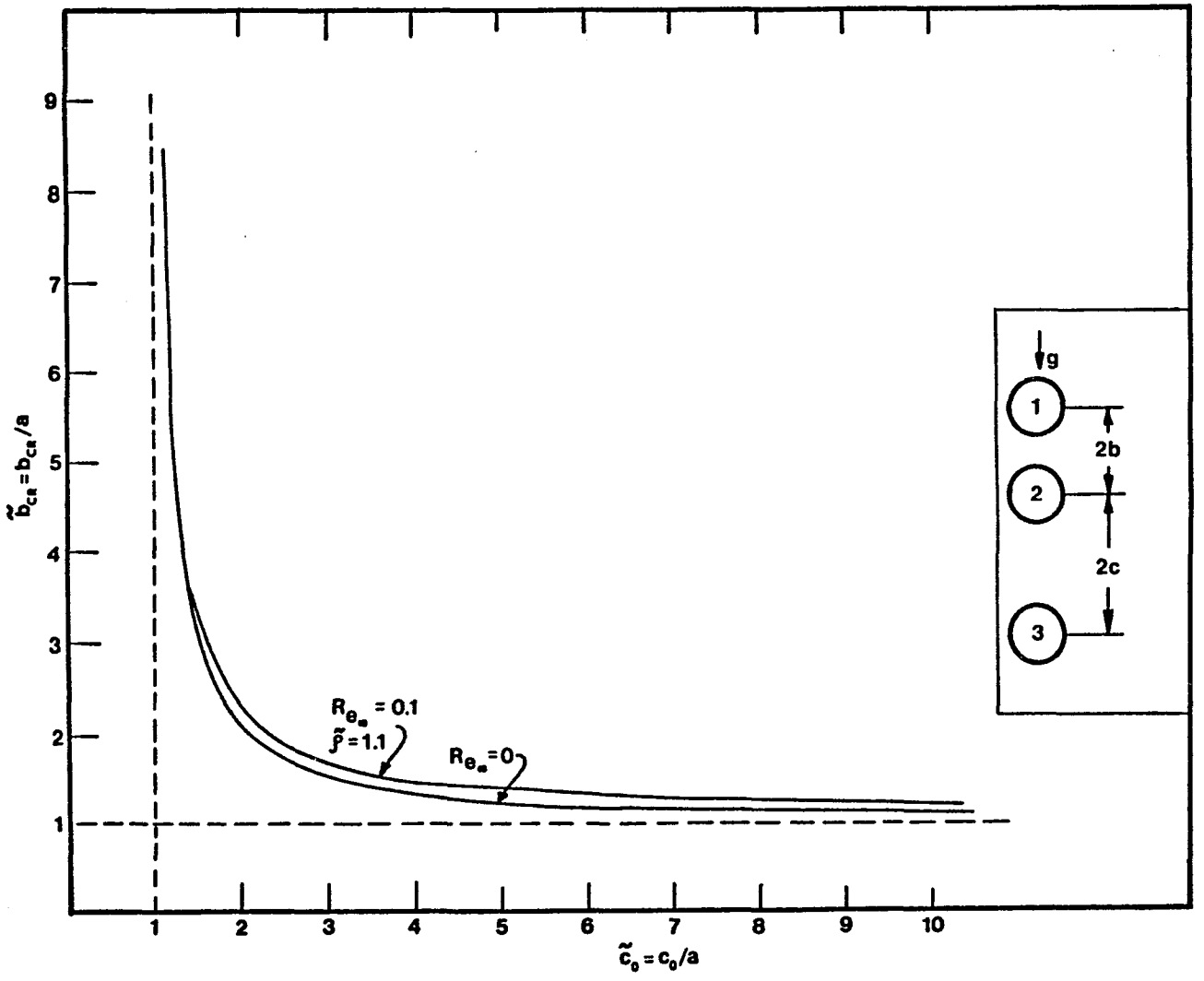

Figure 7. Critical initial spacing curves for R_{e_∞} = 0 and 0.1.

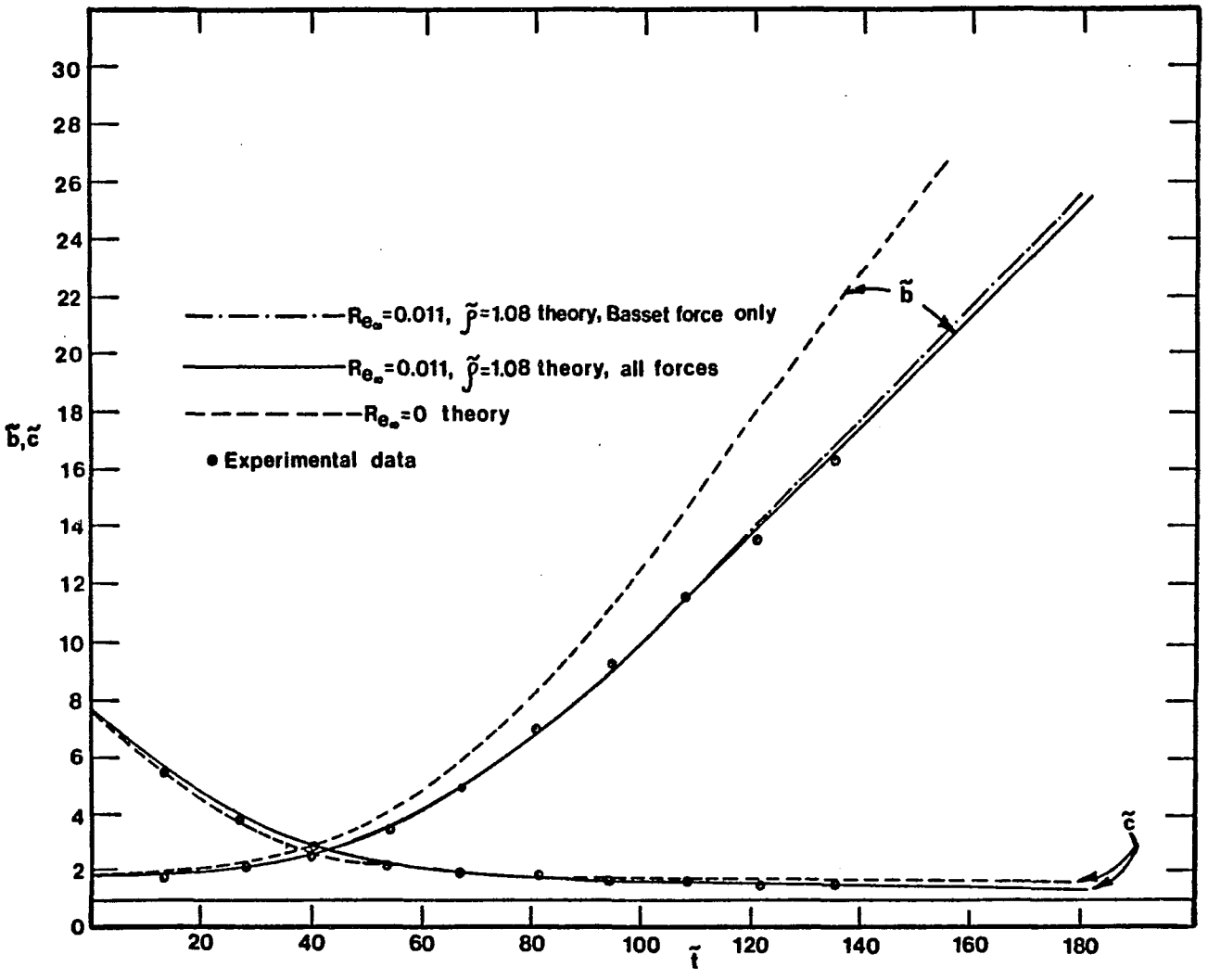

Figure 8. Comparison of theory with experimental data on sphere spacings; $\tilde{b}_o = 1.63$, $\tilde{c}_o = 7.38$.

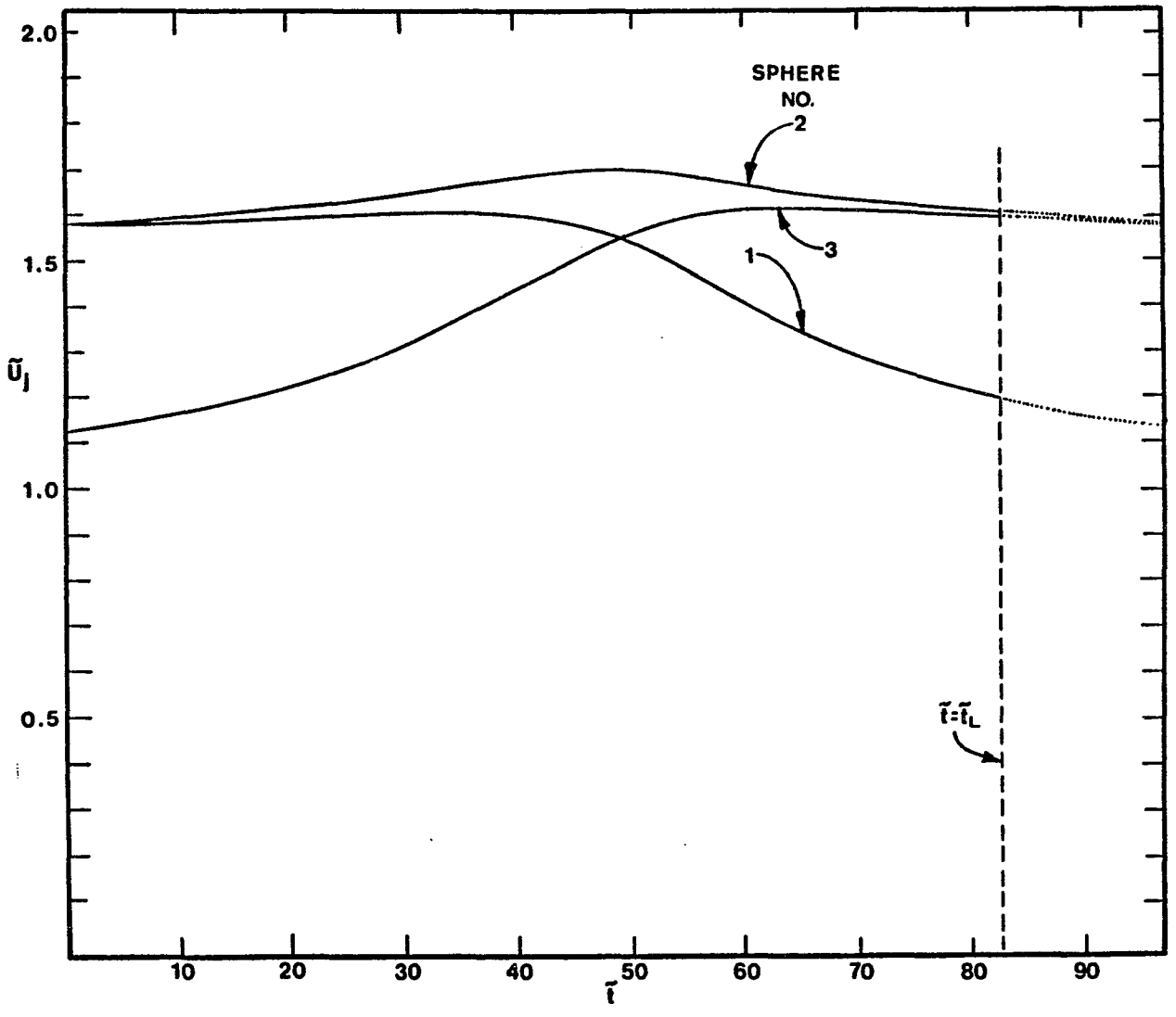

Figure 9. Velocity-time curves for a three-sphere chain, $\tilde{b}_o \approx 1$, $\tilde{c}_o = 10$, $Re_\infty = 0$; $\tilde{t}_L$ is defined by $\tilde{c}(\tilde{t}_L) = 1.05$.

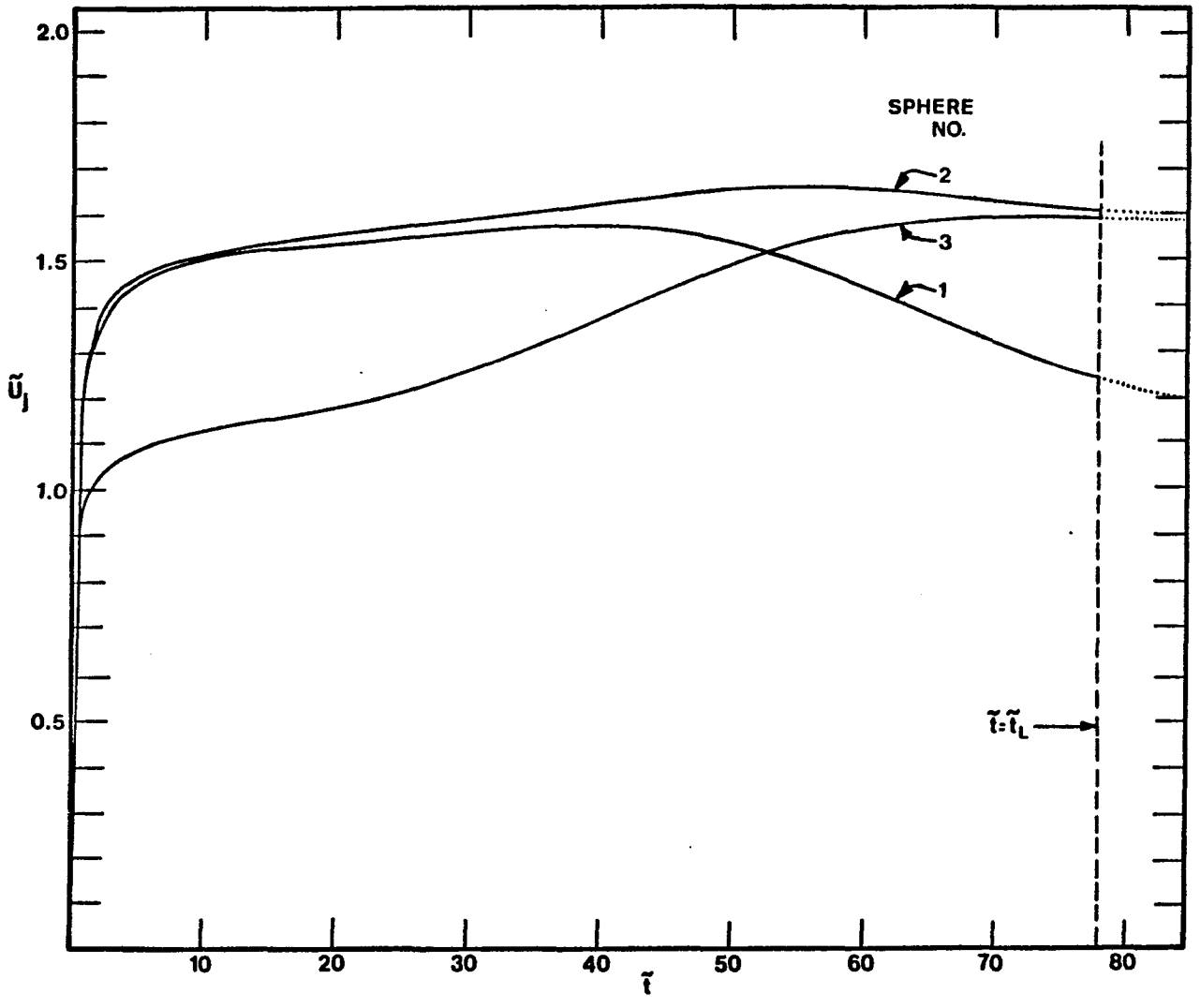

Figure 10. Velocity-time curves for a three-sphere chain, $\tilde{b}_o \approx 1$, $\tilde{c}_o = 10$, $Re_\infty = 0.1$, $\tilde{\rho} = 1.1$.

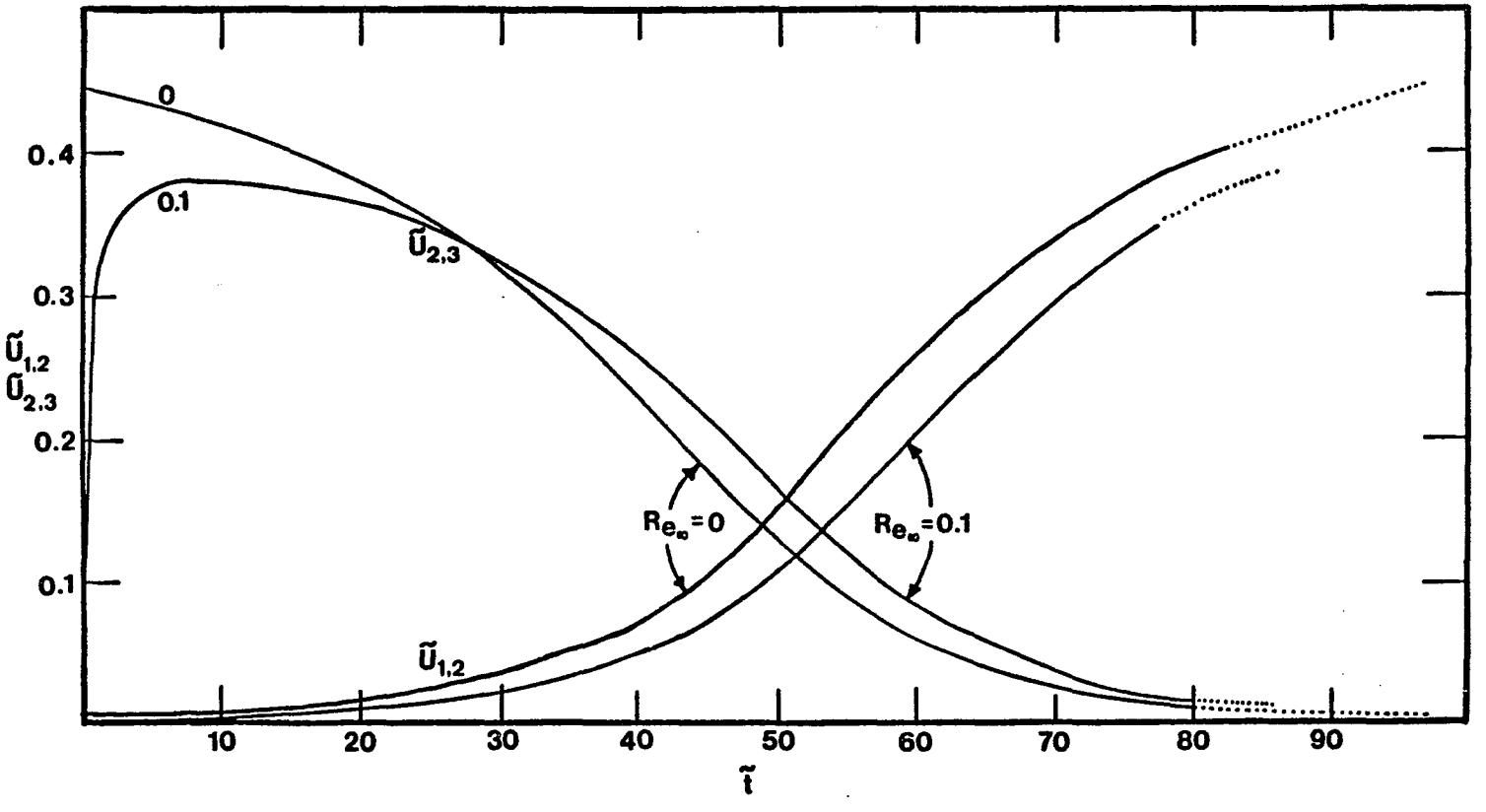

Figure 11. Relative velocity vs. time for the two leading and trailing spheres of a three-sphere chain, $\tilde{b}_o \approx 1$, $\tilde{c}_o = 10$, $\tilde{\rho} = 1.1$, $Re_\infty = 0.1$ and 0.

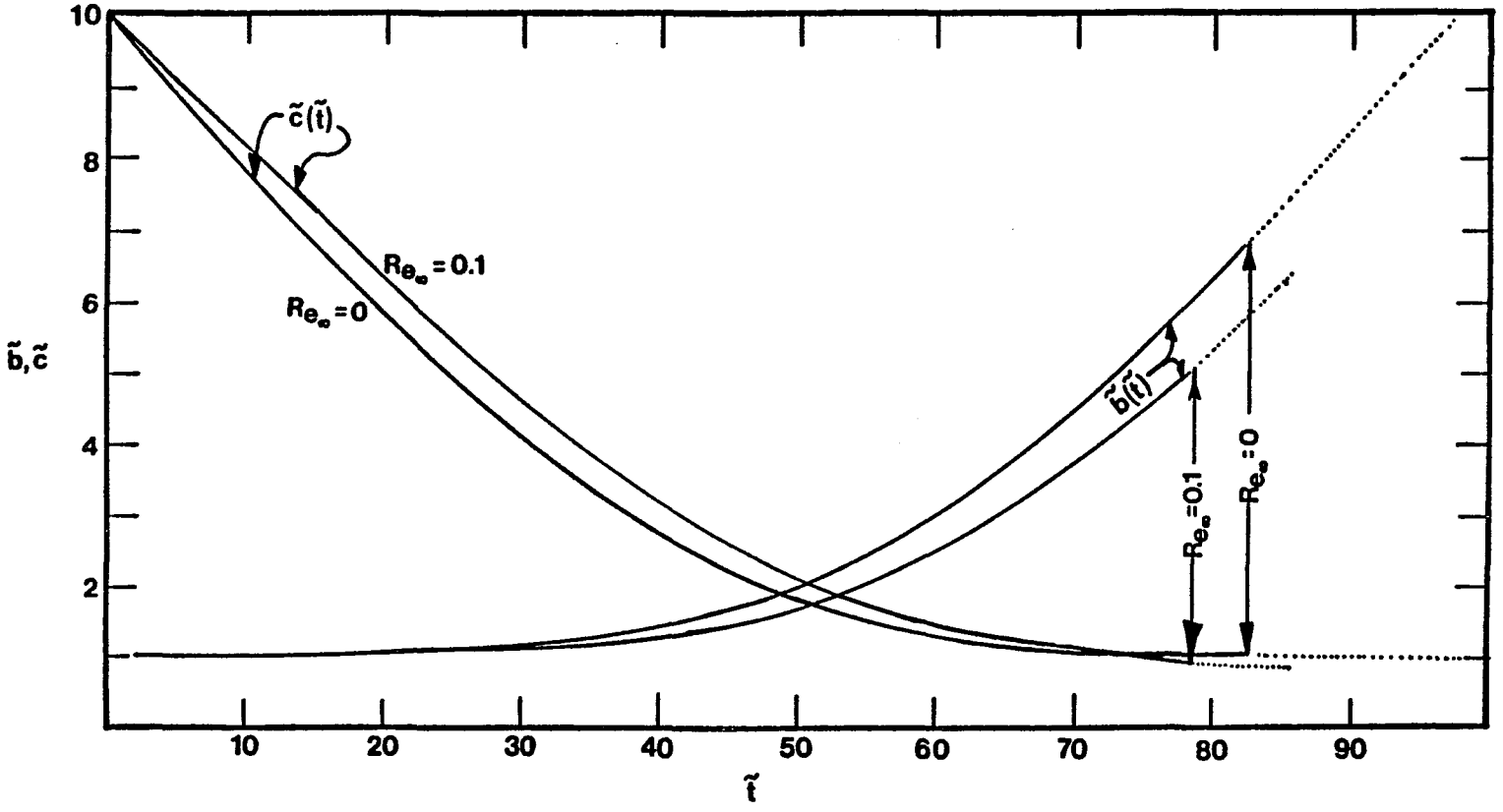

Figure 12. Sphere spacings vs. time for a three-sphere chain, $\tilde{b}_o \approx 1$, $\tilde{c}_o = 10$, $\tilde{\rho} = 1.1$, $Re_\infty = 0.1$ and 0.

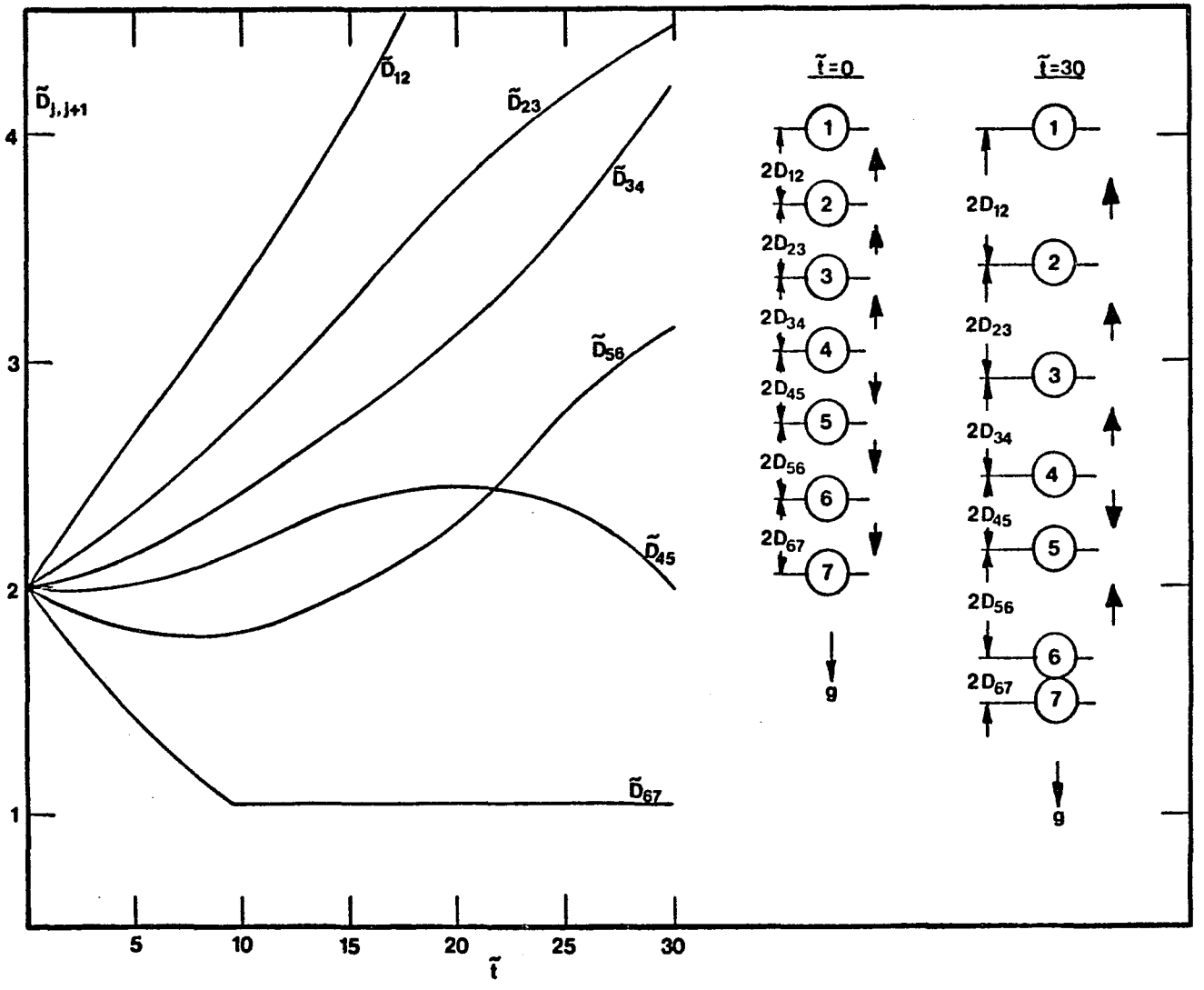

Figure 13. Sphere spacings vs. time for a seven-sphere chain, $\tilde{D}_{j,j+1}(0) = 2$ (j=1,2,...,6), $Re_\infty = 0$, ↑ = spacing is increasing, ↓ = spacing is decreasing.

CHAPTER III

STOKES FLOW PAST FINITE COAXIAL CLUSTERS OF SPHERES IN A CIRCULAR CYLINDER

Abstract

The solution of Stokes flow past a finite coaxial cluster of spheres in an infinitely long cylindrical tube is presented. General solutions are constructed from the fundamental solutions to the governing equation in both the cylindrical and spherical coordinate systems. No-slip boundary conditions are enforced on the tube surface by constructing a Fourier integral representation of the general disturbance created by the spheres and detected on the cylinder wall. No-slip boundary conditions are then applied on the sphere surfaces by a truncation technique developed previously in Gluckman, Pfeffer and Weinbaum (1971) for unbounded axisymmetric multi-particle flows.

Results, in the form of drag forces and zero-drag velocities, demonstrate the interparticle interaction effects, the sphere-wall interactions, and the effects of wall damping on the interparticle shielding phenomenon.

1. Introduction

The slow motion of an incompressible viscous fluid relative to assemblages of submerged particles has long been of interest in the areas of sedimentation, flow through packed and fluidized beds, the study of suspension viscosities, pollution abatement, and other engineering and bio-engineering applications involving viscous flow relative to assemblages of submerged solids. One particularly intriguing application is the investigation of blood flow in capillary blood vessels in which the red cells could be approximated by spheres or oblate spheroids whose diameters or major diameters are of the same order of magnitude as the diameter of the blood vessel.

Under the topic of blood flow, one interesting transient phenomenon to be considered is the formation of aggregates of red blood cells, or rouleaux, in the microcapillaries. It has been demonstrated in Leichtberg, Gluckman, Weinbaum and Pfeffer (1975) and in Leichtberg, Weinbaum, and Pfeffer (1975) that the mechanism involved in the formation of rouleaux of red blood cells may be hydrodynamical in nature and due to the inter-particle interaction forces which are unequally distributed among the particles and continually change as functions of particle spacing and velocity. The above referenced papers, however, deal exclusively with transient flows in unbounded media and must be presented in the context of the present paper in order to establish the limits of validity of extrapolating the results of unbounded flow theory to the bounded flow reality of the microcirculation. As the results of the present paper will demonstrate, the inter-particle interactions observed in the unbounded flow problem also exist in a bounded flow situation. Thus, the hydrodynamic mechanism which imparts unequal

drag forces, and consequently unequal velocities, to the various spheres in a chain is present with the solid boundaries as well as without them. The effect of the bounding surface on the inter-particle interactions is a damping effect; that is, the interaction is present but is steadily decreased as the particle-to-tube diameter ratio increases, with the amount of damping becoming significant at diameter ratios of 0.5 or greater.

Although a transient analysis of bounded flow is theoretically possible by the methods developed in Leichtberg, Gluckman, Weinbaum and Pfeffer (1975), the computational time required is prohibitive. The unbounded transient flow analysis, on the other hand, can be handled on a moderate capacity, present generation computer in 15 to 45 seconds per typical run. Hence, it was necessary to employ the indirect approach of utilizing unbounded transient and bounded quasi-steady results to develop a qualitative description of the bounded transient phenomenon.

The problem considered in this paper is the flow past a finite chain of rigid spheres in slow motion through a viscous fluid, which may be moving or stationary, inside an infinitely long cylindrical tube. The problems of multi-particle slow viscous flow have been previously treated extensively by four major approaches -- the method of reflections, the point force approximation, the finite element method, and the technique of singularity distributions over the solid boundaries.

The method of reflections, developed by Smoluchowski (1911, 1912) and used by Burgers (1940), Kynch (1959), and Happel and Brenner (1965) is an iterative approximation technique which has been extensively used to solve multi-particle and particle-wall interaction problems. In the case of particles settling near a solid wall, it is necessary first to establish the effect of the wall on the particles separately by the method of reflections

and then to combine these effects with those due to particle interaction by further application of the method of reflections. In determining the effect of the wall on a particle, one starts with the known solution for the isolated particle in an infinite medium and superposes (since the governing equation for Stokes' flow is linear) a first-reflection flow field such that the no-slip boundary conditions on the wall are satisfied exactly. The boundary conditions on the particle, however, are at best approximately satisfied if the particle-to-wall dimension ratio is small. The second reflection would superpose a third flow such that boundary conditions are satisfied exactly on the particle, but only approximately on the wall. In the case of one sphere moving near a wall, rapid convergence is obtained when the ratio of the characteristic particle to wall dimension is small. Bohlin (1960), using an extension of the method of reflections as originally presented by Faxen (1923), obtained drag results for a single sphere moving along the axis of a cylinder which exhibit very good agreement with the earlier more exact solution of Haberman and Sayre (1958), for sphere-to-cylinder diameter ratios of up to 0.6. For higher diameter ratios Bohlin's method breaks down due to certain simplifying assumptions.

Other investigations using the method of reflections were conducted by Ladenburg (1907) and Faxen (1922) who studied the drag of spheres moving in a still liquid inside a long cylindrical tube, by Wakiya (1953) and Happel and Byrne (1954) who studied the drag of spheres in Poiseuille flow inside a long cylinder, and by Greenstein and Happel (1970) who studied the axial motion of two spheres perpendicular to their line of centers, obtaining results which are in excellent agreement with the experimental results of Bart (1959).

The convergence characteristics of the method of reflections are strongly dependent on the ratio of the spacing between the particles and/or wall to particle dimensions. When this ratio is large (i.e., a dilute system), a single reflection describes the particle interaction adequately, as was done by Hocking (1964). For concentrated systems (the ratio approaching unity) higher order interaction effects become significant, and the leading term in the iterative series solution becomes a poor description of particle interaction effects and generates a series with very slow convergence characteristics. Furthermore, this method is extremely tedious to apply when more than two surfaces are present, and is, therefore, totally inapplicable to chains of spheres, especially in the presence of a bounding surface.

The point force technique, developed by Burgers (1938, 1941, 1942) and used by others, is only a useful approximation for dilute systems and is inapplicable to concentrated systems or to any bounded flow, because of the inability of point forces to account for the angular dependence of disturbances on one surface in the presence of others.

The finite-element treatment of multi-particle slow flow was most recently used by Skalak, Chen and Chien (1972) in treating the problem of capillary blood flow, consisting of biconcave disc-shaped solid particles equally spaced and axisymmetrically located in a circular tube. Using the finite element method, these authors examined the apparent viscosity of the blood in capillaries and its dependence on hematocrit and on the presence of rouleaux. This method is a very promising technique for irregular but identical particles with periodic spacing. The method cannot easily be applied to transient interaction problems or to steady flow problems where the particle boundary conditions are not periodic because of the slow decay properties of Stokes flow disturbances.

The techniques described above have not been used when more than two objects are present except for the special cases of the flow relative to an infinite chain of equally spaced particles along their line of centers. Because of the perfect periodicity existing in such infinite chains, this latter problem can be viewed as the flow past a single particle in a cell with periodic boundary conditions, e.g., Wang and Skalak (1969) and Chen and Skalak (1970).

The technique of describing solid boundaries by a distribution of internal singularities is based on the work of Payne and Pell (1960) who have shown that the infinite set of simply separable singular solutions for each co-ordinate system provides a complete set of generating functions, which can be used to satisfy rather general viscous flow boundary conditions along any constant co-ordinate surface of the same orthogonal co-ordinate system. Gluckman, Pfeffer and Weinbaum (1971) have taken advantage of the completeness of these fundamental separable solutions to extend the boundary method and obtain the exact Stokes solutions for a finite line array of spheres or spheroids in unbounded media, by placing a single infinite sequence of appropriate singularities at the origin of each sphere or spheroid. This study has shown that it is most efficient to use a truncated series of point singularities, and satisfy boundary conditions at discrete points on each object simultaneously. This method, the multipole truncation technique, yields first-, second-, and fifth-order truncation solutions for the drag which are accurate to 2.5, 0.1, and 0.001% respectively for flow parallel to the axis of two touching spheres, in sharp contrast to the poor results obtained by the method of reflections. This method was later extended in Gluckman, Weinbaum and Pfeffer (1972) to the exact

treatment of axisymmetric Stokes flow past an arbitrary convex body of revolution in an unbounded medium.

The principles developed by Payne and Pell were also used by Haberman and Sayre (1958) in obtaining an "exact" solution for a single sphere moving along the axis of an infinite cylinder. They employed the general solutions of the creeping motion equations for both the cylindrical and spherical coordinate systems, the latter being an expansion of the stream function. The cylindrical solution alone was used to satisfy the boundary conditions on the cylinder and the resulting expression was transformed into spherical coordinates. A term-wise comparison of the constants in this transformed expression with the constants in the direct spherical coordinate solution yielded a relationship between these constants. By substituting these relationships into the relationships which arise between the constants of the spherical solution as a result of applying the boundary conditions on the sphere, Haberman and Sayre obtained an infinite set of linear algebraic equations for evaluating the coefficients appearing in the general expansion of the stream function. Wall correction factors were obtained for both rigid and fluid spheres, in both moving and stationary media.

Hochmuth and Sutera (1970) treated the motion of a large concentric sphere moving in a long tube by combining the methods of Haberman and Sayre with lubrication theory arguments. The problem of a sphere eccentrically located in close proximity to a tube wall was treated by Goldman, Cox and Brenner (1967) by obtaining an exact solution in bipolar coordinates, and by Bungay and Brenner (1973) via a regular perturbation procedure. Brenner (1970 and 1971) studied the motion of a small, eccentric,

neutrally-buoyant solid particle or liquid droplet, demonstrating that the pressure drop could be obtained without the need for a detailed solution satisfying the boundary conditions on the tube wall.

The technique used in the present paper for finite chains of spheres inside a cylinder satisfies the tube boundary conditions, using the infinite set of simply separable singular solutions in both the spherical and cylindrical coordinate systems. The resulting expression, which contains unknown constants but which nevertheless satisfies the boundary conditions on the cylinder independently of these constants, is then used to satisfy the boundary conditions on all the spheres simultaneously in a manner similar to the multipole truncation technique developed in Gluckman, Pfeffer, and Weinbaum (1971).

Section 2 presents the formulation of the problem, its governing equations and the boundary conditions. Section 3 outlines the solution procedure, and section 4 deals with the methods of calculating either the drag forces or zero-drag velocities. Sections 5 and 6 then present and discuss the results.

2. Formulation of the Problem

The flows considered in this paper are assumed to be axisymmetric, with the line of sphere centers coinciding with the cylinder axis, so that the Stokes stream function exists. It is further assumed that the motion is sufficiently slow for the creeping motion equations to be valid. Before presenting these equations, it is convenient to non-dimensionalize all the variables. Denoting the dimensional variables with a tilda, we obtain the non-dimensional velocity (U or V), stream function (ψ), drag force (F_D), pressure (p), and length (L) as follows:

$$U = R_o\tilde{U}/\nu \ , \ \psi = \tilde{\psi}/R_o\nu \ , \ F_D = \tilde{F}_D/\rho\nu^2 \ ,$$

$$p = \frac{R_o^2}{\rho\nu^2}(\tilde{p} - \rho g\tilde{z}) \ , \ L = \tilde{L}/R_o \ , \tag{2.1}$$

where R_o = tube radius, ν = kinematic viscosity, and ρ = fluid density. The expression for dimensionless pressure includes the possible effect of body forces. It is assumed that this body force per unit mass, g, acts in the positive axial $\tilde{z}$ direction only, if it is present at all.

The equations of motion for Stokes creeping flow are:

$$\nabla p = \nabla^2\vec{V} \tag{2.2}$$

$$\nabla\cdot\vec{V} = 0. \tag{2.3}$$

Taking the curl of both sides of (2.2) and introducing (2.3) and the stream function results in a fourth-order partial differential equation for the stream function.

$$\vec{\omega} = \nabla \times \vec{V} = \vec{i}_3 h_3 E^2 \psi \tag{2.4}$$

$$E^2(E^2\psi) = 0, \tag{2.5}$$

where

$$E^2 = \frac{h_1 h_2}{h_3}\left[\frac{\partial}{\partial q_1}\left(\frac{h_1 h_3}{h_2}\frac{\partial}{\partial q_1}\right) + \frac{\partial}{\partial q_2}\left(\frac{h_2 h_3}{h_1}\frac{\partial}{\partial q_2}\right)\right]. \tag{2.6}$$

Here (q_1, q_2, q_3) are generalized orthogonal curvilinear coordinates, h_1, h_2, h_3 are the metrical coefficients of this coordinate system, ψ is assumed independent of q_3 and the operator E^2 is the generalized axisymmetric Stokesian linear operator. In cylindrical coordinates, (2.6) reduces to (see Figure 1 for coordinate definition)

$$E^2 = \frac{\partial}{\partial R^2} - \frac{1}{R}\frac{\partial}{\partial R} + \frac{\partial^2}{\partial z^2}, \tag{2.7}$$

and

$$E^2\psi = R\omega. \tag{2.8}$$

In spherical coordinates,

$$E^2 = \frac{\partial^2}{\partial r^2} + \frac{1-\zeta^2}{r^2}\frac{\partial^2}{\partial \zeta^2} \tag{2.9}$$

and

$$E^2\psi = \omega r \sin\theta \tag{2.10}$$

where $\zeta = \cos\theta$ for brevity.

The geometry being considered is shown in Figure 1. The various spheres in the N-sphere chain are equally spaced and are

indexed from $-(N-1)/2$ to $(N-1)/2$ with the origin taken at the central sphere for convenience. In this manner, the system is symmetrical about the $z = 0$ plane and the descriptive equations are expected to be even functions of z. For an even number of spheres, a slight rearrangement achieves the same results. The flow far downstream is a Poiseuille flow with the velocity profile

$$v(R) = V(1-R^2) \tag{2.11}$$

where V is the downstream centerline velocity and is related to the discharge, Q, by

$$Q = \frac{\tilde{Q}}{R_o \nu} = \frac{\pi}{2} V. \tag{2.12}$$

The no-slip boundary conditions, written with reference to the cylinder wall are:

$$\psi = V\left(\frac{R^2}{2} - \frac{R^4}{4}\right), \quad |z| \to \infty \tag{2.13}$$

and

$$\left.\begin{aligned} v_z &= 0 \qquad (2.14a) \\ \psi &= \frac{V}{4} \qquad (2.14b) \end{aligned}\right\} \quad R = 1$$

at the cylinder wall, $R = 1$. On each of the N sphere surfaces, $r_j = a$,

$$\left.\begin{aligned} v_{r_j} &= U\cos\theta_j \qquad (2.15a) \\ v_{\theta_j} &= U\sin\theta_j \qquad (2.15b) \end{aligned}\right\} \quad r_j = a, \quad j = -\frac{N-1}{2} \text{ to } \frac{N-1}{2},$$

In the sphere boundary conditions, the origin of coordinates for the purpose of determining v_{r_j} and v_{θ_j} by differentiation of ψ is the center of the sphere on which the condition is being applied. This means that boundary conditions (2.15) are to be applied from N different coordinate origins, which makes their application extremely tedious. For this reason it is simpler to use the cylindrical R-z coordinate system which has common coordinates for all spheres. Since the velocities v_{r_j} and v_{θ_j} are orthogonal and in the same plane, all other velocities originating from the same point as v_{r_j} and v_{θ_j} and in the same plane must be zero relative to an observer moving with sphere j. In particular, v_z and v_R must be identically zero, and therefore, with reference to the cylinder wall,

$$\left.\begin{aligned} v_z &= U \qquad (2.16a) \\ v_R &= 0 \qquad (2.16b) \end{aligned}\right\} \text{ on } r_j = a \text{ , all j.}$$

3. Solution

This section is presented in three subsections: (A) the general solution, (B) the cylinder boundary conditions, and (C) the sphere boundary conditions.

A. The general solution

The general solutions to $E^4\psi = 0$ are originally due to Sampson (1891), but are also given by Savic (1953) and Haberman and Sayre (1958). In the cylindrical coordinate system, the general solution is

$$\psi(R,z) = a_1R^2 + a_2R^4 + \int_0^\infty [A(\lambda)RI_1(\lambda R) + B(\lambda)R^2I_0(\lambda R)]\cos\lambda z\,d\lambda + \int_0^\infty [D(\lambda)RI_1(\lambda R) + C(\lambda)R^2I_0(\lambda R)]\sin\lambda z\,d\lambda \quad , \tag{3.1}$$

where $A(\lambda)$, $B(\lambda)$, $C(\lambda)$, and $D(\lambda)$ are unknown functions of λ, a_1 and a_2 are unknown constants, and I_0 and I_1 are modified Bessel functions of the first kind. Other terms in the general solution have been dropped because they become infinite at $R = 0$ or as $z \to \infty$. By satisfying the boundary conditions at $R = 1$, the solution (3.1) will be constrained, by proper choice of the unknown functions, to cancel out the disturbances created by the spheres and experienced by the cylinder wall. Hence, the Fourier integral form, rather than the series form, was chosen, since the functional representation over the infinite domain, $R = 1$, requires a continuous range rather than discrete values of the eigenvalues, λ. Since the system is symmetrical about $z = 0$, the disturbances created by the spheres, at very low Reynolds numbers, will be likewise symmetrical and, hence, even

functions of z. If (3.1) is to define these disturbances at R = 1, then it should first be reduced to the cosine integral, i.e.,

$$\psi(R,z) = a_1R^2 + a_2R^4 + \int_o^\infty [A(\lambda)RI_1(\lambda R) + B(\lambda)R^2I_o(\lambda R)] \cos\lambda z d\lambda . \tag{3.2}$$

In the spherical coordinate system (r,θ), the general solution to $E^4\psi = 0$ is

$$\psi(r,\theta) = \sum_{n=o}^{\infty}(C'_n r^n + D'_n r^{n+2} + C_n r^{-n+1} + D_n r^{-n+3})\mathcal{J}_n(\zeta) \tag{3.3}$$

where $\mathcal{J}_n(\zeta)$ are Gegenbauer functions of the first kind of order n and degree $-\frac{1}{2}$. C'_n, D'_n, C_n, and D_n are arbitrary constants of integration. Terms which are infinite all along the cylinder axis, $\theta = 0$, have been omitted from (3.3). The velocity components, $v_r = -(1/r^2\sin\theta)\partial\psi/\partial\theta$ and $v_\theta = (1/r\sin\theta)\partial\psi/\partial r$ which are obtained from (3.3), representing the velocity disturbances created by the spheres, must vanish far downstream where $r \to z \to \pm\infty$, $\sin\theta \to 0$, and $r\sin\theta = R$. This condition, plus the adjustment necessary to make ψ vanish on the centerline, results in the following evaluation of some of the constants in (3.3)

$$\begin{aligned} C'_n &= D'_n = 0 \quad \text{for all } n, \\ C_n &= D_n = o \quad , \; n = 0,1. \end{aligned} \tag{3.4}$$

Application of (3.4) to (3.3) results in the following general form for the stream function in spherical coordinates:

$$\psi(r,\theta) = \sum_{n=2}^{\infty}[C_n r^{-n+1} + D_n r^{-n+3}]\mathcal{J}_n(\zeta). \tag{3.5}$$

Equation (3.5), representing a spherical disturbance in the flow field, is singular at the origin of coordinates, r = 0. In order to successfully satisfy the no-slip boundary conditions on the surface of each of the N spheres in the chain, it becomes necessary to place the singularity (3.5) at each sphere's center. The spherical solution, ψ_j, which is singular at the center of the j^{th} sphere is given by (3.5) when the origin of coordinates is placed at the point of singularity, i.e.,

$$\psi_j = \sum_{n=2}^{\infty} [C_{nj} r_j^{-n+1} + D_{nj} r_j^{-n+3}] \mathcal{J}_n(\zeta_j), \tag{3.6}$$

$$\zeta_j = \cos\theta_j.$$

Here the r_j and θ_j coordinates are measured from the origin of each sphere considered separately (see Figure 1). The singular solution (3.6) is placed at the center of each sphere by utilizing the linearity of the governing equation and superimposing the solutions (3.6) as follows

$$\psi = \sum_{j=-\frac{1}{2}(N-1)}^{\frac{1}{2}(N-1)} \psi_j \quad \text{for N odd,} \tag{3.7a}$$

For N even the origin is taken midway between the two central spheres and the indexing of j is altered. Combining (3.6) and (3.7a) yields the spherical solution representing flow field disturbances created by N spheres

$$\psi = \sum_{j} \sum_{n=2}^{\infty} [C_{nj} r_j^{-n+1} + D_{nj} r_j^{-n+1}] \mathcal{J}_n(\zeta_j). \tag{3.7b}$$

The index limits on the outer summation have been omitted for the sake of brevity and generality of application to odd and even-numbered chains, and it remains understood that the j-summation is carried for all the N spheres.

In Gluckman, Pfeffer and Weinbaum (1971), the complete general solution for a chain of spheres moving through an unbounded medium was given as (3.7), and boundary conditions on the spheres were used to determine the values of the C_{nj} and D_{nj} unknown coefficients. In the present problem the complete general solution must also include the cylindrical-coordinate solution (3.2) in order to be able to satisfy the cylinder boundary conditions as well. Hence, the general solution to (2.5) is constructed as the superposition of the cylindrical solution (3.2) and the spherical disturbance representation (3.7), i.e.,

$$\psi = a_1 R^2 + a_2 R^4 + \int_0^\infty [A(\lambda) R I_1(\lambda R) + B(\lambda) R^2 I_0(\lambda R)] \cos\lambda z \, d\lambda$$

$$+ \sum_j \sum_{n=2}^{\infty} [C_{nj} r_j^{-n+1} + D_{nj} r_j^{-n+3}] \mathcal{J}_n(\zeta_j). \tag{3.8}$$

As $|z| \to \infty$, equation (3.8) reduces to

$$[\psi]_{|z| \to \infty} = a_1 R^2 + a_2 R^4 .$$

Therefore, from condition (2.13) requiring a return to Poiseuille flow at infinity, the constants a_1 and a_2 are evaluated as

$$a_1 = \tfrac{1}{2}V \ , \ a_2 = \tfrac{1}{4}V, \tag{3.9}$$

and (3.8) becomes

$$\psi = V\left(\frac{R^2}{2} - \frac{R^4}{4}\right) + \int_0^\infty [A(\lambda)RI_1(\lambda R) + B(\lambda)R^2 I_0(\lambda R)]\cos\lambda z\, d\lambda$$
$$+ \sum_j \sum_{n=2}^{\infty} [C_{nj} r_j^{-n+1} + D_{nj} r_j^{-n+3}] \mathcal{P}_n(\zeta_j) \qquad (3.10)$$

B. The cylinder boundary conditions

Equation (3.10) is written in mixed coordinates -- the cylindrical coordinate system (R,z) and N different spherical coordinate systems (r_j, θ_j; all j). Clearly, in order to differentiate (3.10) and apply boundary conditions at R = 1 it is first necessary to set up a coordinate transformation. With the aid of Figure 1 it can be seen that

$$r_j = [R^2 + (z - jd)^2]^{\frac{1}{2}}$$
$$\zeta_j = \cos\theta_j = \frac{z - jd}{r_j} \qquad (3.11)$$
$$\sin\theta_j = \frac{R}{r_j} .$$

Furthermore,

$$\frac{\partial r_j}{\partial R} = \sin\theta_j$$
$$\frac{\partial \zeta_j}{\partial R} = -\frac{\zeta_j \sin\theta_j}{r_j} \qquad (3.12)$$
$$\frac{\partial}{\partial R}(\sin\theta_j) = \frac{\zeta_j^2}{r_j}$$

$$\frac{\partial r_j}{\partial z} = \zeta_j$$

$$\frac{\partial \zeta_j}{\partial z} = \frac{\sin^2\theta_j}{r_j} \tag{3.13}$$

$$\frac{\partial}{\partial z}(\sin\theta_j) = -\frac{\zeta_j \sin\theta_j}{r_j} .$$

Using (3.11), (3.12), (3.13), and the properties of Gegenbauer and Legendre functions, the z and R velocity components are calculated from (3.10):

$$v_z = \frac{1}{R}\frac{\partial \psi}{\partial R} = V(1-R^2)$$

$$+ \int_o^\infty \left\{A(\lambda)\lambda I_o(\lambda R)+B(\lambda)[\lambda R I_1(\lambda R)+2I_o(\lambda R)]\right\} \cos\lambda z d\lambda \tag{3.14}$$

$$+ \sum_j \sum_{n=2}^{\infty} \left\{C_{nj}P_n(\zeta_j)r_j^{-n-1} + D_{nj}[P_n(\zeta_j)+2\mathcal{J}_n(\zeta_j)]r_j^{-n+1}\right\} ,$$

$$v_R = -\frac{1}{R}\frac{\partial \psi}{\partial z} = \int_o^\infty [A(\lambda)I_1(\lambda R)+B(\lambda)RI_o(\lambda R)]\lambda \sin\lambda z d\lambda$$

$$+ \sum_j \sum_{n=2}^{\infty} \left\{C_{nj}\left[\frac{(n+1)\mathcal{J}_{n+1}(\zeta_j)}{\sin\theta_j}\right] r_j^{-n-1}\right. \tag{3.15}$$

$$\left. + D_{nj}\left[\frac{(n+1)\mathcal{J}_{n+1}(\zeta_j)-2\zeta_j\mathcal{J}_n(\zeta_j)}{\sin\theta_j}\right] r_j^{-n+1}\right\} ,$$

where $P_n(\zeta_j)$ are Legendre functions. To satisfy the no-slip boundary conditions on the wall, equations (3.10) and (3.14)

will be transformed into cylindrical coordinates. Application of the boundary conditions at R = 1 will then result in two Fourier integral representations of two functions of z. Inverting these two equations will give two simultaneous equations for the $A(\lambda)$ and $B(\lambda)$ arbitrary functions, which will be determined in terms of the C_{nj} and D_{nj} coefficients. Substitution of these results back into (3.10) gives an expression which represents flow inside a cylinder with not-as-yet specified disturbances in the flow, and which satisfies the boundary conditions on the cylinder.

Accordingly, the transformation (3.11) is substituted into the spherical terms of (3.10) and (3.14), resulting in expressions for ψ and v_z in terms of R-z cylindrical coordinates only. When the boundary conditions $v_z = 0$ and $\psi = V/4$ from (2.14) are applied at R = 1, the following result is obtained:

$$\int_o^\infty \left\{ A(\lambda)\lambda I_o(\lambda) + B(\lambda)[\lambda I_1(\lambda)+2I_o(\lambda)] \right\} \cos\lambda z d\lambda$$

$$= -\sum_j \sum_{n=2}^{\infty} [C_{nj} F_n^{(1)}(z_j) + D_{nj} F_n^{(2)}(z_j)] \tag{3.16}$$

$$\int_o^\infty [A(\lambda) I_1(\lambda) + B(\lambda) I_o(\lambda)] \cos\lambda z d\lambda$$

$$= -\sum_j \sum_{n=2}^{\infty} [C_{nj} F_n^{(3)}(z_j) + D_{nj} F_n^{(4)}(z_j)] \tag{3.17}$$

where, for brevity,

$$z_j = z - jd, \tag{3.18}$$

and

$$F_n^{(1)}(z_j) = (1+z_j^2)^{-(n+1)/2} P_n\left(\frac{z_j}{\sqrt{1+z_j^2}}\right) \tag{3.19a}$$

$$F_n^{(2)}(z_j) = (1+z_j^2)^{-(n-1)/2} \left[P_n\left(\frac{z_j}{\sqrt{1+z_j^2}}\right) + 2\mathcal{I}_n\left(\frac{z_j}{\sqrt{1+z_j^2}}\right)\right] \tag{3.19b}$$

$$F_n^{(3)}(z_j) = (1+z_j^2)^{-(n-1)/2} \mathcal{I}_n\left(\frac{z_j}{\sqrt{1+z_j^2}}\right) \tag{3.19c}$$

$$F_n^{(4)}(z_j) = (1+z_j^2)^{-(n-3)/2} \mathcal{I}_n\left(\frac{z_j}{\sqrt{1+z_j^2}}\right). \tag{3.19d}$$

The right hand sides of (3.16) and (3.17) are representative, to within the yet-unknown C_{nj} and D_{nj} coefficients, of the spherical disturbances as they are felt on the cylinder wall. These disturbances are functions of the z coordinate only. Although the individual $F_n^{(k)}(z_j)$ functions (k = 1,2,3,4) are even in z_j for even n and are odd in z_j for odd n, the complete right hand sides of (3.16) and (3.17) must be even functions of z, since they represent Stokes flow disturbances by a system which is symmetrical about z = 0.

The left hand sides of (3.16) and (3.17) are seen as Fourier cosine integral representations of their right hand sides. While keeping in mind the discussion of the previous paragraph, these integral representations may be inverted and the resulting equations manipulated somewhat. From (3.16) and (3.17), respectively,

$$A(\lambda)\lambda I_o(\lambda) + B(\lambda)[\lambda I_1(\lambda)+2I_o(\lambda)] = -\Phi(\lambda) \tag{3.20}$$

$$A(\lambda)I_1(\lambda) + B(\lambda)I_o(\lambda) = -\Gamma(\lambda), \tag{3.21}$$

where

$$\Phi(\lambda) = \frac{1}{\pi}\int_{-\infty}^{\infty}\left\{\sum_j \sum_{n=2}^{\infty}[C_{nj}F_n^{(1)}(z_j)+D_{nj}F_n^{(2)}(z_j)]\right\}\cos\lambda z dz$$

$$= \sum_j \sum_{n=2}^{\infty}[C_{nj}G_{nj}^{(1)}(\lambda)+D_{nj}G_{nj}^{(2)}(\lambda)], \tag{3.22}$$

$$\Gamma(\lambda) = \frac{1}{\pi}\int_{-\infty}^{\infty}\left\{\sum_j \sum_{n=2}^{\infty}[C_{nj}F_n^{(3)}(z_j)+D_{nj}F_n^{(4)}(z_j)]\right\}\cos\lambda z dz$$

$$= \sum_j \sum_{n=2}^{\infty}[C_{nj}G_{nj}^{(3)}(\lambda)+D_{nj}G_{nj}^{(4)}(\lambda)]. \tag{3.23}$$

Making use of the even/odd properties of $F_n^{(k)}(z_j)$ and of definition (3.18), the $G_{nj}^{(k)}(\lambda)$ functions (k = 1,2,3,4) can be written as

$$G_{nj}^{(k)}(\lambda) = \frac{1}{\pi}\int_{-\infty}^{\infty} F_n^{(k)}(z_j)\cos\lambda z dz$$

$$= \begin{cases} \frac{2}{\pi}\cos\lambda j d\int_o^{\infty} F_n^{(k)}(z_j)\cos\lambda z_j dz_j, & n \text{ even} \\ -\frac{2}{\pi}\sin\lambda j d\int_o^{\infty} F_n^{(k)}(z_j)\sin\lambda z_j dz_j, & n \text{ odd.} \end{cases} \tag{3.24}$$

Equations (3.20) and (3.21) are now solved simultaneously for the $A(\lambda)$ and $B(\lambda)$ functions. The resulting solutions for $A(\lambda)$ and $B(\lambda)$, along with definitions (3.22) and (3.23) for $\Phi(\lambda)$ and $\Gamma(\lambda)$ are then substituted into the general solution, (3.10), resulting in equation (3.25), below, for the stream function. This new solution for ψ satisfies the boundary conditions on the cylinder wall and contains unspecified disturbances emanating from the spheres. Presented below is the result for ψ and the corresponding velocities v_z and v_R:

$$\psi = V(\frac{R^2}{2} - \frac{R^4}{4}) + \sum_j \sum_{n=2}^{\infty} [C_{nj} S_{nj}^{(1)}(R,z) + D_{nj} T_{nj}^{(1)}(R,z)] \quad (3.25)$$

$$v_z = V(1-R^2) + \sum_j \sum_{n=2}^{\infty} [C_{nj} S_{nj}^{(2)}(R,z) + D_{nj} T_{nj}^{(2)}(R,z)] \quad (3.26)$$

$$v_R = \sum_j \sum_{n=2}^{\infty} [C_{nj} S_{nj}^{(3)}(R,z) + D_{nj} T_{nj}^{(3)}(R,z)], \quad (3.27)$$

where the $S_{nj}^{(k)}(R,z)$ and $T_{nj}^{(k)}(R,z)$ are defined as follows:

$$S_{nj}^{(1)}(R,z) = r_j^{-n+1} \mathcal{J}_n(\zeta_j) + \int_o^{\infty} \xi_{nj}^{(1)}(R,\lambda) \cos\lambda z \, d\lambda \quad (3.28a)$$

$$T_{nj}^{(1)}(R,z) = r_j^{-n+3} \mathcal{J}_n(\zeta_j) + \int_o^{\infty} \phi_{nj}^{(1)}(R,\lambda) \cos\lambda z \, d\lambda \quad (3.28b)$$

$$S_{nj}^{(2)}(R,z) = r_j^{-n-1} P_n(\zeta_j) + \int_o^{\infty} \xi_{nj}^{(2)}(R,\lambda) \cos\lambda z \, d\lambda \quad (3.29a)$$

$$T_{nj}^{(2)}(R,z) = r_j^{-n+1} [P_n(\zeta_j) + 2\mathcal{J}_n(\zeta_j)] + \int_o^{\infty} \phi_{nj}^{(2)}(R,\lambda) \cos\lambda z \, d\lambda \quad (3.29b)$$

$$S_{nj}^{(3)}(R,z) = r_j^{-n-1}\frac{(n+1)\zeta_{n+1}(\zeta_j)}{\sin\theta_j} + \int_o^\infty \xi_{nj}^{(3)}(R,\lambda)\sin\lambda z d\lambda \quad (3.30a)$$

$$T_{nj}^{(3)}(R,z) = r_j^{-n+1}\frac{(n+1)\zeta_{n+1}(\zeta_j)-2\zeta_j\zeta_n(\zeta_j)}{\sin\theta_j} + \int_o^\infty \phi_{nj}^{(3)}(R,\lambda)\sin\lambda z d\lambda \quad (3.30b)$$

The integrand envelope functions $\xi_{nj}^{(k)}(R,\lambda)$ and $\phi_{nj}^{(k)}(R,\lambda)$ are given by

$$\xi_{nj}^{(k)}(R,\lambda) = \frac{1}{H(\lambda)}[h_1^{(k)}(R,\lambda)G_{nj}^{(3)}(\lambda) + h_2^{(k)}(R,\lambda)G_{nj}^{(1)}(\lambda)] \quad (3.31)$$

$$\phi_{nj}^{(k)}(R,\lambda) = \frac{1}{H(\lambda)}[h_1^{(k)}(R,\lambda)G_{nj}^{(4)}(\lambda) + h_2^{(k)}(R,\lambda)G_{nj}^{(2)}(\lambda)], \quad k = 1,2,3$$

where

$$H(\lambda) = \lambda[I_o^2(\lambda)-I_1^2(\lambda)] - 2I_o(\lambda)I_1(\lambda) \quad (3.32)$$

$$h_1^{(1)}(R,\lambda) = R\left\{[\lambda I_1(\lambda)+2I_o(\lambda)]I_1(\lambda R) - \lambda R I_o(\lambda)I_o(\lambda R)\right\} \quad (3.33a)$$

$$h_2^{(1)}(R,\lambda) = R[RI_1(\lambda)I_o(\lambda R) - I_o(\lambda)I_1(\lambda R)] \quad (3.33b)$$

$$h_1^{(2)}(R,\lambda) = \lambda\left\{[\lambda I_1(\lambda)+2I_o(\lambda)]I_o(\lambda R) - I_o(\lambda)[\lambda R I_1(\lambda R)+2I_o(\lambda R)]\right\} \quad (3.34a)$$

$$h_2^{(2)}(R,\lambda) = I_1(\lambda)[\lambda R I_1(\lambda R)+2I_o(\lambda R)] - \lambda I_o(\lambda)I_o(\lambda R) \quad (3.34b)$$

$$h_1^{(3)}(R,\lambda) = \frac{\lambda}{R} h_1^{(1)}(R,\lambda) \tag{3.35a}$$

$$h_2^{(3)}(R,\lambda) = \frac{\lambda}{R} h_2^{(1)}(R,\lambda) \tag{3.35b}$$

The integrations indicated in (3.28), (3.29), and (3.30) are to be carried out numerically. However, their integrand envelope functions, defined by (3.31), involve the $G_{nj}^{(i)}(\lambda)$ functions ($i = 1,2,3,4$) which are defined in integral form in (3.24). These integrals (3.24) must be evaluated analytically before one proceeds with the numerical integrations of (3.28), (3.29), and (3.30). The analytical integrations of (3.24) are presented in detail in the appendix. The results are presented below:

$$\begin{aligned}
G_{nj}^{(1)}(\lambda) &= -\beta_{nj}(\lambda)\lambda^n K_o(\lambda) \\
G_{nj}^{(2)}(\lambda) &= \beta_{nj}(\lambda)\lambda^{n-2}[n(n-1)K_o(\lambda)-(2n-3)\lambda K_1(\lambda)] \\
G_{nj}^{(3)}(\lambda) &= \beta_{nj}(\lambda)\lambda^{n-1} K_1(\lambda) \\
G_{nj}^{(4)}(\lambda) &= \beta_{nj}(\lambda)\lambda^{n-3}[(2n-3)\lambda K_o(\lambda)-(n-2)(n-3)K_1(\lambda)],
\end{aligned} \tag{3.36}$$

where

$$\beta_{nj}(\lambda) = \begin{cases} -(-1)^{n/2} \dfrac{2}{\pi n!} \cos\lambda jd \quad , & n = \text{even} \\ (-1)^{(n-1)/2} \dfrac{2}{\pi n!} \sin\lambda jd \quad , & n = \text{odd} . \end{cases} \tag{3.37}$$

The $K_o(\lambda)$ and $K_1(\lambda)$ functions are the modified Bessel functions of the second kind.

Equation (3.25) is the complete solution to the governing equation, (2.5), and satisfies the boundary conditions at infinity and all along the cylinder wall, R = 1, independently of the C_{nj} and D_{nj} unknown coefficients. These coefficients will now be used to satisfy the appropriate conditions on the surfaces of the spheres.

C. The sphere boundary conditions

The boundary conditions on the sphere surfaces are given by (2.16 a and b): $v_z = U$, $v_R = 0$, where U is the velocity with which all the spheres are moving relative to the tube, and v_z and v_R are given by (3.26) and (3.27). The technique of applying the sphere boundary conditions is analagous to the multipole truncation method employed in solving the unbounded flow problem presented in Gluckman, Pfeffer and Weinbaum (1971).

To satisfy the boundary conditions (2.16) exactly along the entire generating arc of each sphere would require the solution of the entire infinite array of unknown coefficients. The truncation technique satisfies the boundary conditions at a finite number of discrete points on each sphere's generating arc and truncates the infinite series into a finite one. The two unknown coefficients in each inner term in (3.25) permit one to satisfy the exact no-slip boundary conditions (2.16) at one discrete point on each sphere. Thus, if a spherical boundary is to be approximated by satisfying conditions (2.16) at M discrete points on its generating arc, M terms are retained in the inner series expansion of (3.25). If there are N spheres in the chain, this results in a linear set of 2xMxN simultaneous algebraic equations for the $2\times M\times N$ C_{nj} and D_{nj} unknown coefficients of the truncated solution,

$$\psi = V\left(\frac{R^2}{2} - \frac{R^4}{4}\right) + \sum_j \sum_{n=2}^{M+1} \left[C_{nj} S_{nj}^{(1)}(R,z) + D_{nj} T_{nj}^{(1)}(R,z)\right], \quad (3.38)$$

This matrix equation can be solved to yield the unknown constants by any of the standard matrix reduction techniques.

The accuracy of the present truncation technique can be improved to any degree by taking a sufficiently large value of M, the order of the truncation, to within the accuracy achieved in the numerical integrations which are required in evaluating the $S_{nj}(R,z)$ and $T_{nj}(R,z)$ matrix elements [see (3.25) to (3.30]. Naturally, as $M \to \infty$ the truncation error reduces to zero. As will be seen in section 5, the series converges quite rapidly, and very good accuracy is achieved with only a small number of boundary points on each sphere.

4. Viscous Drag Force

The force exerted by the fluid on a spherical boundary r_j = constant is shown in Happel and Brenner (1965) to be

$$F_j = \mu\pi\int_o^{\pi} r_j^3 \sin^3\theta_j \frac{\partial}{\partial r_j}\left[\frac{E^2\psi}{r_j^2\sin^2\theta_j}\right] r_j d\theta_j \ . \tag{4.1}$$

Performing the above integration, using (3.25) and the orthogonality properties of the Gegenbauer functions, results in the simple relationship,

$$F_j = 4\pi\mu D_{2j} \ . \tag{4.2}$$

Equation (4.2) demonstrates that only the first order term (n=2) of the inner series of (3.25) contributes to the drag forces exerted on each submerged sphere.

The classical Stokes result for the drag force on an isolated sphere is

$$F = 6\pi\mu Ua \ , \tag{4.3}$$

The drag force on a sphere moving through a fluid in the presence of other solid boundaries can be expressed in terms of a convenient drag correction factor, λ. Two drag correction factors are defined: $\lambda^{(U)}$ for spheres moving through a stationary fluid, and $\lambda^{(V)}$ for stationary spheres in a moving fluid whose velocity is given by the Poiseuille profile far downstream.

For spheres moving with velocity U through an otherwise stationary fluid (V=0), we have, for sphere j,

$$F_j = 4\pi\mu D_{2J}^{(U)} = 6\pi\mu aU\lambda_j^{(U)} , \tag{4.4}$$

and hence

$$\lambda_j^{(U)} = \frac{D_{2j}^{(U)}}{1.5aU} . \tag{4.5}$$

That is, $\lambda_j^{(U)}$ is the ratio of the drag force on sphere j to that on a single sphere moving with velocity U through a quiescent unbounded fluid. In the case of fluid flow past stationary spheres (U=0), we have

$$F_j = 4\pi\mu D_{2j}^{(V)} = -6\pi\mu aV\lambda_j^{(V)} \tag{4.6}$$

and hence

$$\lambda_j^{(V)} = -\frac{D_{2j}^{(V)}}{1.5aV} . \tag{4.7}$$

Here, too, $\lambda_j^{(V)}$ is seen as the ratio of F_j to the drag force on a single stationary sphere in an infinite fluid moving with uniform velocity V. The negative sign arises from the fact that the $D_{zj}^{(V)}$ are necessarily negative.

When both the fluid and spheres are moving, the linearity of the equation of motion suggests that the net drag is the algebraic sum of the two drag forces discussed above, i.e.,

$$D_{2j} = D_{2j}^{(U)} + D_{2j}^{(V)} . \tag{4.8}$$

Therefore,

$$F_j = 4\pi\mu D_{2j} = 4\pi\mu[D_{2j}^{(U)} + D_{2j}^{(V)}] , \tag{4.9}$$

and

$$F_j = 6\pi\mu a[U\lambda_j^{(U)} - V\lambda_j^{(V)}] . \tag{4.10}$$

It is thus necessary to consider only cases in which U = 0 or V = 0, and to consider the problem of combined fluid and sphere velocities as a superposition of its component problems.

A number of possible applications of equation (4.10) come to mind. Consider a doublet (two spheres) suspended in a vertical tube in which fluid is being pumped upward. The flowrate required to keep the spheres stationary against the gravitational field is sought. Setting U = 0 and equating F_j to the force of gravity, one finds from equation (4.10) that

$$V = \frac{U_t}{\lambda^{(V)}} ,$$

where U_t is the infinite medium isolated sphere terminal settling velocity, $U_t = 2a^2(\rho_{sphere} - \rho)g/9\mu$.

Another interesting application, which involves the simultaneous motion of fluid and particles, is the zero-drag motion of spheres in a Poiseuille flow. When the particles are free to move along with the fluid and there are no body forces present in the direction of motion, they will tend to travel with different velocities (unless the flow is uniform) which are such that the net drag force on each sphere is zero. Equation (4.10) indicates that this requires the fluid resistance to the motion of a sphere to exactly cancel the convective pull of the moving fluid, for each sphere of the chain. Although these zero-drag sphere velocities can be calculated from (4.10),

$$\frac{U_j}{V} = \frac{\lambda_j^{(V)}}{\lambda_j^{(U)}} , \text{ all } j, \qquad (4.11)$$

their solution in this manner is cumbersome, since (4.11) is a set of nonlinear simultaneous equations for the velocities U_j, $\lambda_j^{(U)}$ being functions of U_j.

A simpler and more direct approach is available, in solving the set of linear simultaneous algebraic equations for the unknown C_{nj} and D_{nj} coefficients, resulting from the application of boundary conditions on the sphere surfaces of an N-sphere chain. The N D_{2j} coefficients are set to zero, and their places are replaced by the N U_j velocity terms by transposition of the proper terms from the right to the left hand sides. The number of equations and unknowns thus preserved, the matrix equation is then solved for the sphere velocities along with the rest of the C_{nj} and D_{nj} coefficients.

Another application is the calculation of wall correction factors to experimental data. In general, information about particle dynamics in an infinite medium is obtained by dropping spheres in a large vessel and measuring their terminal settling velocities. If the drag force exerted on each sphere when two spheres fall in an infinite viscous fluid is compared with that exerted on a single sphere, we have, by (4.4)

$$\lambda_\infty = \frac{U_{I\infty}}{U_{II\infty}} \,. \tag{4.12}$$

Here $U_{I\infty}$ and $U_{II\infty}$ are the settling velocities of one sphere and two spheres, respectively, in an infinite fluid, and λ_∞ is the two-sphere drag correction factor in an infinite medium. To correct the experimentally measured velocities for the influence of a finite sized cylindrical boundary, the factors k_I and k_{II} are defined, e.g., see Happel and Pfeffer (1960) so that

$$\lambda_\infty = \frac{k_I U_I}{k_{II} U_{II}} \cdot \tag{4.13}$$

Here k_I and k_{II} are wall correction factors for one and two spheres, accounting solely for the influence of the tube wall. Also, in (4.13), λ_∞ is the particle interaction parameter for an infinite medium, accounting solely for inter-particle interaction effects, while U_I and U_{II} are the experimentally observed one-sphere and two-sphere terminal settling velocities.

The wall-sphere interactions are thus effectively separated from the sphere-sphere interaction effects, giving wall interaction parameters which can be used to correct experimental data. If λ is the overall drag correction factor, defined by (4.4) or (4.6), including both wall and inter-particle interactions, it is easily seen that (4.13) reduces to

$$\lambda = \lambda_\infty k_{II} \, . \tag{4.14}$$

Equation (4.14) will be used to calculate the wall correction factors for two spheres, k_{II}, and also for three spheres, k_{III}.

5. Solutions for One Sphere

Solutions, using the truncation technique, to the problem of axisymmetric slow viscous flow past one sphere moving along the centerline of a long cylindrical tube will be presented in this section. This problem was chosen since its solution has already been presented by Haberman and Sayre (1958), providing a convenient comparison for the present analysis in the special case of a single-sphere chain.

The most accurate lowest order truncation solution for the viscous drag force is obtained by choosing one point at $\theta_j = \pi/2$ on the sphere's semi-circular generating arc for satisfying the no-slip boundary conditions. This point is the most advantageous since it controls the projected area as well as the sphere-to-cylinder diameter ratio of the boundary shape approximating the sphere. Additional points are selected as mirror-image pairs about the line $\theta_j = \pi/2$ in order to preserve the geometric symmetry of the spherical boundary shape about this line. The procedure used in the present analysis for spacing these points along each boundary was to divide the half arc of the sphere into equal segments.

An examination of the system of linear algebraic equations resulting from the simultaneous application of no-slip conditions at all the boundary points shows that when the $\theta_j = \pi/2$ point is used, the coefficient matrix becomes singular and the equations are linearly dependent. In order to overcome this difficulty, the top point can be considered to be a combination of two closely adjacent points, i.e., $\theta_j = \pi/2 \pm \alpha$. The optimum value of α is found by obtaining solutions for one sphere, at several different diameter ratios, with the boundary conditions being satisfied exactly at only the two points $\theta_j = \pi/2 \pm \alpha$ (M=2), for

a succession of angles α. The largest value for α for which convergence to a desired accuracy is obtained is then chosen. These results are presented in Table 1. Examination of Table 1

α	Diameter ratio, a = 0.1		a = 0.4		a = 0.6	
	$\lambda^{(U)}$	$\lambda^{(V)}$	$\lambda^{(U)}$	$\lambda^{(V)}$	$\lambda^{(U)}$	$\lambda^{(V)}$
5^{o}	1.2630	1.2499	3.7811	3.1302	24.127	14.277
3^{o}	1.2638	1.2507	3.8352	3.1917	25.251	15.709
2^{o}	1.2640	1.2513	3.8770	3.2380	25.862	16.510
1^{o}	1.2641	1.2514	3.8895	3.2688	26.489	16.956
0.9^{o}	1.2641	1.2515	3.8902	3.2677	26.491	16.957
0.8^{o}	1.2641	1.2515	3.8905	3.2682	26.493	16.958
0.7^{o}	1.2641	1.2515	3.8905	3.2682	26.493	16.958

Table 1. Drag factors for one sphere, M=2. Convergence tests for optimum α.

reveals that both $\lambda^{(U)}$ and $\lambda^{(V)}$ converge to five significant figures for all sphere-to-cylinder diameter ratios, a, when $\alpha \leq 0.8^{o}$. Consequently, α was taken as 0.8^{o} in all problems treated in this study, and these two top points at $\theta_j = 89.2^{o}$ and $\theta_j = 90.8^{o}$ were considered to be the single high point required.

Before meaningful results can be presented, the fundamental question of convergence remains to be answered. We must resolve the question of what order truncation solution is necessary in order to achieve results of prescribed accuracy; i.e., at how many points on the generating arc of each sphere should the boundary conditions be satisfied in order for a given accuracy to be achieved. Since only an infinite number of points on the

generating arc can describe a perfect sphere, the discrete point representation used in the present study can only describe a distorted boundary shape. This results in errors in the calculated drag force and velocity field. However, since the projected area of the distorted boundary normal to the flow direction is the same as that for a perfect sphere, the drag force should not be greatly affected by the number of boundary points used. This is especially true for a single sphere or for widely spaced spheres. However, for closely spaced spheres, the inter-particle shielding effect becomes somewhat dependent on the boundary shape, resulting in an increased drag error. Similarly, since the top boundary point sets the diameter ratio, a, the drag force on a single sphere is expected to vary only slightly with moderate distortions in the boundary shape when the sphere is small. However, in the case of a large sphere, the exact boundary shape plays a greater role in the sphere-cylinder interaction, and consequently the solution is expected to converge more slowly.

We conclude, therefore, that the minimum M required to achieve a prescribed accuracy should be a function of the sphere-to-cylinder diameter ratio and of the sphere spacing. To obtain a more quantitative answer, the convergence characteristics of the one and two sphere problems were examined over a range of diameter ratios and spacings. Table 2 shows the drag correction factors, $\lambda^{(U)}$ and $\lambda^{(V)}$, on a single sphere for various M and a. It is seen that convergence to four significant figures is obtained when the boundary conditions are satisfied at a surprisingly small number of points on the sphere's generating arc. Even at a = 0.8 only fifteen points are required, and the convergence is remarkably fast at the lower diameter ratios -- five

Diameter ratio, a	Number of points, M	$\lambda^{(U)}$	$\lambda^{(V)}$
0.1	1	1.264	1.252
	3	1.263	1.255
	5	1.263	1.255
0.3	1	2.429	2.211
	3	2.372	2.231
	5	2.373	2.231
	7	2.373	2.231
0.5	1	7.575	5.682
	3	5.936	4.989
	5	5.975	5.018
	7	5.973	5.017
	9	5.973	5.017
0.7	1	-38.73	-19.76
	3	21.60	15.66
	5	25.59	18.08
	7	25.26	17.89
	9	25.30	17.91
	11	25.29	17.91
	13	25.29	17.91

Table 2. Convergence of one-sphere solutions at various diameter ratios.

points at a = 0.3, three points at a = 0.1. (As $a \to 0$, equation (3.38) reduces to the exact single isolated sphere Stokes solution, with M = 1.) This rapid convergence is in dramatic contrast to the convergence of the method of reflections solution employed previously by others and discussed in section 1. It should be noted that the error resulting from the application of the present truncation technique ranges from 0.022% at a = 0.3 to 14.6% at a = 0.7 when only three points on the generating arc are used.

Haberman and Sayre (1958) also obtained the solution for a single sphere moving along the axis of an infinite cylinder. Their method of solution, which is inapplicable to the multisphere problem, is described in general terms in section 1. Table 3 compares the drag correction factors obtained by the present truncation method to the solutions of Haberman and Sayre.

a	λ (U)	λ(V)	Haberman & Sayre		Wang & Skalak	
			λ(U)	λ(V)	λ(U)	λ(V)
0.0	1.000	1.000				
0.1	1.263	1.255	1.263	1.255	1.263	1.255
0.2	1.680	1.636	1.680	1.635	1.680	1.635
0.3	2.373	2.231	2.371	2.231	2.370	2.229
0.4	3.599	3.223	3.596	3.218	3.592	3.216
0.5	5.973	5.017	5.970	5.004	5.949	4.996
0.6	11.20	8.696	11.14	8.651	11.10	8.617
0.7	25.29	17.91	24.96	17.67	24.70	17.49

Table 3. Comparison of one-sphere solutions with results of Haberman & Sayre (1958). Wang & Skalak solutions are for an infinite chain of spheres which are 40 cylinder radii apart.

Their solutions also utilize a truncation technique in which an infinite set of simultaneous algebraic equations is truncated and solved. This system of equations is different from that of the present method and may exhibit different convergence properties from those exhibited in Table 2.

Haberman and Sayre present an approximate solution,

$$\lambda^{(U)} = \frac{1-0.75857a^5}{1-2.1050a+2.0865a^3-1.7068a^5+0.72603a^6}$$

$$\lambda^{(V)} = \frac{1-2/3a^2-0.20217a^5}{1-2.1050a+2.0865a^3-1.7068a^5+0.72603a^6} \qquad (5.1)$$

derived by keeping two equations and two unknowns from the infinite set of equations. In Figure 2 the results of the present theory are plotted along with Haberman's final results and his lower-order truncation solution, equation (5.1). The Haberman results and the present solutions agree to within 0.5 percent for diameter ratios of up to 0.6, but differ somewhat as the sphere radius approaches unity. It should be noted that the present results listed are converged solutions, and that the inclusion of additional higher-order terms by increasing the number of boundary points results in no significant improvement. However, a number of questions may be raised. As seen in Figure 2, Haberman's final results consistently fall above his lower-order approximation and below the present theory's results. This would seem to raise a question concerning the complete convergence of the Haberman and Sayre solutions. On the other hand, Wang and Skalak (1969) present drag solutions for an infinite chain of spheres as the inter-sphere spacing grows large, and these results, Table 3, approach the Haberman and Sayre solutions. This seems to lend support to the latter results, although the

largest spacing presented by Wang and Skalak is 40 tube radii, which in view of the slow decay properties of Stokes flow disturbances cannot be considered as infinite. On examination of the present solution technique, the discrepancy may be seen as due to the distortion of the spherical boundary shape resulting from the discrete rather than continuous application of boundary conditions on the sphere surface. As M increases, the shape distortion converges to true sphericity, but does so very slowly. The effect of this distortion on the sphere-wall interaction is then significantly only at the larger diameter ratios.

In view of the above discussion, a further look into the problem is certainly warranted. For example, a possible course would examine the convergence of the present solution with increasing M, but with the boundary points concentrated near the top of the sphere, thus correcting the distortion near the tube wall.

The drag correction factor $\lambda^{(U)}$ is seen to be consistently greater than $\lambda^{(V)}$ (Figure 2). This is due to the choice of reference velocities used in the definitions (4.4) and (4.6). The reference drag force used in these definitions is that experienced by a single stationary sphere immersed in a flow of uniform velocity U or V. In the case of a sphere translating in a bounded quiescent fluid, the undisturbed fluid is seen as flowing with a mean velocity U relative to the sphere; the same uniform velocity U is also used to compute the reference drag force for $\lambda^{(U)}$. In the case of a stationary sphere immersed in a Poiseuille flow (2.11), the reference velocity used in $\lambda^{(V)}$ is the centerline velocity V, although the mean undisturbed fluid velocity seen by a non-vanishing small sphere is less. For this reason, $\lambda^{(V)} < \lambda^{(U)}$ for all $a > 0$.

6. Solutions for Multiple Spheres

In the previous section solutions for the flow past one sphere were presented, tested for convergence, and compared to published results. This section will examine the solutions for flow in a tube past finite chains of spheres. To the best of the authors' knowledge exact solutions for finite chains of two or more spheres inside a tube do not exist in the literature.

In the previous section the convergence properties of the solutions were examined as a function of the sphere-to-cylinder diameter ratio. In the case of multiple spheres, the rate of convergence deserves examination as a function of particle spacing also. To this end, a number of solutions to the two sphere problem at various diameter ratios and sphere spacings are presented in Table 4. Each problem is solved several times with an increasing number of boundary points, M. Since the inter-sphere interaction is adversely affected by the boundary shape distortions resulting from using a finite number of points, M, the solutions are expected to converge more slowly for the two sphere problem than they did for a single sphere. Therefore, the starting value of M for a given case in Table 4 is the optimum M corresponding to the given diameter ratio, reported in Table 2 for a single sphere.

As expected, the solution is seen to converge faster at the greater spacing. In the most difficult case of spheres touching ($d/2a=1$) the minimum number of points required for a solution which is accurate to four significant figures ranges from seven at $a = 0.1$ to fifteen at $a = 0.7$ (and also at $a = 0.8$). Thus, while the inter-particle interactions have an adverse effect on the convergence rate, the solution still converges quite rapidly.

Diameter ratio, a	Number of points, M	d/2a = 1		d/2a = 2	
		$\lambda^{(U)}$	$\lambda^{(V)}$	$\lambda^{(U)}$	$\lambda^{(V)}$
0.1	3	0.9306	0.8880	1.078	1.006
	5	0.9321	0.8899	1.077	1.005
	7	0.9328	0.8907	1.077	1.005
	9	0.9328	0.8907	1.077	1.005
0.3	5	2.072	1.917	2.320	2.117
	7	2.076	1.920	2.320	2.117
	9	2.076	1.920	2.320	2.117
0.5	7	5.654	4.913	5.968	4.987
	9	5.655	4.909	5.968	4.988
	11	5.656	5.911	5.968	4.988
	13	5.656	4.911	5.968	4.988
0.7	11	24.39	17.47	25.28	17.50
	13	24.42	17.46	25.28	17.50
	15	24.41	17.46	25.28	17.50
	17	24.41	17.46	25.28	17.50

Table 4. Convergence of two-sphere solutions at various diameter ratios, for sphere spacings d/2a = 1 (touching) and d/2a = 2.

Before proceeding with presentation and analysis of the solutions, we shall demonstrate the proper approach of the drag results as $a \to 0$ to the values predicted by the unbounded Stokes flow theory for two spheres of Stimson and Jeffery (1926) and for three spheres by Gluckman, Pfeffer and Weinbaum (1971). Table 5 shows the asymptotic behavior for one sphere and for two and three spheres at two different spacings.

Solutions to flow past chains containing 1, 2, 3, 5, 7 and 9 spheres have been obtained, with the boundary conditions being satisfied at a sufficiently large number of points to achieve proper convergence to four significant figures. Since solution of the flow past N spheres with M boundary-condition points on each generating arc involves the reduction of a 2xMxN by 2xMxN matrix equation, in which each element of the coefficient matrix is evaluated by a numerical integration routine (integration limits from zero to infinity), the computing time can become a serious practical limitation. Hence, care must be taken to construct the computer program efficiently, minimizing operation times associated with indexing, accessing, looping, etc. In addition, the computing time can be halved by making use of the symmetry of the solution about the $z = 0$ plane. Because of this symmetry and the symmetric and antisymmetric properties of the Legendre and Gegenbauer functions, it is easily verified that the $S_{nj}^{(k)}(R,z)$ and $T_{nj}^{(k)}(R,z)$ matrix elements obey the relation

$$\left.\begin{aligned} S_{n,-j}^{(k)}(R,-z) &= (-1)^{n+k} S_{nj}^{(k)}(R,z) \\ T_{n,-j}^{(k)}(R,-z) &= (-1)^{n+k} T_{nj}^{(k)}(R,Z) \end{aligned}\right\} \quad k = 2,3 \qquad (6.1)$$

a	$\lambda^{(U)}$								
	One sphere	Two spheres		Three spheres					
		d/2a=1	d/2a=2	d/2a = 1			d/2a = 1.5		
		Spheres -1&1	Spheres -1&1	Sphere -1	Sphere 0	Sphere 1	Sphere -1	Sphere 0	Sphere 1
0.4	3.599	3.339	3.583	3.191	2.753	3.191	3.409	3.168	3.409
10^{-1}	1.263	0.9328	1.077	0.8613	0.5077	0.8613	0.9633	0.6938	0.9633
10^{-2}	1.022	0.6632	0.7662	0.6196	0.3538	0.6196	0.6707	0.4611	0.6707
10^{-3}	1.002	0.6469	0.7446	0.6082	0.3273	0.6082	0.6486	0.4459	0.6486
10^{-4}	1.0002	0.6453	0.7425	0.6064	0.3263	0.6064	0.6465	0.4444	0.6465
10^{-5}	1.0000	0.6452	0.7423	0.6062	0.3262	0.6062	0.6463	0.4443	0.6463
0 unbounded theory	1.000	0.6452	0.7423	0.6062	0.3262	0.6062	0.6462	0.4442	0.6462

Table 5. Asymptotic values of the calculated $\lambda^{(U)}$ as $a \to 0$, for one, two, and three spheres.

Therefore, only the $2M^2N^2$ matrix elements associated with the boundary conditions at points on one side of the symmetry plane must be evaluated via numerical integration, while the other $2M^2N^2$ elements are formed from (6.1).

Actual computer running times on the IBM 370/168 for the solution of one problem were found to be approximately $[\frac{1}{4}(M+1)N]^2$ seconds, ranging from 3 seconds for one sphere with five points to 21 minutes for nine spheres with fifteen points per generating arc. It was, therefore, out of the realm of practicality to obtain converged solutions for chains containing more than nine spheres.

Since the accuracy of the converged solutions is limited by the accuracy of the numerical integrations, extreme care must be taken to obtain integrated values whose accuracy is within that of the overall problem.

The results for two sphere chains are shown in Figures 3 and 4. The one sphere solutions and Wang and Skalak's (1969) infinite chain results are also shown for reference. Since the effect of inter-sphere interactions is a reduction in drag force, the drag is seen to decrease with increasing chain length and narrowing interparticle gaps. The effect of the enclosing boundary, however, is a marked increase in the drag force which rises beyond bound as the lubrication limit is approached between the spheres and the tube wall. For $a \to 0$, the results approach their unbounded-flow values, as expected.

The results for $a = 0.2$, $d/2a = 1$ and 2 are plotted in Figure 5 for chains containing different numbers of spheres, and are shown again in Figure 6 for $a = 0.5$. The values for $\lambda^{(U)}$ for the infinite chain of Wang and Skalak (1969) are also shown. Solid lines connect the discrete values to denote individual

chains. It is seen that with increasing chain length, the drag on the central and end spheres decreases, demonstrating the shielding characteristic of the interparticle interactions. The shielding effect is seen even more vividly by the rapid change in drag as the end of a chain is approached, due to the fact that the end spheres receive the least amount of interactive shielding. The behavior of these end spheres with increasing chain length is underscored by the dashed curves. Note that the single-sphere point is common to both families of curves. It is further noted that the shielding effects discussed above are very strong at $d/2a = 1$, but are reduced, or damped, drastically at $d/2a = 2$, particularly at the higher diameter ratio. This demonstrates the damping effect which the tube wall has on the interaction forces.

The wall damping is illustrated more clearly in Figures 7 and 8, for five-sphere chains having various spacings at diameter ratios of 0.2 and 0.5, respectively. The curve for $d/2a = \infty$ is simply the single sphere result. As the spacing increases, the drag forces are observed to rise, and the resulting curves become progressively flatter as the amount of shielding exercised decreases. The striking feature to be noted, however, is that the degree of interparticle interaction, or shielding, as indicated for each chain by the curvature of its drag curve and by its rate of approach to the $d/2a = \infty$ curve, decreases more rapidly at the high diameter ratio. Thus, while the diameter ratio has little effect on the degree of shielding within closely packed chains, it appears to have a strong damping effect as the chain dilutes.

The values of U/V for zero-drag motion were also determined. The effect of increasing the diameter ratio is to decrease the

mean Poiseuillian velocity seen by the spheres and hence to reduce the zero-drag velocities. The effect of the inter-sphere interaction is to decrease the sphere velocities due to the transmission of the centerline velocity defect of each sphere to the boundaries of all the other spheres. This behavior is just the reverse of what is observed for a chain of spheres falling under gravity in a quiescent fluid.

The values of U/V for one sphere are plotted against diameter ratios in Figure 9. Also shown, for reference, are the infinite chain results of Wang and Skalak (1969) for $d/2a = 1$. The third curve is the approximate results obtained in Leichtberg, Weinbaum and Pfeffer (1975) for a single sphere moving with zero drag along the centerline of a parabolic fluid velocity profile in an unbounded medium, i.e., in a fictitious Poiseuille flow $v = V(1-R^2)$ which exists without a solid wall at R=1. It is seen in Figure 9 that the tube wall has no effect on the sphere's velocity for $a < 0.2$, and exerts a modest influence at the higher diameter ratios. Similar behavior is observed for the motion of two spheres since the two sphere interaction does not result in end effects. A comparison of the results for chains of three or more spheres, however, shows that the wall exerts a significant influence on the intra-chain, inter-sphere interaction.

Figure 10 presents the zero-drag velocities of chains of various length, with $a = 0.5$ and $d/2a = 1.1$. The interactions and end effects are clearly demonstrated, with the outer spheres of a given chain moving faster than the central spheres, while increasing chain length tends to decrease the sphere velocities.

The effect of the diameter ratio is, as noted previously, to decrease U/V. Its influence on the inter-sphere relative

velocities requires a somewhat closer look. In the limit of vanishing diameter ratio, the particles move in a flow field which is uniform in its undisturbed state. Consequently, $\lambda_j^{(U)} = \lambda_j^{(V)}$ since the two cases differ by merely a frame of reference, with the result that U/V = 1 for all the spheres. That is, there is no interaction between the particles. As the diameter ratio increases, however, particle interaction effects appear due to the non-uniform velocity profile. Further increases in diameter ratio bring the wall interaction into play, and the damping effects discussed previously become progressively more prominent. Thus, the degree of interparticle interactions is small for $a < 0.1$, reaches a maximum in the approximate range $0.3 < a < 0.4$, and is quickly damped out for $a > 0.5$, particularly in chains of medium concentration.

Figures 11 and 12 present U/V for five-sphere chains at various spacings, with diameter ratios of 0.3 and 0.5, respectively. A comparison of the two figures shows that, while the damping effect associated with the higher diameter ratio is of relatively little importance to the closely-packed chains, $d/2a = 1.1$ and 1.3, it is of much larger significance to the chains with larger spacing.

Also noted from Figures 10-12 is the fact that the interaction effects in the zero-drag motion are roughly two orders of magnitude smaller than those presented earlier for sphere motion with constrained rather than free sphere velocities.

Table 6 presents, for the sake of completeness, the zero drag velocities of one and two sphere chains.

The wall correction factors which were discussed in section 4 were calculated, and the results are presented in the form of correlation equations. These equations are valid only

a	1 sphere	2 spheres	
		d/2a = 1	d/2a = 2
0.0	1.000	1.000	1.000
0.1	0.9935	0.9926	0.9932
0.2	0.9734	0.9705	0.9727
0.3	0.9404	0.9378	0.9400
0.4	0.8957	0.8882	0.8953
0.5	0.8400	0.8329	0.8397
0.6	0.7763	0.7713	0.7761
0.7	0.7081	0.7042	0.7080
0.8	0.6378	0.6369	0.6378

Table 6. Zero-drag velocities, U/V, for one and two sphere chains.

for small sphere-tube diameter ratio, a. The relations are listed below, along with their ranges of validity and percent errors.

(i) Two spheres translating in a stationary fluid. Validity limited to close spacings, $1 \leq d/2a \leq 2$. Error of 0.2% at a = 0.1, 1.4% at a = 0.2.

$$k_{II}^{(U)} = \exp[a(3.6591+0.4594a)]. \tag{6.2}$$

(ii) Two spheres translating in a stationary fluid. Valid at all spacings, $1 \leq d/2a < \infty$. Maximum error of 0.5% for $a \leq 0.2$.

$$k_{II}^{(U)} = 1 + 1.86a + 7.7a^2 + 5.552a\left(\frac{2a}{d}\right) + 1.39a^2\left(\frac{2a}{d}\right) - 4.228a\left(\frac{2a}{d}\right)^2 + 3.66a^2\left(\frac{2a}{d}\right)^2. \tag{6.3}$$

(iii) Two stationary spheres in a Poiseuille flow. Validity limited to close spacings $1 \leq d/2a \leq 2$. Error of 1% at $a = 0.1$, 2% at $a = 0.2$.

$$k_{II}^{(V)} = \exp[a(2.8376 + 2.9043a)], \tag{6.4}$$

(iv) Two stationary spheres in a Poiseuille flow. Valid at all spacings, $1 \leq d/2a < \infty$. Maximum error of 0.7% for $a \leq 0.2$.

$$k_{II}^{(V)} = 1 + 1.92a + 6.3a^2 + 1.1925a\left(\frac{2a}{d}\right) + 15.115a^2\left(\frac{2a}{d}\right) - 0.599a\left(\frac{2a}{d}\right)^2 - 8.49a^2\left(\frac{2a}{d}\right)^2 \tag{6.5}$$

(v) Three spheres translating in a quiescent fluid. Validity limited to close spacings $1 \leq d/2a \leq 2$. Maximum error for $a \leq 0.2$ is 5.0% for equation (6.6) and 2.3% for (6.7).

$$k_{III}^{(U)} = \exp[a(3.7051 + 0.5089a)], \text{ end spheres} \tag{6.6}$$

$$k_{III}^{(V)} = \exp[a(2.7745 + 16.675a)] \text{ inner sphere.} \tag{6.7}$$

Equations (6.2), (6.4), (6.6) and (6.7) are of the form: $k = \exp[a(C_o + C_1 a)]$ where C_o and C_1 are arbitrary constants. This form was chosen because of the near linearity of $\ln\lambda(a)$ at small diameter ratios, as evidenced in Figures 3 and 4. The coefficients C_o and C_1 were determined by fitting the above equation to the data at $a = 0.0$, 0.1, 0.2. Equations (6.3) and (6.5) were derived by fitting the form

$$k = c_o(a) + c_1(a)\left(\frac{2a}{d}\right) + c_2(a)\left(\frac{2a}{d}\right)^2$$

$$c_i(a) = p_i + q_i a + r_i a^2 \quad , \quad i = 0,1,2$$

where $p_o = 1$, $p_1 = p_2 = 0$ to satisfy the asymptotic condition that k approaches unity as a approaches zero for any value of 2a/d,

to the data for 2a/d = 0.0, 0.5, 1.0 and a = 0.0, 0.1, 0.2. The accuracy of equations (6.2) to (6.7) was checked at the test data points as well as at intermediate values.

Appendix

The analytical integrations required for the closed-form evaluation of the $G_{nj}^{(k)}(\lambda)$ functions, equation (3.24) are presented here. We bring forward equations (3.25) and (3.19).

$$G_{nj}^{(k)}(\lambda) = (-1)^n \frac{2}{\pi} \begin{Bmatrix} \cos\lambda j d \\ \sin\lambda j d \end{Bmatrix} \int_0^\infty F_n^{(k)}(x) \begin{Bmatrix} \cos\lambda x \\ \sin\lambda x \end{Bmatrix} dx \qquad (A.1)$$

$$\begin{Bmatrix} n = \text{even} \\ n = \text{odd} \end{Bmatrix},$$
$$k = 1,2,3,4$$

where

$$F_n^{(1)}(x) = (1+x^2)^{-(n+1)/2} P_n\left(\frac{x}{\sqrt{1+x^2}}\right) \qquad (A.2a)$$

$$F_n^{(2)}(x) = (1+x^2)^{-(n-1)/2} \left[P_n\left(\frac{x}{\sqrt{1+x^2}}\right) + 2\mathcal{J}_n\left(\frac{x}{\sqrt{1+x^2}}\right)\right] \qquad (A.2b)$$

$$F_n^{(3)}(x) = (1+x^2)^{-(n-1)/2} \mathcal{J}_n\left(\frac{x}{\sqrt{1+x^2}}\right) \qquad (A.2c)$$

$$F_n^{(4)}(x) = (1+x^2)^{-(n-3)/2} \mathcal{J}_n\left(\frac{x}{\sqrt{1+x^2}}\right). \qquad (A.2d)$$

These eight integrals will be evaluated by inductive reasoning, using the relations of the Legendre and Gegenbauer functions. We begin with the Fourier integral representation of the modified Bessel function of the second kind (see Abramowitz and Stegun (1965)),

$$K_i(\lambda) = \pi^{-\frac{1}{2}}\left(\frac{2}{\lambda}\right)^i \Gamma(i+\tfrac{1}{2})\int_0^\infty (1+x^2)^{-i-\frac{1}{2}}\cos\lambda x\,dx\ ,\quad i=0,1,2,\ldots \qquad (A.3)$$

Equation (A.3) can be inverted into

$$\frac{2}{\pi}\int_0^\infty \lambda^i K_i(\lambda)\cos\lambda x\,d\lambda = \pi^{-\frac{1}{2}}2^i\Gamma(i+\tfrac{1}{2})(1+x^2)^{-i-\frac{1}{2}}\ ,\quad i=0,1,2,\ldots \qquad (A.4)$$

We now prove that

$$\frac{2}{\pi}\int_0^\infty \lambda^n K_0(\lambda)\cos[\lambda x-(n-2)\tfrac{\pi}{2}]d\lambda = -n!\,(1+x^2)^{-(n+1)/2}P_n\left(\frac{x}{\sqrt{1+x^2}}\right), \qquad (A.5)$$

$$n \geq 0.$$

With $i = 0$, (A.4) reduces to

$$\frac{2}{\pi}\int_0^\infty K_0(\lambda)\cos\lambda x\,d\lambda = (1+x^2)^{-\frac{1}{2}}P_0\left(\frac{x}{\sqrt{1+x^2}}\right) = (1+x^2)^{-\frac{1}{2}}$$

Successive differentiations with respect to x yield,

$$-\frac{2}{\pi}\int_0^\infty \lambda K_0(\lambda)\sin\lambda x\,d\lambda = -x(1+x^2)^{-3/2}$$

$$= -(1+x^2)^{-1}P_1\left(\frac{x}{\sqrt{1+x^2}}\right),$$

$$-\frac{2}{\pi}\int_0^\infty \lambda^2 K_0(\lambda)\cos\lambda x\,d\lambda = (1+x^2)^{-3/2}\left(\frac{3x^2}{1+x^2}-1\right)$$

$$= 2(1+x^2)^{-3/2}P_2\left(\frac{x}{\sqrt{1+x^2}}\right).$$

The last three equations verify (A.5) for n = 0,1,2, respectively. We now differentiate (A.5) with respect to x utilizing the relationships between the Legendre and Gegenbauer functions.

$$-\frac{2}{\pi}\int_0^\infty \lambda^{n+1} K_0(\lambda)\sin[\lambda x-(n-2)\tfrac{\pi}{2}]d\lambda$$

$$= -n!(n+1)(1+x^2)^{-(n+2)/2}\left[n\mathcal{J}_{n+1}\left(\frac{x}{\sqrt{1+x^2}}\right)-\frac{x}{\sqrt{1+x^2}}P_n\left(\frac{x}{\sqrt{1+x^2}}\right)\right]$$

$$= (n+1)!(1+x^2)^{-(n+2)/2}P_{n+1}\left(\frac{x}{\sqrt{1+x^2}}\right).$$

Since $\sin[\lambda x-(n-2)\pi/2] = \cos[\lambda x-(n-1)\pi/2]$, this completes the inductive proof of (A.5) for all $n \geq 0$.

A similar proof now follows for the following relation

$$\frac{2}{\pi}\int_0^\infty \lambda^{n-1} K_1(\lambda)\cos[\lambda x-(n-2)\tfrac{\pi}{2}]d\lambda = n!(1+x^2)^{-(n-1)/2}\mathcal{J}_n\left(\frac{x}{\sqrt{1+x^2}}\right), \qquad (A.6)$$

$$n \geq 2.$$

Equation (A.4), with i = 1, reduces to

$$\frac{2}{\pi}\int_0^\infty \lambda K_1(\lambda)\cos\lambda x\,d\lambda = (1+x^2)^{-3/2} = 2(1+x^2)^{-\frac{1}{2}}\mathcal{J}_2\left(\frac{x}{\sqrt{1+x^2}}\right).$$

Differentiation with respect to x yields

$$-\frac{2}{\pi}\int_0^\infty \lambda^2 K_1(\lambda)\sin\lambda x\,d\lambda = -3x(1+x^2)^{-5/2}$$

$$= -6(1+x^2)^{-1}\mathcal{J}_3\left(\frac{x}{\sqrt{1+x^2}}\right).$$

The last two equations verify (A.6) for n=2 and n=3, respectively. We next differentiate (A.6) and utilizing the relationships between Legendre and Gegenbauer functions:

$$-\frac{2}{\pi}\int_0^\infty \lambda^n K_1(\lambda)\sin[\lambda x-(n-2)\tfrac{\pi}{2}]d\lambda$$

$$= -n!(1+x^2)^{-n/2}\left[(n-1)\frac{x}{\sqrt{1+x^2}}\mathcal{J}_n\left(\frac{x}{\sqrt{1+x^2}}\right)+\left(1-\frac{x^2}{1+x^2}\right)P_{n-1}\left(\frac{x}{\sqrt{1+x^2}}\right)\right]$$

$$= -(n+1)!(1+x^2)^{-n/2}\mathcal{J}_{n+1}\left(\frac{x}{\sqrt{1+x^2}}\right).$$

Since $\sin[\lambda x-(n-2)\pi/2] = \cos[\lambda x-(n-1)\pi/2]$, this completes our inductive proof of (A.6).

What follows in deriving the desired integrals centers on equations (A.5) and (A.6) and involves their manipulation and re-indexing. It can be shown that

$$(1+x^2)^{-(n-3)/2}\mathcal{J}_n\left(\frac{x}{\sqrt{1+x^2}}\right)$$

$$= \frac{2n-3}{n(n-1)}(1+x^2)^{-(n-1)/2}P_{n-2}\left(\frac{x}{\sqrt{1+x^2}}\right)$$

$$+\frac{(n-2)(n-3)}{n(n-1)}(1+x^2)^{-(n-3)/2}\mathcal{J}_{n-2}\left(\frac{x}{\sqrt{1+x^2}}\right),$$

and

$$(1+x^2)^{-(n-1)/2}P_n\left(\frac{x}{\sqrt{1+x^2}}\right)$$

$$= (1+x^2)^{-(n-1)/2}P_{n-2}\left(\frac{x}{\sqrt{1+x^2}}\right)-(2n-1)\mathcal{J}_n\left(\frac{x}{\sqrt{1+x^2}}\right).$$

Substituting for the right hand sides of the latter two equations from (A.5) and (A.6) and combining integrals, we get

$$\frac{2}{\pi}\int_o^\infty \lambda^{n-3}[(2n-3)\lambda K_o(\lambda)-(n-2)(n-3)K_1(\lambda)]\cos[\lambda x-(n-2)\tfrac{\pi}{2}]d\lambda$$

$$= n!(1+x^2)^{-(n-3)/2}\mathcal{I}_n\left(\frac{x}{\sqrt{1+x^2}}\right), \quad n \geq 2 \tag{A.7}$$

and

$$\frac{2}{\pi}\int_o^\infty \lambda^{n-2}[n(n-1)K_o(\lambda)-(2n-1)\lambda K_1(\lambda)]\cos[\lambda x-(n-2)\tfrac{\pi}{2}]d\lambda$$

$$= n!(1+x^2)^{-(n-1)/2}P_n\left(\frac{x}{\sqrt{1+x^2}}\right), \quad n \geq 2, \tag{A.8}$$

The four equations (A.5) to (A.8) all have the following general form:

$$\frac{2}{\pi}\int_o^\infty g_n^{(k)}(\lambda)\cos[\lambda x-(n-2)\tfrac{\pi}{2}]d\lambda = n!f_n^{(k)}(x), \quad \begin{matrix} n \geq 2 \\ k = 1,2,3,4, \end{matrix} \tag{A.9}$$

where k = 1,2,3,4 for equations (A.5,8,6,7), respectively, and $f_n(-x) = (-1)^n f_n(x)$; i.e., $f_n(x)$ is even in x when n is even, and odd for odd n. It is further noted that

$$\cos[\lambda x-(n-2)\tfrac{\pi}{2}] = \begin{cases} -(-1)^{n/2}\cos\lambda x, & n = \text{even} \\ -(-1)^{(n-1)/2}\sin\lambda x, & n = \text{odd}. \end{cases} \tag{A.10}$$

When (A.10) is used to replace the cosine term in (A.9), the result is a Fourier cosine (sine) integral representation of the even (odd) function $n!f_n^{(k)}(x)$ when n is even (odd). We can, therefore, solve for the Fourier coefficient:

$$\int_o^\infty f_n^{(k)}(x)\begin{Bmatrix}\cos\lambda x\\ \sin\lambda x\end{Bmatrix} dx = \begin{Bmatrix}-(-1)^{n/2}\\ -(-1)^{(n-1)/2}\end{Bmatrix} \frac{1}{n!} g_n^{(k)}(\lambda), \qquad \begin{Bmatrix}n = \text{even}\\ n = \text{odd}\end{Bmatrix}, \quad n \geq 2, \quad k = 1,2,3,4 . \tag{A.11}$$

The derivation of the required integrals is now completed by comparing (A.9) to equations (A.5) to (A.8), extracting the eight functions $f_n^{(k)}(x)$ and $g_n^{(k)}(\lambda)$. A glance at (A.2) reveals that

$$f_n^{(1)}(x) = -F_n^{(1)}(x)$$

$$f_n^{(2)}(x) = F_n^{(2)}(x) - 2F_n^{(3)}(x)$$

$$f_n^{(3)}(x) = F_n^{(3)}(x)$$

$$f_n^{(4)}(x) = F_n^{(4)}(x).$$

Therefore, substitution for $f_n^{(k)}(x)$ and $g_n^{(k)}(\lambda)$ in (A.11) and multiplying by

$$(-1)^n \frac{2}{\pi}\begin{Bmatrix}\cos\lambda jd\\ \sin\lambda jd\end{Bmatrix}, \quad \begin{Bmatrix}n = \text{even}\\ n = \text{odd}\end{Bmatrix}$$

yields the functions $G_{nj}^{(k)}(\lambda)$ of equation (A.1):

$$G_{nj}^{(1)}(\lambda) = \begin{Bmatrix} (-1)^{n/2}\cos\lambda jd \\ -(-1)^{(n-1)/2}\sin\lambda jd \end{Bmatrix} \frac{2}{\pi n!}\lambda^{n}K_{o}(\lambda)$$

$$G_{nj}^{(2)}(\lambda) = \begin{Bmatrix} -(-1)^{n/2}\cos\lambda jd \\ (-1)^{(n-1)/2}\sin\lambda jd \end{Bmatrix} \frac{2}{\pi n!}\lambda^{n-2}[n(n-1)K_{o}(\lambda) - (2n-3)\lambda K_{1}(\lambda)]$$

$$G_{nj}^{(3)}(\lambda) = \begin{Bmatrix} -(-1)^{n/2}\cos\lambda jd \\ (-1)^{(n-1)/2}\sin\lambda jd \end{Bmatrix} \frac{2}{\pi n!}\lambda^{n-1}K_{1}(\lambda)$$

$$G_{nj}^{(4)}(\lambda) = \begin{Bmatrix} -(-1)^{n/2}\cos\lambda jd \\ (-1)^{(n-1)/2}\sin\lambda jd \end{Bmatrix} \frac{2}{\pi n!}\lambda^{n-3}[(2n-3)\lambda K_{o}(\lambda) - (n-2)(n-3)K_{1}(\lambda)].$$

These results are reproduced in section 3, equations (3.36) and (3.37).

References

Abramowitz, M. and Stegun, I. 1965 "Handbook of Mathematical Functions", Dover Publications, Inc.

Bart, E. 1959 M.Ch.E. Thesis, New York University.

Bohlin, T. 1960 Trans. Roy. Inst. Technol. (Stockholm), No. 155.

Brenner, H. 1970 J. Fluid Mech. 43, 641.

Brenner, H. 1971 Ind. Eng. Chem. Fundam. 10, 537.

Bungay, P.M. and Brenner, H. 1973 J. Fluid Mech. 60, 81.

Burgers, J.M. 1938 Second Report on Viscosity and Plasticity, North Holland Publishing Co., Amsterdam.

Burgers, J.M. 1940 Proc. Konigl. Akad. Wetenschap. (Amsterdam) 43, 425, 646.

Burgers, J.M. 1941 Proc. Konigl. Wetenschap. (Amsterdam) 44, 1045.

Burgers, J.M. 1942 Proc. Konigl. Akad. Wetenschap. (Amsterdam) 45, 9.

Chen, T.C. and Skalak, R. 1970 Appl. Sci. Res. 22, 403.

Faxen, H. 1922 Ann. Phys. 68, 89.

Faxen, H. 1923 Arkiv. Mat. Astron. Fys. 17, No. 27.

Gluckman, M.J., Pfeffer, R. and Weinbaum, S. 1971 J. Fluid Mech. 50, 705.

Gluckman, M.J., Weinbaum, S. and Pfeffer, R. 1972 J. Fluid Mech. 55, 677.

Goldman, A.J., Cox, R.G. and Brenner, H. 1967 Chem. Eng. Sci. 22, 653.

Greenstein, T. and Happel, J. 1970 Appl. Sci. Res. 22, 345.

Haberman, W.L. and Sayre, R.M. 1958 David W. Taylor Model Basin Report No. 1143, U.S. Navy Dept., Washington, D.C.

Happel, J. and Brenner, H. 1965 "Low Reynolds Number Hydrodynamics", Prentice Hall, Inc.

Happel, J. and Byrne, B.J. 1954 Ind. Eng. Chem. 46, 1181; corrections 1957 Ind. Eng. Chem. 49, 1029.

Happel, J. and Pfeffer, R. 1960 A.I.Ch.E. J. 6, 129.

Hochmuth, R.M. and Sutera, S.P. 1970 Chem. Eng. Sci. 25, 593.

Hocking, L.M. 1964 J. Fluid Mech. 20, 129.

Kynch, G.J. 1959 J. Fluid Mech. 5, 193.

Ladenburg, R. 1907 Ann. Phys. 23, 447.

Leichtberg, S., Gluckman, M.J., Weinbaum, S. and Pfeffer, R. 1975 "A Study of Unsteady Forces at Low Reynolds Number: A Strong Interaction Theory for the Coaxial Settling of Three or More Spheres", to be published.

Leichtberg, S., Weinbaum, S. and Pfeffer, R. 1975 "A Theory for the Coaxial Slow Viscous Motion of Finite Clusters of Spheres in Unbounded Poiseuille Flow and Its Application to Rouleaux Formation", to be published.

Payne, L.E. and Pell, W.H. 1960 J. Fluid Mech. 7, 529.

Sampson, R.A. 1891 Phil. Trans. Roy. Soc. A182, 449.

Savic, P. 1953 Nat. Res. Counc. Canada Rep. No. MT-22.

Skalak, R., Chen, P.H. and Chien, S. 1972 Biorheology 9, 67.

Smoluchowski, M. 1911 Bull. Int. Acad. Polonaise Sci. Lett. 1A, 28.

Smoluckowski, M. 1912 Proc. Fifth Int. Cong. Math. 2, 192.

Stimson, M. and Jeffery, O.B. 1926 Proc. Roy. Soc. A111, 110.

Wakiya, S. 1953 J. Phys. Soc. Japan 8, 254.

Wang, H. and Skalak, R. 1969 J. Fluid Mech. 38, 75.

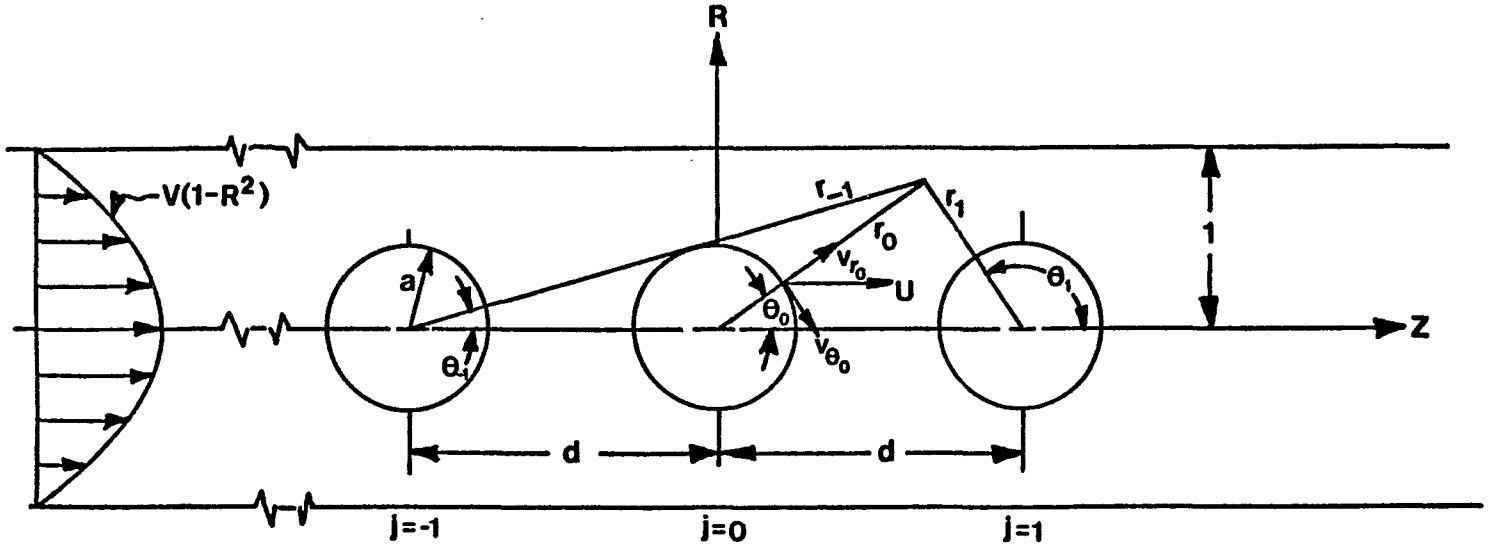

Figure 1. The system geometry.

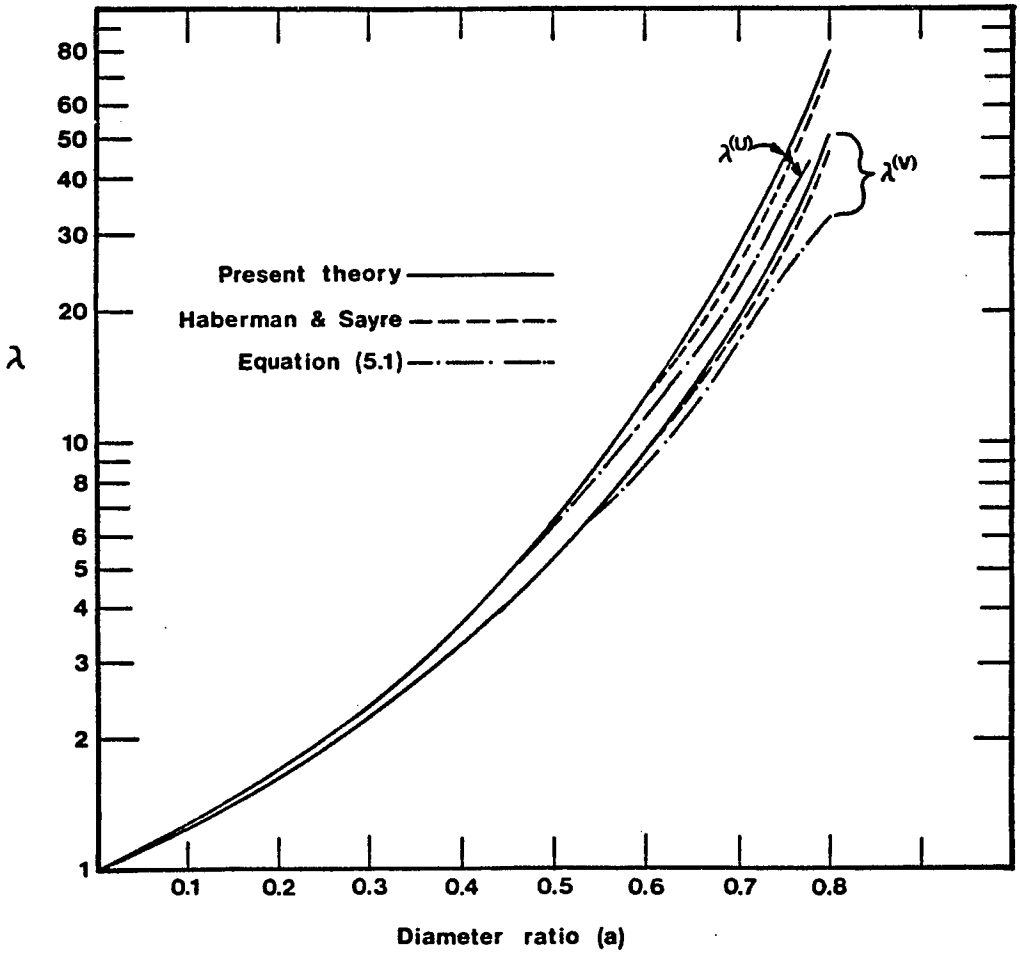

Figure 2. Comparison of single-sphere drag solution to results of Haberman & Sayre.

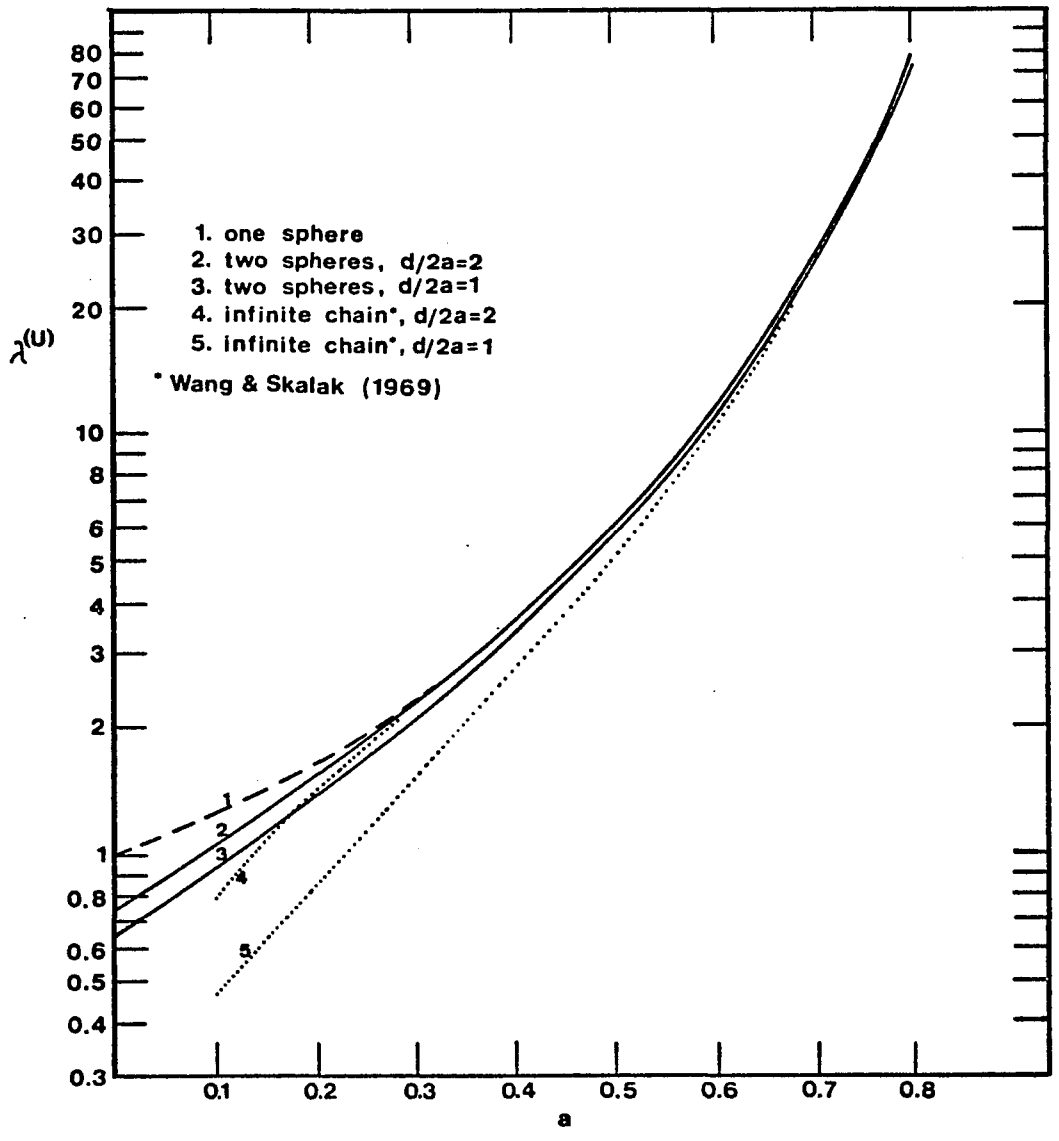

Figure 3. Drag correction factor $\lambda^{(U)}$ vs. diameter ratio.

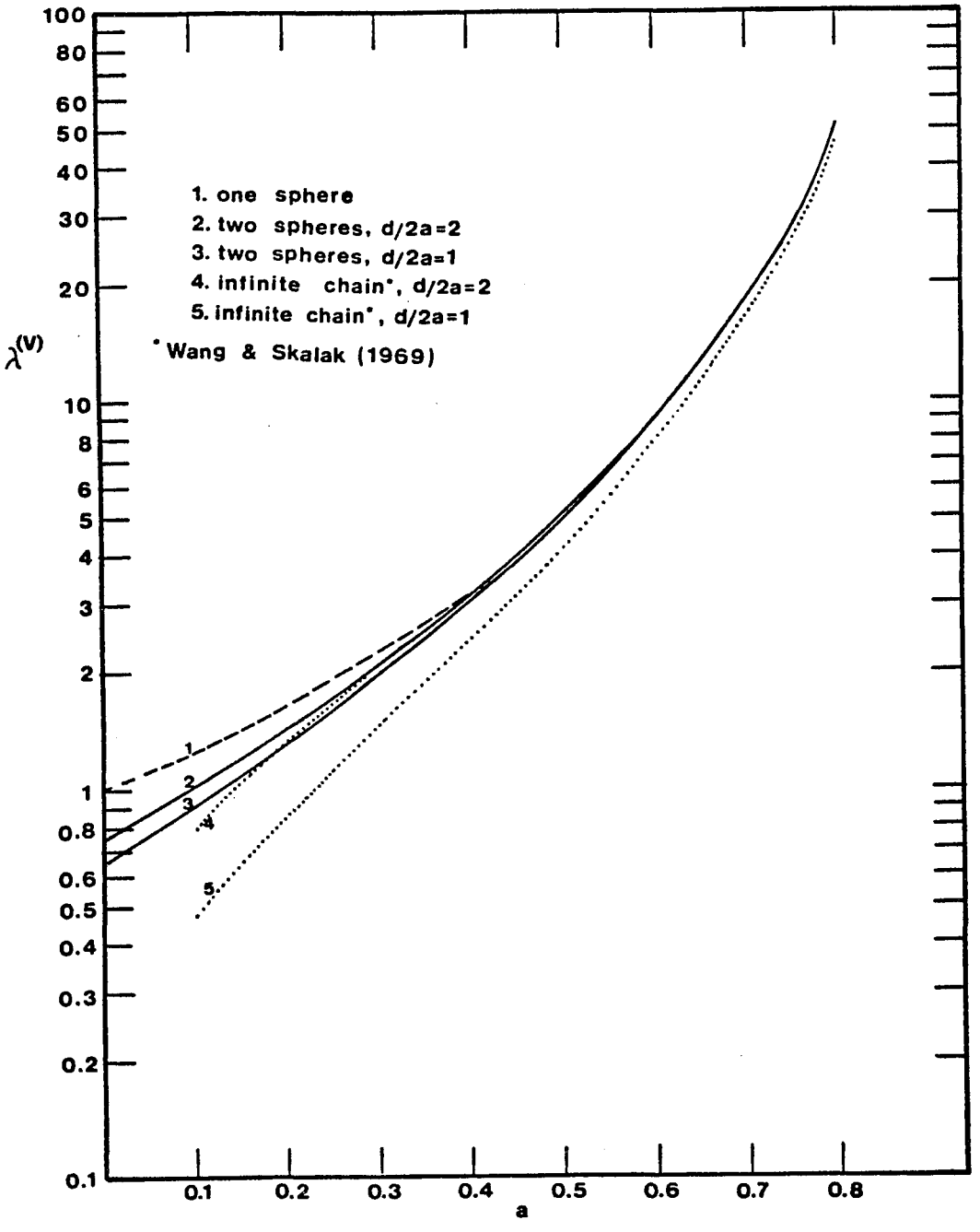

Figure 4. Drag correction factor $\lambda^{(V)}$ vs. diameter ratio.

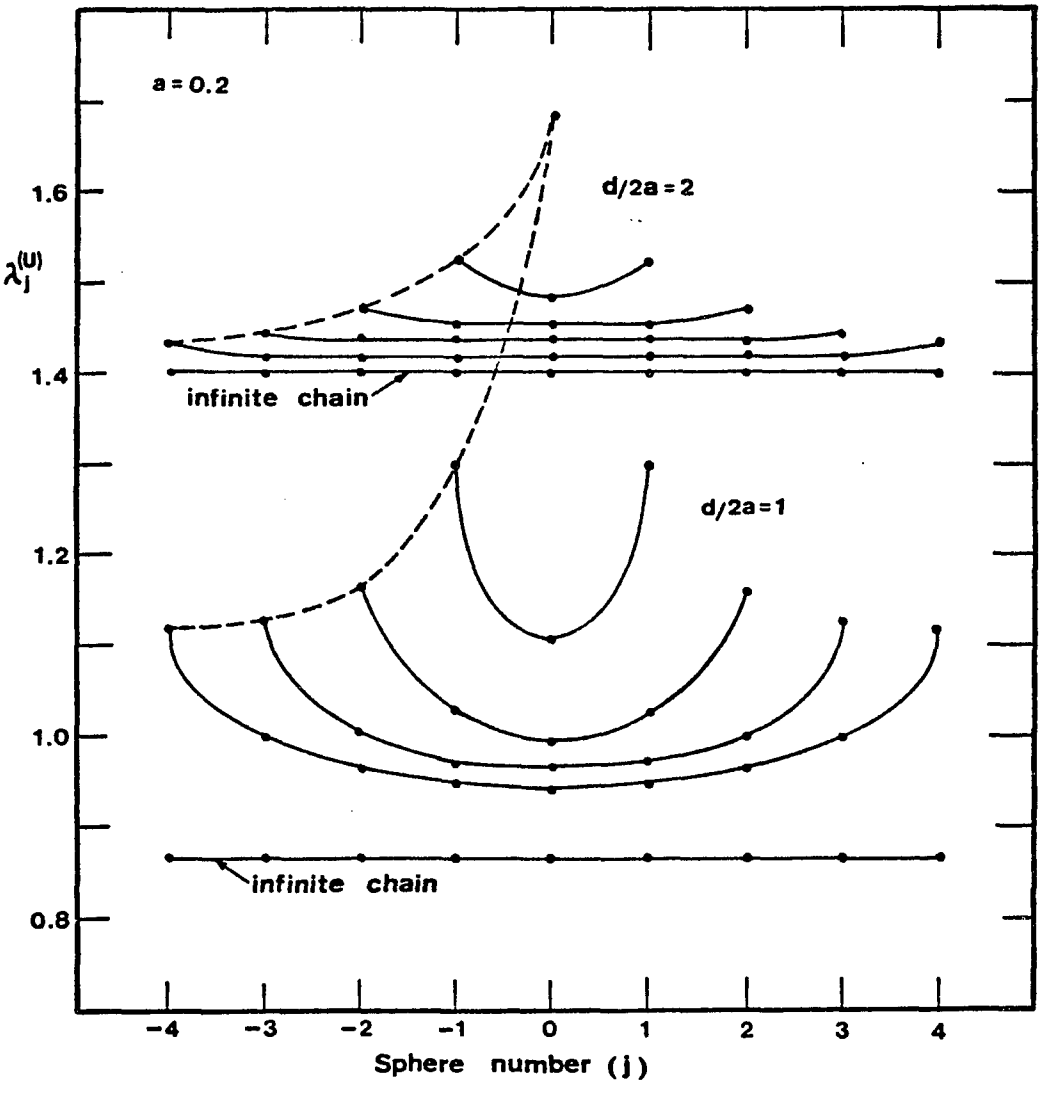

Figure 5. Drag correction factors $\lambda_j^{(U)}$ for chains containing various numbers of spheres of diameter ratio 0.2.

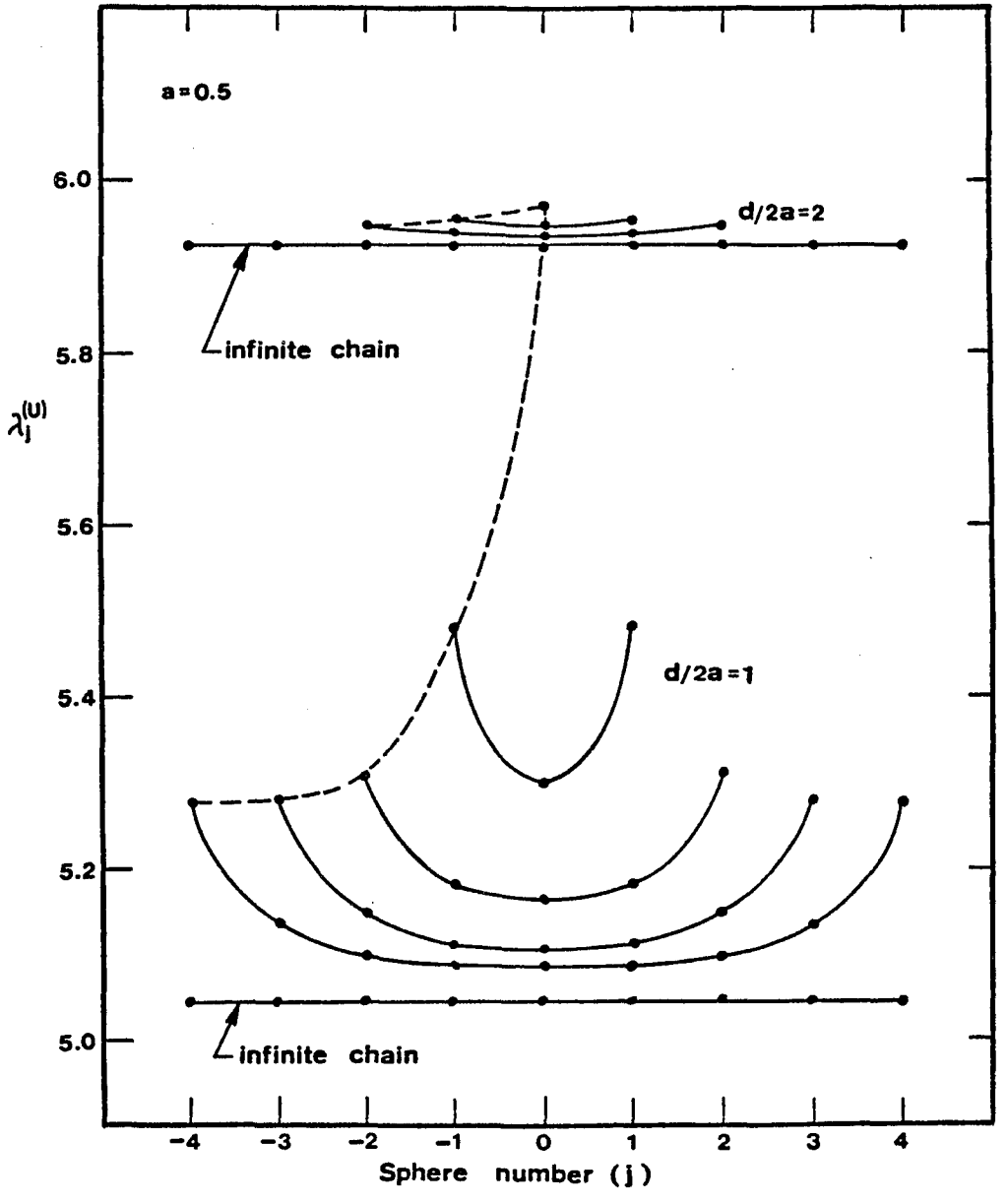

Figure 6. Drag correction factors $\lambda_j^{(U)}$ for chains containing various numbers of spheres of diameter ratio 0.5.

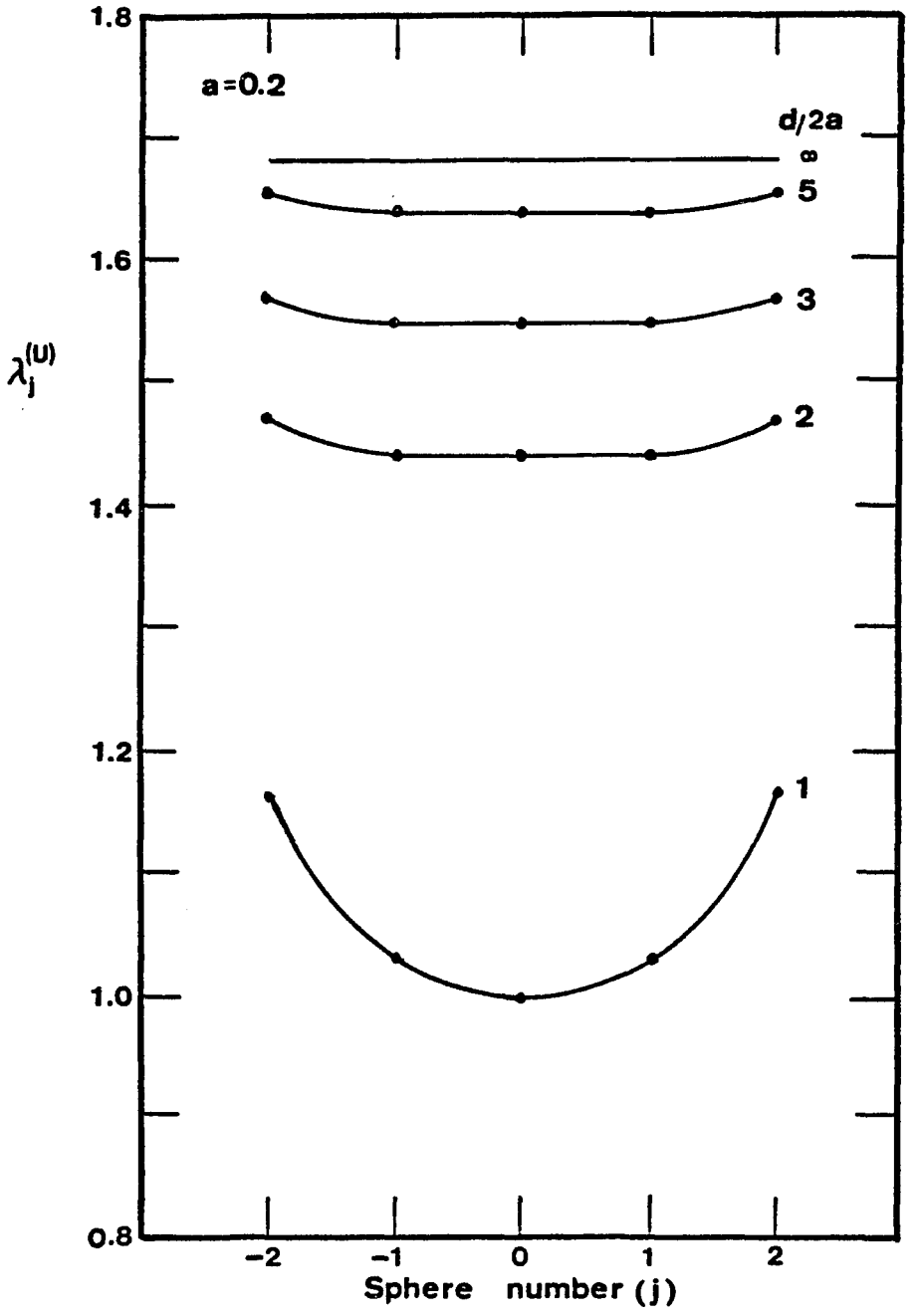

Figure 7. Drag correction factors $\lambda_j^{(U)}$ for five-sphere chains of diameter ratio 0.2 at different sphere spacings.

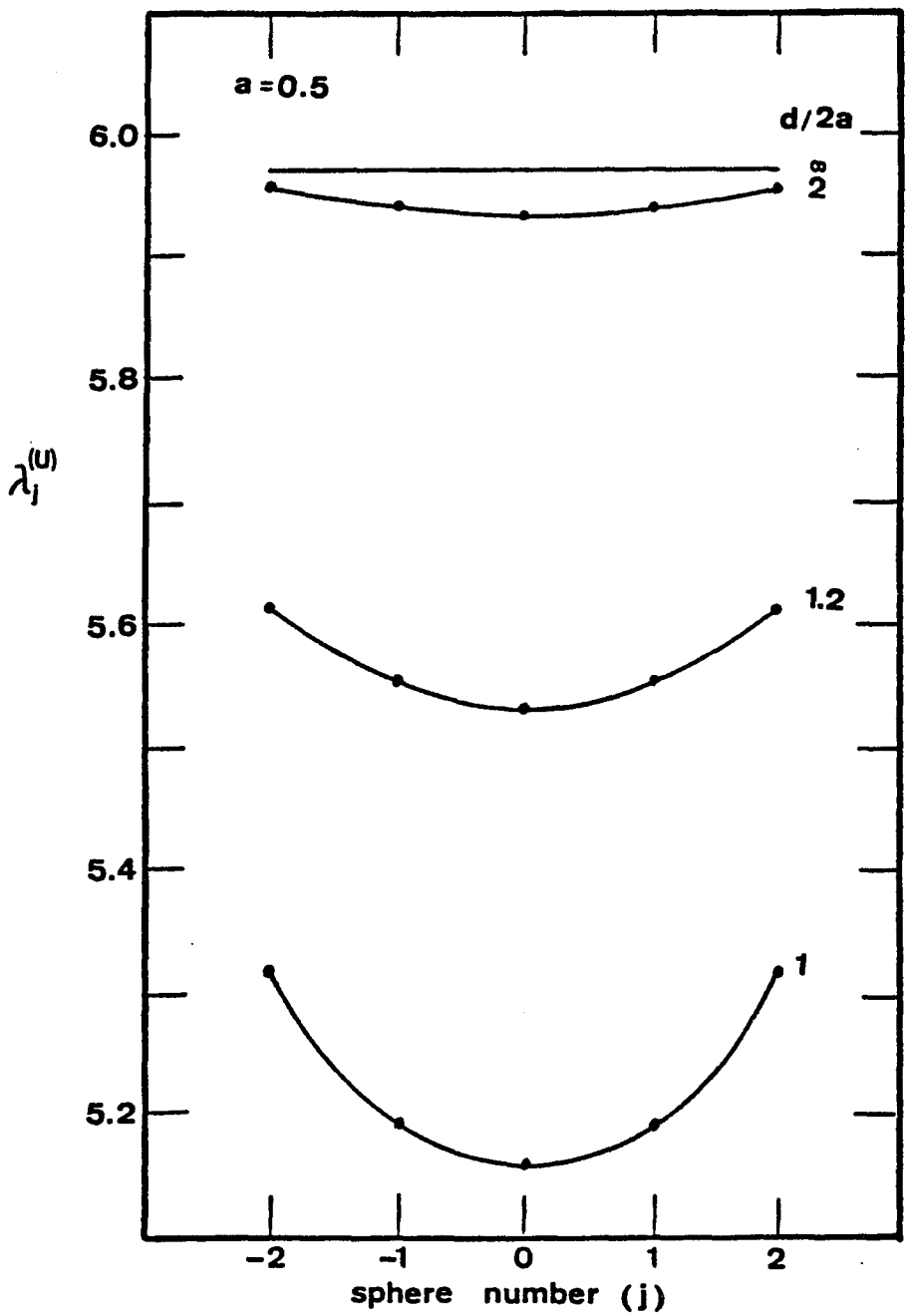

Figure 8. Drag correction factors $\lambda_j^{(U)}$ for five-sphere chains of diameter ratio 0.5 at different sphere spacings.

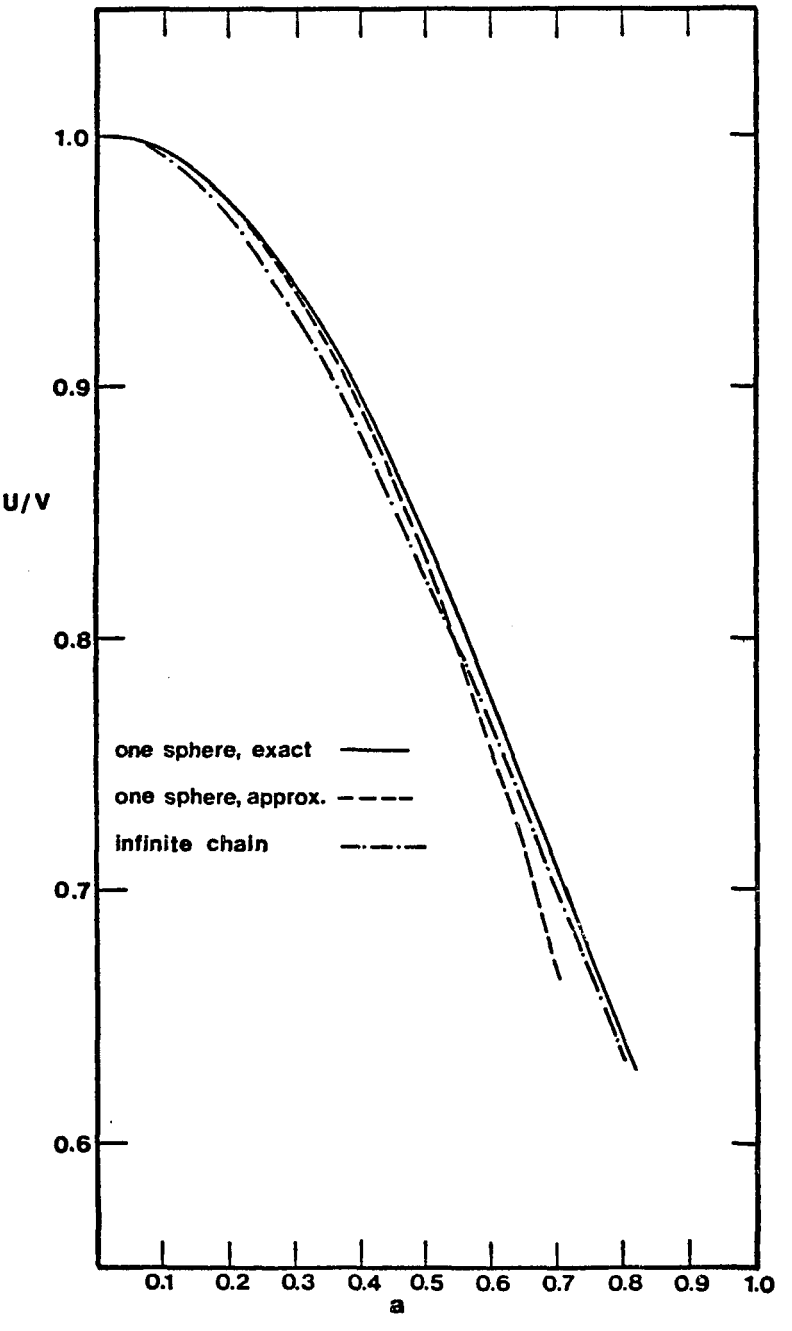

Figure 9. Zero-drag velocity vs. diameter ratio for one sphere, exact and approximate. Also shown are Wang & Skalak (1969) solutions for an infinite chain of contiguous spheres.

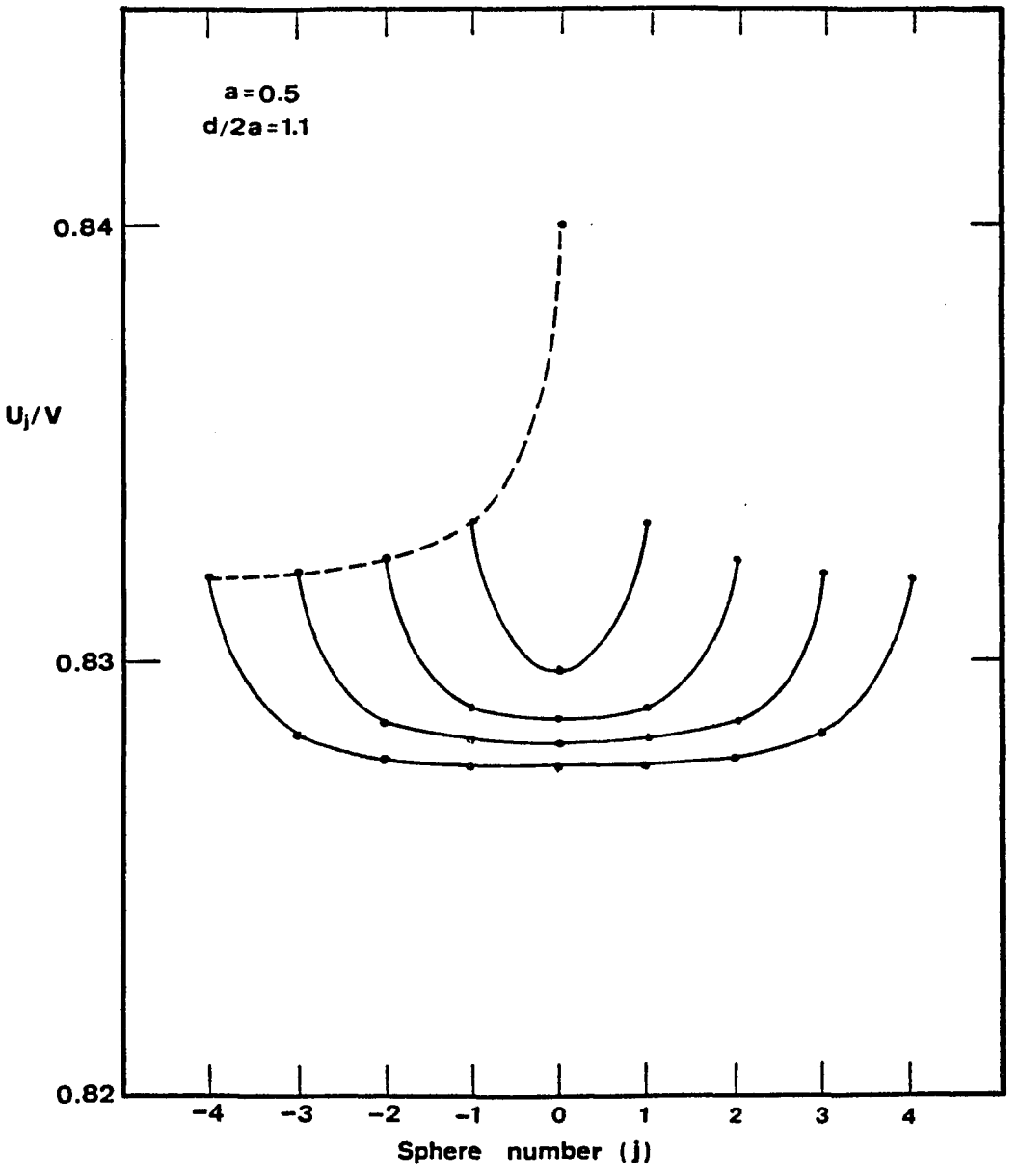

Figure 10. Zero-drag velocities in chains of diameter ratio 0.5, d/2a = 1.1, and varying length.

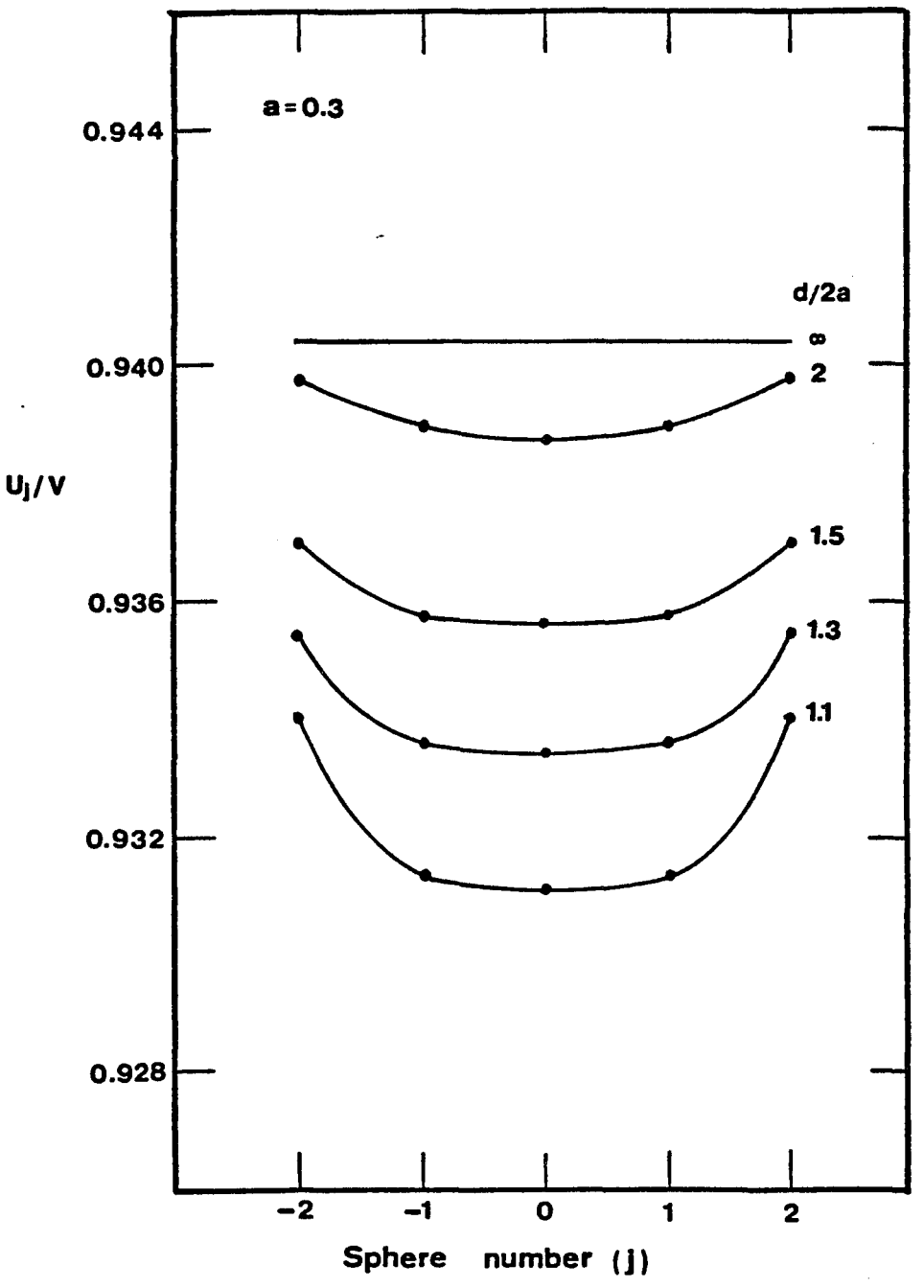

Figure 11. Zero-drag velocities in five-sphere chains of diameter ratio 0.3 and varying sphere spacings.

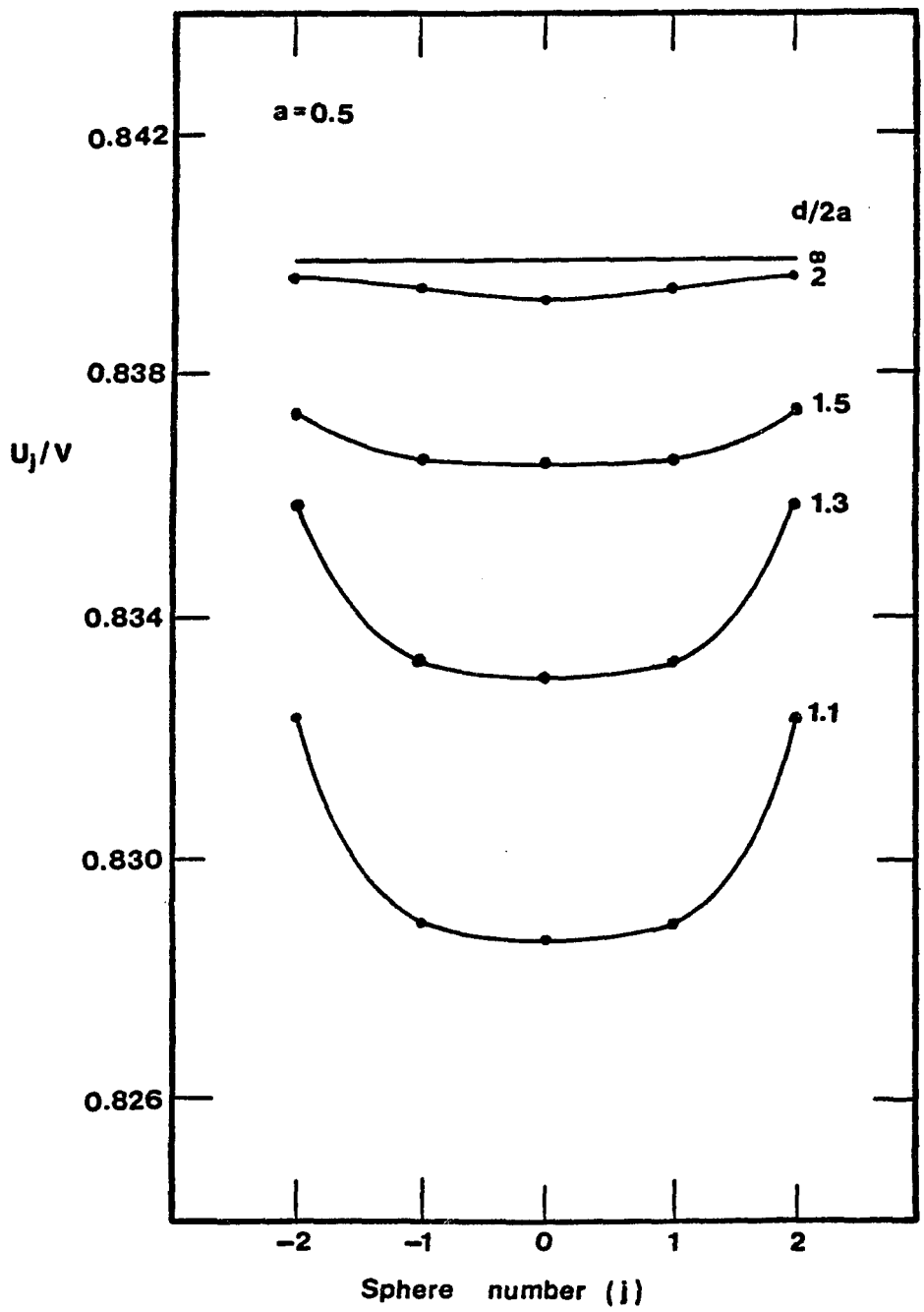

Figure 12. Zero-drag velocities in five-sphere chains of diameter ratio 0.5 and varying sphere spacings.

CHAPTER IV

A THEORY FOR THE COAXIAL SLOW VISCOUS MOTION OF FINITE CLUSTERS OF SPHERES IN UNBOUNDED POISEUILLE FLOW AND ITS APPLICATTON TO ROULEAUX FORMATION

Abstract

The tendency of red cells to stack axially and form aggregates, or rouleaux, in their passage through the microcirculation is a well documented phenomenon. The mechanism for the formation of rouleaux is commonly attributed to London-Van der Waals attraction forces and to intercellular bridging by macromolecular monolayers. While these short range forces and other assumed mechanisms are unquestionably important for red cells that are almost touching, they do not explain the mechanism by which the red cells achieve their nearly touching configuration.

The paper describes a simplified theoretical model for the time-dependent behavior of a closely spaced, neutrally-buoyant chain of identical red cells in Poiseuille flow. The results of this model predict a new hydrodynamical mechanism for the formation of rouleaux in the microcirculation, which suggests that the long range forces responsible for the red cell aggregation may be hydrodynamic in origin and due to multi-particle Stokes flow interaction effects. Toward that end, the interaction theory developed by the authors for gravity-driven Stokes flow is extended to the time-dependent, axisymmetric motion of finite chains of neutrally-buoyant spheres in unbounded Poiseuille flow at low Re. This theory predicts that individual particles in a finite chain of identical cells travel at different velocities due to particle interactions and that these effects are most pronounced for 16-80μ arterioles and venules.

1. INTRODUCTION

The tendency of red cells to stack axially and form aggregates, or rouleaux, in their passage through the microcapillaries is a well documented phenomenon. Krough (1922), in examining the blood flow at the base of the nail, reports that it is possible "to see gaps in a stream moving at a fairly rapid rate", and notes some observations which "would be expected if they are just gaps in the moving column of corpuscles, but not if they are contractions pushing the corpuscles before them...". These first crude observations have since been vastly refined in in vivo, in vitro, and laboratory models of the microcirculation. Monro's (1963) in vivo study of the microcapillary blood flow in the rabbit ear chamber presents photographs and sketches of chains of moving red cells separated by zones of relatively cell free plasma. Monro reports that the average chain length is in the vicinity of 8 cells in 11μ vessels, and 15 cells in 12μ vessels. Whitmore (1968) gives numerous references to previous studies of red cell aggregation and presents a thorough discussion of the aggregative properties of blood and other suspensions. An excellent summary of the rheological properties of red cell suspensions in arterioles (greater than 60-80μ) somewhat larger than those considered herein is given in Meiselman and Goldsmith (1973).

The study of rouleaux formation may carry more than just academic interest. Whitmore (1968) points out that the first visual evidence of rheological abnormality which is usually observed in the circulation, other than changes in the red cells' character, is a more conspicuous aggregation of the cellular material. This is a possible signal of the activation of the fibrinogen-fibrin reaction which generally occurs after

injury to, or interference with, the system. Two mechanisms, which are thought to be associated with red cell aggregation under abnormal conditions, are discussed in Whitmore (1968). One is the development of adhesive substances on the surfaces of the red cells. These sticky protein precipitates create a severe form of aggregation or "sludging" of the blood, which occurs most frequently in infection after cells have passed through inflamed vessels, and possibly in trauma or allergy. A second aggregating mechanism, which is particularly important under stagnant flow conditions, is the bridging or direct coupling between adjacent red cell surfaces by a macromolecular monolayer of certain long-chain molecules such as fibrinogen, some globulins and high molecular weight dextrans.

The above bridging phenomenon has been studied in three recent investigations by Chien and Jan, who measured the degree of aggregation of red blood cells in dextran solutions under various conditions. In Chien and Jan (1973), these investigators report that increasing the molecular weight of the dextran fractions makes them increasingly more effective in causing rouleaux formation, due to the two-fold effect of (i) larger adsorption area on the cell surface resulting in a stronger bridging force and (ii) weaker electrical repulsion due to longer intercellular distances. The electrical force is due to the red blood cells' negative surface charge, resulting primarily from the presence of ionogenic carboxyl groups of sialic acids on the wall surface. The role of this surface electric charge in red blood cell interactions was studied by Jan and Chien (1973a,b). By varying the surface charge of the cells, the ionic composition of the fluid medium, and the molecular weight and concentration of the dextran solution, the investigators determined that the

surface charge of red blood cells plays a significant role in cell-to-cell interactions by inhibiting their aggregation, and that the electrostatic repulsive force is operative over a distance of more than 200Å.

It is evident, therefore, that the rate of aggregation due to macromolecular bridging and the stability of such rouleaux depends on a balance of the adsorption force between the macromolecule and cell surfaces vs. the electrostatic repulsion force, the mechanical shear force, and the membrane bending force. While these short-range forces are unquestionably important for red cells that are almost touching at spacings of the order of 10^3 angstroms or less, they fail to explain why the red cells should achieve this almost touching configuration in the first place. Whitmore (1966 and 1967) is the only previous investigator to have addressed this latter question. Whitmore suggests that a possible mechanism is the size variation between red and white cells and red cells themselves in any given blood sample. Since in a narrow vessel small cells travel slightly faster than larger ones, it is conceivable that a train of particles would regroup into smaller stacks, each headed by a large cell or an embolus and tailed by smaller ones, with cell-free plasma preceding the rouleaux. The axial stacks of cells

frequently observed behind a white cell are strong evidence in support of this hypothesis when widely different cell sizes are involved.

The marshalling of aggregating red cells into neat axial stacks requires that the red cells readjust their relative positions after coming into contact. In this manner the red cells are able to achieve positions of minimum energy (presenting the minimum free surface to the plasma) and maximum mechanical stability which, for discoids, is the rouleau shape. Brenner and Bungay (1971) note that the additional pressure drop required to sustain flow in a tube containing an eccentrically located rigid sphere depends upon the third power of the sphere-to-cylinder diameter ratio, while that for a concentrically located one depends on the fifth power. Consequently, the former configuration will always give rise to larger pressure drops than the latter, especially at large eccentricities.

It has been suggested by Fahraeus (1958) that the queuing of random aggregates into rouleaux might aid blood flow by drawing the cells into a core, thus increasing the width of the plasma layer in which most of the shear occurs. This argument is consistent with the observed tendency of rouleaux to stay at or near the tube centerline. Red cells exhibit an axial drift, or migration across streamlines, away from the tube wall (Goldsmith, 1971). This migration toward a position of lower velocity gradient was studied theoretically by Wohl and Rubinow (1974). They show that it arises out of the interaction between the incident flow and the particle deformation, even at Reynolds numbers which are too small for tubular pinch effects (Segré and Silberberg, 1962) to occur.

From the standpoint of energy conservation, there is good reason for the red cells not to travel separately in the small arterioles and veins 15μ and larger. The recent investigation by Skalak et al. (1972) has shown that at fixed hematocrit the formation of rouleaux of identical red cells results in a lower apparent viscosity of the blood, and hence a decreased energy dissipation. Skalak et al. also show that slightly irregular rouleaux, such as would be caused by random sizing of red cells, result in nearly the same apparent viscosity as uniform rouleaux. This behavior suggests that the slowly decaying hydrodynamic forces between unequally spaced identical red cells might be more important in rouleaux formation than the small hydrodynamic force differences due to the statistical variation in red cell dimensions. This basic hypothesis is borne out by the results of the present study.

Existing theoretical and experimental studies of the microcirculation have focused primarily on the red cells' interaction with the capillary wall, or on the deformation of the red cell due to the stresses induced by its interaction with the boundary or by the fluid motion. Much less attention has been devoted to the interparticle interaction between the cells, the subject of the present study.

The physical properties of the red cell membrane and capillary wall are quite complicated. The recent investigations by Skalak et al. (1973), Zarda (1974), and Chien et al. (1975) have provided enough information about the elastic and visco-elastic properties of the red cell membrane to permit fairly accurate quantitative predictions of the hydrodynamic and elastic behavior of the red cells as they are transported by plasma through the microcapillaries. The theoretical and experimental

models investigated to date have been largely limited to the rigid-particle and liquid-droplet models, with the aim of bracketing the possible extreme range of variation in properties. In their survey paper, Brenner and Bungay (1971) provide an informative summary of the many significant theoretical facts that have emerged from experimental and mathematical investigations of these two extreme models.

Considerable research has been conducted on the liquid droplet model in an attempt to simulate the deformation of the red cell under hemodynamic stress: Goldsmith and Mason (1962), Chaffey et al. (1965), Cox (1969), Hetsroni et al. (1970) and Hyman and Skalak (1969). The paper by Hyman and Skalak analyzes the motion of an infinite train of identical, equally-spaced, neutrally buoyant, spherical liquid droplets moving axially in a long tube. The limiting rigid-sphere case of infinite particle viscosity had been studied earlier by Wang and Skalak (1969). In these infinite-train studies, all particles translate with the same velocity because of the model's inherent peroidicity. As a result, the calculations reveal only relatively weak interparticle hydrodynamic interactions compared with the particle-wall effects.

The problem of the interaction between a single rigid or linear-elastic particle and a cylindrical boundary has also received extensive attention. Haberman and Sayre (1958) present an exact solution for a single rigid sphere moving concentrically in a long tube. The Haberman and Sayre solution technique failed to converge in the limit as the sphere to cylinder diameter ratio approached unity but this problem was later handled by Hochmuth and Sutera (1970) using lubrication-theory analysis. In the latter work, the authors found that the

additional pressure drop required to move the sphere approached infinity as the clearance between the sphere and the wall vanished. This singular behavior can be removed if the sphere is replaced by a liquid droplet of the same volume. The droplet is able to alleviate the large stresses in the narrow fluid gap by undergoing gross deformations in shape. Experimental studies by Skalak and Branemark (1969), Hochmuth et al. (1970), and Goldsmith and Marlow (1972), of erythrocytes flowing in narrow capillaries have similarly observed appreciable deformations in shape. The latter problem has also been studied theoretically by Lighthill (1968) and Fitz-Gerald (1969a,b) using a linear pressure-deformation model of the red cell membrane. Some other representative studies of the red cell-wall interaction problem include Darabaner and Mason (1967), Goldman et al. (1967), Sutera and Hochmuth (1968), Hochmuth and Sutera (1969 and 1970), Chen and Skalak (1970), and Brenner (1970). Thorough discussions of the various aspects of microcirculatory mechanics are presented in two recent survey papers, Skalak (1972) and Goldsmith and Skalak (1975).

The present study differs from existing theoretical models in that it emphasizes the interparticle interactions which exist between red cells in 10-80μ vessels. To this end a strong interaction theory is presented for the transient behavior of finite axial chains of rigid, neutrally-buoyant spheres in unbounded Poiseuille flows. The principal difficulty in treating this unsteady interaction problem has historically been the treatment of the quasi-steady Stokes flows for three or more closely spaced particles. The basic techniques for handling these quasi-steady flows for both unbounded and bounded axisymmetric systems are described in three recent papers by the

authors, Gluckman, Pfeffer, and Weinbaum (1971) and Leichtberg et al. (1975a,b). These studies show that the rouleaux-forming hydrodynamic mechanism exists in both bounded and unbounded flows. Our aim here is not the exact solution of red blood cell motion, but rather a qualitative description of the rouleaux-forming mechanism, based on the exact solutions of other, related flow problems.

A discussion of hydrodynamic interparticle interaction effects in unbounded and bounded media follows in section 2. Section 3 defines the present problem and some of its simplifying assumptions. Section 4 presents an outline of the theory, while section 5 discusses the results.

2. THE EFFECTS OF INTER-PARTICLE INTERACTIONS

The chief characteristic of the hydrodynamic rouleaux-forming mechanism proposed in this paper is the long-range interaction which takes place between the various bodies of a multi-body Stokes flow. The essential features of this interaction for coaxial bounded and unbounded flows are reported in several recent papers by the authors: Gluckman, Pfeffer and Weinbaum (1971), Leichtberg, Gluckman, Weinbaum and Pfeffer (1975), and Leichtberg, Pfeffer and Weinbaum (1975).

In Gluckman, Pfeffer, and Weinbaum (1971), attention is focused on the slow, viscous, axisymmetric flow past a finite chain of spheres or spheroids in an unbounded medium. The particles are identical and are translating in an otherwise quiescent fluid. When only one sphere is present in the chain, that sphere is isolated and experiences a resisting drag force of

$$F = 6\pi\mu U a \tag{2.1}$$

where μ = fluid viscosity,
U = sphere velocity,
a = sphere radius.

In longer chains of, say, N spheres the drag experienced by each sphere is found to depend on the positions and velocities of all the other spheres in the chain. We define, for convenience, the drag correction factor λ_j (j=1,2,...,N) for each of the N spheres as follows:

$$F_j = 6\pi\mu U_j a\lambda_j \ , \ j=1,2,\ldots,N \tag{2.2}$$

where U_j is the velocity of the j^{th} sphere in the chain. The

drag correction factor is, therefore, the ratio of the drag on a sphere in an array to the drag on an identical isolated sphere.

The drag correction factors λ_j are shown in Figure 1 for a seven-sphere chain in which the spheres are equally spaced and moving with equal velocities. In a neutrally-buoyant or gravity-driven flow the velocities of the spheres would, of course, not be equal. Although λ_j has a discrete value for each object, the values have been connected by solid lines to indicate each individual chain.

The figure demonstrates several characteristics of the inter-sphere interaction. The curve at $d/a = \infty$ represents an isolated sphere with $\lambda = 1$. Spheres in coaxial chains with finite spacings all have $\lambda_j < 1$. This drag reduction is due to the transmission of a velocity disturbance created by each sphere to the boundaries of all the other spheres (Hocking, 1964). Of greater import to the present study is the apparent shielding effect, evidenced by the dependence of the drag reduction on a sphere's position within a chain and on the spacing. It can be seen that in any one chain the central spheres receive a greater shielding and, hence, experience a lower drag than the outer ones. Also noted is the decreasing drag as the sphere spacing decreases, due to the increased particle interaction. Also, as the spheres move further apart, the end effects are seen to decrease.

The shielding, or inter-particle interaction, effect is thus unequally distributed among the various spheres of a chain and is a strong function of the inter-sphere spacing. If the chain were sedimenting freely along its line of centers, the settling velocity of each sphere would be inversely proportional

to its drag (in the absence of inertia). The unequal interactions would then impart greater settling velocities to central spheres and lower velocities to outer ones. The equal-spacing, equal-velocities configuration is thus unstable and cannot persist. In fact, a chain of three or more spheres has no stable steady state configuration since the quasi-steady Stokes drag on each sphere continues to vary because of multiparticle interaction effects that continually change as a function of particle spacing and velocity.

The qualitative behavior of a sedimenting three-sphere chain in a gravitational field has been investigated experimentally by Happel and Pfeffer (1960). This time-dependent problem was also solved theoretically in Leichtberg, Gluckman, Weinbaum and Pfeffer (1975) for chains of three to twenty-five spheres. Figure 2 presents a velocity-time plot of the three-sphere time-dependent problem along with schematic drawings of the configurations at various times. The velocity of each sphere has been nondimensionalized by U_t, the single sphere terminal settling velocity, and time by a/U_t. Spheres 1 and 2 are initially almost touching, and sphere 3 is relatively isolated ten diameters away. However, at this configuration spheres 1 and 2 interact strongly as a doublet, settling with equal velocities 40% greater than that of sphere 1. As the doublet approaches the single sphere, sphere 3 begins to accelerate due to the reduction in its drag created by the approaching doublet. The doublet also accelerates somewhat because of its interaction with sphere 3, but sphere 2, which receives more of this interaction than does sphere 1, accelerates faster than the latter. Due to the doublet's break-up, sphere 1 decelerates. Thus, spheres 2 and 3 approach each other and form a doublet which

rapidly moves away from the increasingly isolated sphere 1, whose velocity asymptotes to $U_1/U_t = 1$.

Although the three-sphere system described above has no steady state configuration, the doublet of spheres 2 and 3 does asymptotically approach a steady state. Thus, the multiparticle interaction effects have served to create a stable, steady doublet, or a rouleaux of two spheres in this gravity driven system. Spheres 2 and 3 cannot collide in a finite time under hydrodynamic forces alone, because of the large stresses set up in the narrowing gap. The spheres can only asymptote toward collision. In the case of red blood cells this is of no consequence, since at close spacings the short-range force balance discussed in section 1 becomes the dominant interaction between the cells.

The behavior of longer chains was also reported in Leichtberg, Gluckman, Weinbaum and Pfeffer (1975), strongly suggesting that chains of non-touching spheres will tend to break up into groups of contiguous particles. The trailing third of a long chain of spheres will disintegrate into a series of single, isolated spheres. The leading half to two-thirds of the chain will break up into a series of doublets and triplets, which would then recombine to form a series of shorter, unsteady chains.

The bounded flow problem for a finite chain of spheres translating axially inside a long circular-cylindrical tube has been examined in Leichtberg, Pfeffer and Weinberg (1975). The quasi-steady state drag forces were found to be affected by the same shielding effects exhibited in Figure 1, with two important exceptions. The effect of the bounding wall is to greatly increase the drag forces (approaching infinity as the sphere-wall

clearance vanishes; see Hochmuth and Sutera, 1970), while exerting a damping influence on the end effects of the sphere-sphere interactions. The damping effect of the tube wall is appreciable only at sphere to cylinder diameter ratios of 0.5 and greater, for center-to-center sphere spacings of about two diameters or more.

When particles move freely along the centerline of a tube in which a fluid is flowing with a Poiseuille velocity profile, each particle translates at its own zero-drag velocity. This is the velocity at which the particle must be carried along by the through flow and have the net fluid resistance on the body vanish, assuming negligible inertial forces.

Figures 3 and 4 present the quasi-steady state zero-drag velocities for a chain of five equally-spaced spheres, at sphere-to-cylinder diameter ratios of 0.3 and 0.5, respectively. Here the sphere velocities are normalized by V_o, the centerline velocity of the parabolic profile, or twice its mean velocity. As in Figure 1, these two figures illustrate the inter-particle interaction effects. However, unlike the settling of spheres in a quiescent fluid, the effect of the inter-particle interactions is to decrease rather than increase the sphere velocities, due to the transmission of the centerline velocity defect of each sphere to the boundaries of all the other spheres. Hence, the central sphere, the one most shielded from high momentum fluid, moves most slowly. Outer spheres, on the other hand, move with the greatest velocities, once more demonstrating the importance of end effects. One also observes that as the sphere spacing increases the sphere velocities gradually approach a maximum velocity, namely that for an isolated sphere in a cylinder with the same sphere-to-cylinder diameter ratio.

A comparison of Figures 3 and 4 reveals the wall damping mentioned before. It is seen that the end effects, which are still quite pronounced for d/2a = 2 at the 0.3 diameter ratio case shown in Figure 3 are significantly damped for the 0.5 diameter ratio case shown in Figure 4 for chains whose center-to-center sphere spacing exceeds 2 sphere diameters.

In order to bracket the range of diameter ratios in which the particle interactions are dominant, Figure 5 plots the zero-drag sphere velocities in a five-sphere chain, normalized by the end sphere's velocity, against the diameter ratio. For the d/2a = 2 case, it is seen that the interaction-induced relative velocity is greatest at $a/R_o \approx 0.25$. The degree of wall damping is observed to rapidly grow in severity as the sphere-to-cylinder diameter ratio increases beyond 0.5. This wall damping is the dominant interaction in capillaries less than roughly 16μ. For very closely spaced chains, however, such as the d/2a = 1.3 case shown in Figure 5, the particle interaction effects are seen to be significant for somewhat larger diameter ratios.

Spheres whose diameters are less than 0.1 cylinder diameters, on the other hand, are found to interact very little with each other in zero-drag motion. Due to the vanishing fluid shear near the centerline, the spheres are being carried with velocity V_o by a fluid with an essentially uniform velocity, V_o. Without the sphere-induced fluid velocity defect, the spheres cannot interact. We see, then, that the rouleaux-forming inter-particle interactions are important only in tubes whose diameter is roughly between two and ten sphere diameters. These interactions are damped by the sphere-wall interaction in smaller tubes, and are insignificant in zero-drag motion in the larger tubes.

3. A SIMPLIFIED BOUNDED FLOW MODEL

In the previous section we considered the effect of chain length, sphere spacing and sphere-to-cylinder diameter ratio on the instantaneous steady state interactions which take place in finite coaxial clusters of spheres which are moving in both bounded and unbounded media. In addition, we examined the time-dependent behavior of such arrays settling along their line of centers in an infinite medium. Both the quasi-steady and the transient behavior for these related problems strongly suggest that inter-particle interactions provide a plausible mechanism for the formation of rouleaux. To conclusively demonstrate this hypothesis one needs to examine the time-dependent zero-drag motion of finite coaxial clusters of identical particles flowing in a tube.

Unfortunately, an exact time-dependent analysis of multi-particle motions in a bounded medium is prohibitively time-consuming on present generation computers, though theoretically possible using the methods of Leichtberg, Gluckman, Weinbaum and Pfeffer (1975). Therefore, an exact verification of the expected transient behavior of bounded flow is not presently practical.

A greatly simplified approximate model, however, is suggested by the exact quasi-steady solutions for the relative importance of the two interaction modes which govern the zero-drag multi-sphere motion inside the cylindrical tube. The inter-sphere interaction, which originates in the non-uniform fluid Poiseuille velocity profile in the vicinity of the spheres, is seen to be the basic mechanism which imparts the unequal velocities to the spheres. This effect was observed to give rise to appreciable end effects for sphere-to-cylinder diameter

ratios greater than 0.1. The wall-sphere interaction, on the other hand, simply serves as a damping effect on the former interaction, controlling its magnitude but not its qualitative aspects. The presence of the no-slip boundary condition introduced by the wall was noted to be particularly important for sphere-to-cylinder diameter ratios greater than 0.5. Hence, a fictitious flow problem can be invented, in which the parabolic fluid velocity profile exists in space with the spheres moving along its center, but with the solid cylinder wall not present. The numerical errors introduced by this approximation will be carefully examined later in connection with Figure 9.

In view of the previous discussion, this simplification has a two-fold effect. First, it retains the Poiseuille flow, the driving mechanism behind the inter-sphere velocity differences. Second, the simplification eliminates the need to satisfy the no-slip boundary conditions on the tube wall, a process of counter-balancing the disturbances on the tube wall created by the spheres' presence. This latter process is a time-consuming operation which accounts for more than 99 percent of the computational time in a quasi-steady state calculation. Its elimination makes it possible to consider time-dependent cases without biasing the transient behavior which we wish to examine.

This simplification does, consequently, lead to numerical inaccuracies but does not change the qualitative predictions of the theory.

4. THEORY

Consider a chain of N spheres moving along the centerline of an unbounded Poiseuille flow, whose undisturbed fluid velocity is

$$V(R) = V_o(1 - R^2/R_o^2), \tag{4.1}$$

The geometry of the N-sphere chain is shown in Figure 6.

The Stokes flow is governed by the fourth-order, linear, partial differential equation

$$E^2(E^2\psi) = 0, \tag{4.2}$$

where the operator E^2 in spherical coordinates is

$$E^2 = \frac{\partial^2}{\partial r^2} + \frac{\sin^2\theta}{r^2}\frac{\partial^2}{\partial(\cos\theta)^2}, \tag{4.3}$$

and ψ is the axisymmetric stream function. The general solution to (4.2), which satisfies the conditions of boundedness on the centerline and vanishing disturbances at infinity, is given by Haberman and Sayre (1958), Gluckman, Pfeffer and Weinbaum (1971), and Leichtberg, Pfeffer and Weinbaum (1975):

$$\psi = V_o R_o^2[\tfrac{1}{2}(R/R_o)^2 - \tfrac{1}{4}(R/R_o)^4] + \sum_{j=1}^{N}\sum_{n=2}^{\infty}[B_{nj}r_j^{-n+1} + D_{nj}r_j^{-n+3}]\mathcal{J}_n(\cos\theta_j). \tag{4.4}$$

The $\mathcal{J}_n(\cos\theta_j)$ are the Gegenbauer functions of the first kind, R, r_j, and θ_j are coordinates defined in Figure 6, and B_{nj} and D_{nj} are arbitrary constants. Each inner term of the infinite series in (4.4) is a fundamental solution to (4.2) and is

singular at $r_j = 0$. The entire series solution is a linear superposition of N singular infinite-series representations of the disturbance produced by each of the N spheres.

No-slip boundary conditions on the sphere surfaces,

$$\left.\begin{aligned} \frac{1}{R}\frac{\partial \psi}{\partial R} &= U_j \\ \frac{1}{R}\frac{\partial \psi}{\partial z} &= 0 \end{aligned}\right\} \text{ on } r_j = a \ , \ j = 1,2,\ldots,N, \qquad (4.5)$$

need be applied only on the semicircular generating arc of each sphere, due to the axial symmetry. To satisfy the boundary conditions (4.5) exactly along the entire generating arc of each sphere would require the solution of the entire infinite array of unknown coefficients. We, therefore, employ the truncation technique developed in Gluckman, Pfeffer and Weinbaum (1971), satisfying the boundary conditions only at a finite number of discrete points on each sphere's generating arc, and truncating the infinite series of (4.4) accordingly.

If the generating arc is approximated by satisfying conditions (4.5) at M discrete points, the infinite series is truncated after n = M+1. This retains M inner terms, each containing two unknown coefficients which permit one to satisfy the two exact no-slip boundary conditions at one point on each sphere. The result is a linear set of 2xMxN simultaneous algebraic equations for the 2xMxN B_{nj} and D_{nj} unknown coefficients of the truncated solution. This matrix equation can be solved to yield the unknown constants by any standard matrix reduction technique, if the sphere velocities are known.

In this problem, however, the sphere velocities U_j, $j = 1,2,\ldots,N$, are not known. The number of unknowns, therefore, exceeds the number of equations by N. This condition will be corrected by introducing the spheres' dynamic equations of motion.

A typical pair of equations for the unknown B_{nj} and D_{nj} constants, obtained by applying conditions (4.5) at the m'th point of sphere i having the spatial coordinates (R_{mi}, z_{mi}), has the general form

$$\sum_{j=1}^{N} \sum_{n=2}^{M+1} [B'_{nj;mi} B_{nj} + D'_{nj;mi} D_{nj}] = U_i - V_o(1-R^2_{mi}/R^2_o)$$

$$\sum_{j=1}^{N} \sum_{n=2}^{M+1} [B''_{nj;mi} B_{nj} + D''_{nj;mi} D_{nj}] = 0, \qquad (4.6)$$

where $B'_{nj;mi}$, $D'_{nj;mi}$, $B''_{nj;mi}$, $D''_{nj;mi}$ are known functions of the coordinates R_{mi} and z_{mi}. This pair of equations is one of NxM such pairs, $(m = 1,2,\ldots,M;\ i = 1,2,\ldots,N)$.

The dynamic equation of motion for the spheres is given in Leichtberg, Gluckman, Weinbaum and Pfeffer (1975). The full equation balances the hydrodynamic drag and buoyancy forces against the "unsteady" inertial, virtual-mass and Basset forces which relate to particle acceleration. The subsequent time-dependent analysis of the gravity-driven settling chain of spheres shows that the most important "unsteady" force term in the transient motion is the Basset force. The magnitude of this force is proportional to the half power of the Reynolds number. However, the inter-particle interactions in the present problem of spheres being convected in a non-uniform velocity profile are roughly two orders of magnitude smaller than those for the gravity-driven motion. Consequently the "unsteady" forces are expected to be negligibly small. With the spheres assumed to be

sufficiently neutrally-buoyant, the force balance requires the spheres to travel along the centerline with velocities U_j ($j = 1,2,\ldots,N$) such that the viscous drag force on each sphere is nearly zero, i.e.,

$$F_j = 0 \ , \ j = 1,2,\ldots,N. \tag{4.7}$$

The viscous drag force on each sphere j is (Haberman and Sayre 1958)

$$F_j = 4\pi\mu D_{2j} \tag{4.8}$$

i.e., only the first order term (n=2) of the inner series of (4.4) contributes to the drag forces exerted on each submerged sphere. The dynamic balance of forces on the spheres is achieved, then, by setting

$$D_{2j} = 0 \ , \ j = 1,2,\ldots,N. \tag{4.9}$$

thus eliminating N unknowns from the matrix equation.

With (4.9), equations (4.6) become

$$\sum_{j=1}^{N} [B'_{2j;mi} B_{2j} - \delta_{ij} U_j) + \sum_{n=3}^{M+1} (B'_{nj;mi} B_{nj} + D'_{nj;mi} D_{nj})] = -V_o (1 - R'^2_{mi}/R_o^2)$$

$$\sum_{j=1}^{N} [B''_{2j;mi} B_{2j} + \sum_{n=3}^{M+1} (B''_{nj;mi} B_{nj} + D''_{nj;mi} D_{nj})] = 0, \tag{4.10}$$

where δ_{ij} is the Kronecker delta. Equations (4.10), for all i ($i = 1,2,\ldots,N$) and m ($m = 1,2,\ldots,M$), constitute the linear set of algebraic equations for the unknowns D_{nj} ($n \neq 2$), B_{nj} and U_j.

The accuracy of the technique depends on M, the order of truncation, and can be improved to any degree by taking a sufficiently large value of M. The convergence as M increases is found to be very rapid. Quasi-steady, or instantaneous, values of the sphere velocities at any given configuration are obtained with excellent accuracy with only a small number of boundary points on each sphere. The truncation errors for the worst case of touching spheres are of the order of 3 percent when M=1 and 0.001 percent for M=5.

The chain configuration at any given time is calculated by integrating

$$\frac{dz_j}{dt} = U_j \quad , \; j = 1,2,\ldots,N \tag{4.11}$$

where $z_j(t)$ is the axial location of the center of sphere j. The time coordinate is discretized. For the (k+1)'th time interval, $t_k \le t \le t_{k+1} = t_k + \Delta t$, we expand $z_j(t_{k+1})$ about $t = t_k$:

$$z_j(t_{k+1}) = z_j(t_k) + \Delta t \frac{dz_j}{dt}(t_k) + \tfrac{1}{2}\Delta t^2 \frac{d^2 z_j}{dt^2}(t_k) + O(\Delta t^3) = \ldots$$

$$= z_j(t_k) + \tfrac{1}{2}\Delta t[U_j(t_k) + U_j(t_{k+1})] + \epsilon_{j,k} \tag{4.12}$$

where

$$\epsilon_{j,k} = -\frac{1}{12}\Delta t^3 \frac{d^2 U_j}{dt^2}(t_k) \tag{4.13}$$

is the discretion error estimate. The sphere positions $z_j(t_{k+1})$

and velocities $U_j(t_{k+1})$, $j = 1,2,\ldots,N$, are calculated by an iterative procedure which alternately solves for the spacings from equation (4.12) and for the velocities by the truncation technique, until convergence is reached. Converged solutions at each time interval are generally achieved rapidly, in one to three iterations. The time interval Δt is optimized after each step by estimating the error from (4.13). A complete transient calculation for the motion of a three-sphere chain typically requires up to 4000 velocity calculations and roughly seven minutes of IBM 370/168 computer time.

5. RESULTS

The quasi-steady state zero-drag sphere velocities were calculated for a variety of chain lengths and configurations using the simplified parabolic profile model described by equations (4.4) and (4.10). In Figure 7 are shown the normalized sphere velocities, U_j/V_o, for various chains containing one to eleven equally spaced spheres. All the chains have a diameter ratio of $a/R_o = 0.5$. The solid lines connect the discrete values of each sphere to indicate individual chains. As the figure shows, the inter-particle interaction effects observed in Figures 1, 3, and 4 are also present in the simplified model. The central sphere of each chain has the lowest velocity, with the velocity increasing rapidly as the ends of the chain are approached. As the chain length increases, the velocity of the central sphere decreases and the end effects become more pronounced.

The effect of spacing on the sphere velocities is demonstrated in Figure 8. Values of U_j/V_o are shown for chains of seven equally spaced spheres at various sphere spacings. As the sphere spacing decreases the sphere velocities decrease and end effects become more important. One concludes from a comparison of Figures 4 and 8 that an unbounded Poiseuille flow exhibits the same interaction and end effects observed in the exact solutions for bounded flow, Figure 4. The removal of the solid tube wall introduces a small numerical error, but does not change the qualitative predictions of the theory. The bounded-flow sphere velocities are slightly greater than the corresponding velocities in the unbounded Poiseuille flow.

A direct numerical comparison of the exact (Leichtberg, Pfeffer and Weinbaum 1975) and approximate (unbounded Poiseuille

flow) solutions for the zero-drag velocity on a single sphere at all diameter ratios is presented in Figure 9. Figure 9 indicates that the reflection from the tube wall of the disturbances produced by the motion of the spheres has a negligible effect on the sphere motion for $a/R_o < 0.2$ and that for $a/R_o = 0.5$ the error is about 0.5 percent. The neglect of the no-slip boundary condition at the cylinder surface is thus seen to be a reasonable approximation for the range of a/R_o where the rouleaux forming mechanism described herein is operative. This is due to the fact that the missing wall effect in the approximate solution is the secondary effect of the wall on the perturbed flow produced by the sphere, and not the primary effect of producing the Poiseuille flow in the absence of the sphere.

The time-dependent behavior of a typical coaxial three sphere chain is shown in Figure 10. Time is non-dimensionalized by a/V_o. Spheres 2 and 3 are initially nearly touching, with sphere 1 three sphere diameters away. The trend is for sphere 1 to approach and form an isolated doublet with sphere 2, while sphere 3 moves away with greater velocity. This behavior confirms our earlier hypothesis that hydrodynamic multi-particle interactions provide a rouleaux-forming mechanism in zero-drag motion. Qualitatively, the behavior is the inverse of that found in Figure 2 for a chain of three spheres settling in a quiescent fluid in a gravitational field. The other important difference is that the interaction effects in the zero-drag motion are roughly two orders of magnitude smaller than those exhibited in Figure 2. This confirms the assertion which was made in Section 4 in reference to the magnitude of the acceleration-related forces acting on the spheres.

Examination of Figures 5 and 10 shows that a rough estimate can be obtained for the distance that a typical chain travels before significant clustering occurs. We may consider, for example, chains of equally spaced spheres with center-to-center spacings of 1.3, 1.5 and 2 sphere diameters, corresponding to particle volume fractions of 13, 11 and 8 percent, respectively, when $a/R_o = 0.5$. Typical hematocrits in 16μ capillaries average around 25%, but this figure is based on the erythrocyte rather than sphere geometry. Our data indicates that the distance traveled by a chain is roughly 100, 240 and 1900 sphere diameters for the three initial spacings considered. However, when the interaction is between a nearly touching doublet and a single sphere which is 1.3, 1.5 and 2 diameters away, the distances traveled for significant interactions to occur are reduced by roughly 50%. According to these estimates, an 8μ red cell in a 16μ vessel must travel typically a distance of the order of 0.4-0.8 mm, 1-2 mm and 7-14 mm, respectively, for the multiparticle interaction effects described herein to be an important influence. The typical length of a single capillary is of the order 0.1 mm. Thus, the time-cumulative effect of the motion through several successive generations of capillaries is very likely involved in the hydrodynamic rouleaux forming mechanism discussed in this study.

6. CONCLUSIONS

The foregoing results provide convincing evidence that the hydrodynamical interactions between identical red cells can lead to the formation of rouleaux in the microcirculation. The theory also predicts that because of the wall damping and the interactive mechanism's dependence on the centerline curvature of the velocity profile, the proposed hydrodynamic mechanism is most important in vessels 16μ to 80μ. In smaller capillaries the interactive effects are effectively damped out by the capillary wall, whereas in larger arterioles and venules there is too little drift between the red cell and the local velocity profile for the inter-particle interactions to be significant.

Although inter-particle interactions are most significant in axial motion through the 16-80μ vessels, axial arrays are observed mostly in capillaries 15μ and smaller. Physiologically, axial stacks are less common in larger vessels, where the arrays are more random. Work on asymmetric configurations is now in progress and may shed further light in the future.

Once the red cells are closer than 0.1μ it is believed that short range attractive forces between adjacent red cells play an important if not dominant role. In the absence of short range forces, long chains of equally spaced particles are observed to regroup into clusters of contiguous particles. However, these clusters are also unstable and do not persist. On the other hand, if short range attraction forces are present, one would expect the stability of the resulting clusters to be greatly increased.

REFERENCES

Brenner, H. 1970 J. Fluid Mech. 43, 641.

Brenner, H. and Bungay, P.M. 1971 Federation Proceedings 30, 1565.

Chaffey, C.E., Brenner, H. and Mason, S.G. 1965 Rheol. Acta 4, 64. (Correction 1967 Rheol. Acta 6, 100).

Chen, T.C. and Skalak, R. 1970 Appl. Sci. Res. 22, 403.

Chien, S. and Jan, K.-M. 1973 Microvas. Res. 5, 155.

Chwang, A.T. and Wu, T.Y. 1974 J. Fluid Mech. 63, 607.

Cox, R.G. 1969 J. Fluid Mech. 37, 601.

Darabaner, C.L. and Mason, S.G. 1967 Rheol. Acta 6, 273.

Fahraeus, R. 1958 Acta med. scand. 161, 151.

Fitz-Gerald, J.M. 1969a Proc. Roy. Soc. Lond. B.174, 193.

Fitz-Gerald, J.M. 1969b J. Appl. Physiol. 27, 912.

Gluckman, M.J., Pfeffer, R., and Weinbaum, S. 1971 J. Fluid Mech. 50, 705.

Goldman, A.J., Cox, R.G. and Brenner, H. 1967 Chem. Eng. Sci. 22, 637.

Goldman, A.J., Cox, R.G. and Brenner, H. 1967 Chem. Eng. Sci. 22, 653.

Goldsmith, H.L. 1971 Fed. Proc. 30, 1578.

Goldsmith, H.L. and Marlow, J. 1972 Proc. Roy. Soc. Lond. B 182, 351.

Goldsmith, H.L. and Mason, S.G. 1962 J. Colloid Sci. 17, 448.

Goldsmith, H.L. and Skalak, R. 1975 Ann. Review of Fluid Mech., 213.

Haberman, W.L. and Sayre, R.M. 1958 David W. Taylor Model Basin Report No. 1143, U.S. Navy Dept., Washington, D.C.

Happel, J. and Pfeffer, R. 1960 A.I.Ch.E. Journal 6, 129.

Hetsroni, G., Haber, S. and Wacholder, E. 1970 J. Fluid Mech. 41, 689.

Hochmuth, R.M., Marple, R.N. and Sutera, S.P. 1970 Microvasc. Res. 2, 409.

Hochmuth, R.M. and Sutera, S.P. 1969 Bibliotheca Anat. 10, 113.

Hocking, L.M. 1964 J. Fluid Mech. 20, 129.

Hyman, W.A. and Skalak, R. 1969 Tech. Rept. no. 3, Project no. NR 062-393, Columbia University, Dept. of Civil Engineering and Engineering Mechanics.

Jan, K.-M. and Chien, S. 1973 J. Gen. Physiol. 61, 638.

Jan, K.-M. and Chien, S. 1973 J. Gen. Physiol. 61, 655.

Krough, A. 1922 "The Anatomy and Physiology of Capillaries," Yale University Press.

Leichtberg, S., Gluckman, M.J., Pfeffer, R. and Weinbaum, S. 1975 "A Study of Unsteady Forces at Low Reynolds Number: A Strong Interaction Theory for the Coaxial Settling of Three or More Spheres," to be published.

Leichtberg, S., Pfeffer, R., and Weinbaum, S. 1975 "Stokes Flow Past Finite Coaxial Clusters of Spheres in a Circular Cylinder," to be published.

Lighthill, M.J. 1968 J. Fluid Mech. 34, 113.

Meiselman, H.J. and Goldsmith, H.L. 1973 Thrombosis Diath. Hemorh. Supplement 44, 273.

Monro, P.A.G. 1963 Biorheology 1, 239.

Rosen, A.L. 1972 J. Inst. Maths. Applics 9, 265.

Segré, S. and Silberberg, A. 1962 J. Fluid Mech. 14, 115.

Skalak, R. 1972 "Biomechanics: Its Foundations and Objectives," ed. Y.-C., Fung, N. Perrone, and M. Anliker, Prentice Hall, Inc., pp. 457-499.

Skalak, R. and Branemark, P.I. 1969 Science 164, 717.

Skalak, R., Chen, P.H. and Chien, S. 1972 Biorheology 9, 67.

Sutera, S.P. and Hochmuth, R.M. 1968 Biorheology 5, 45.

Wang, H. and Skalak, R. 1969 J. Fluid Mech. 38, 75.

Whitmore, R.L. 1966 Nature 209, 298.

Whitmore, R.L. 1967 Appl. Physiol. 22, 767.

Whitmore, R.L. 1968 "Rheology of the Circulation," Pergamon Press.

Wohl, P.R. and Rubinow, S.I. 1974 J. Fluid Mech. 62, 185.

Chien, S., King, R.G., Skalak, R., Usami, S. and Copley, A.L. 1975 Biochemistry (in press).

Skalak, R., Zarda, P.R., Chen, P.H. and Chen, T.C. 1971 Symposium on Computer-Aided Engineering, U. of Waterloo, 403.

Zarda, P.R., Jr. 1974 Ph.D. Dissertation, Columbia University.

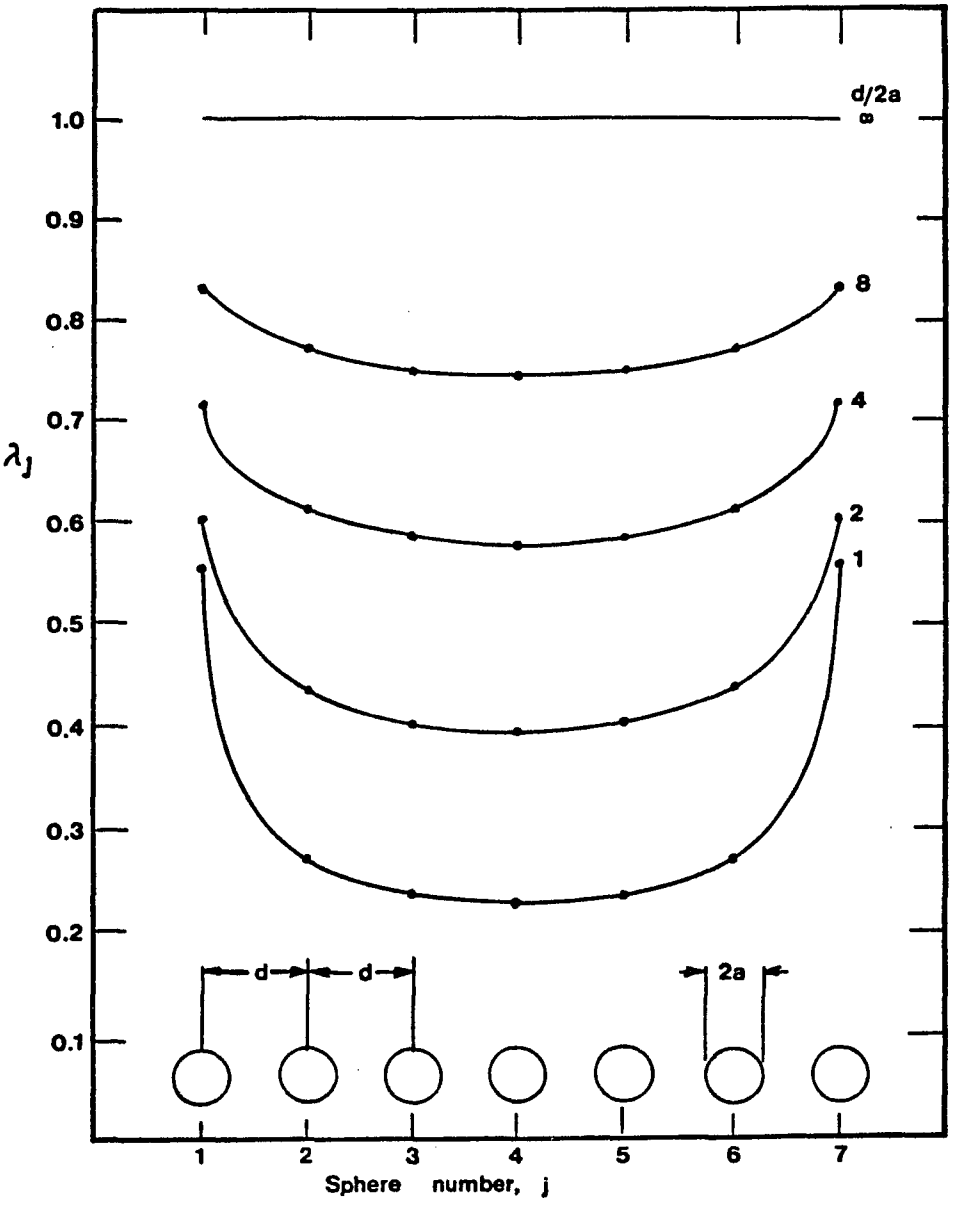

Figure 1. Quasi-steady state drag correction factors for an equally-spaced seven-sphere chain at various sphere spacings, in an infinite quiescent fluid (from Gluckman, Pfeffer & Weinbaum, 1971).

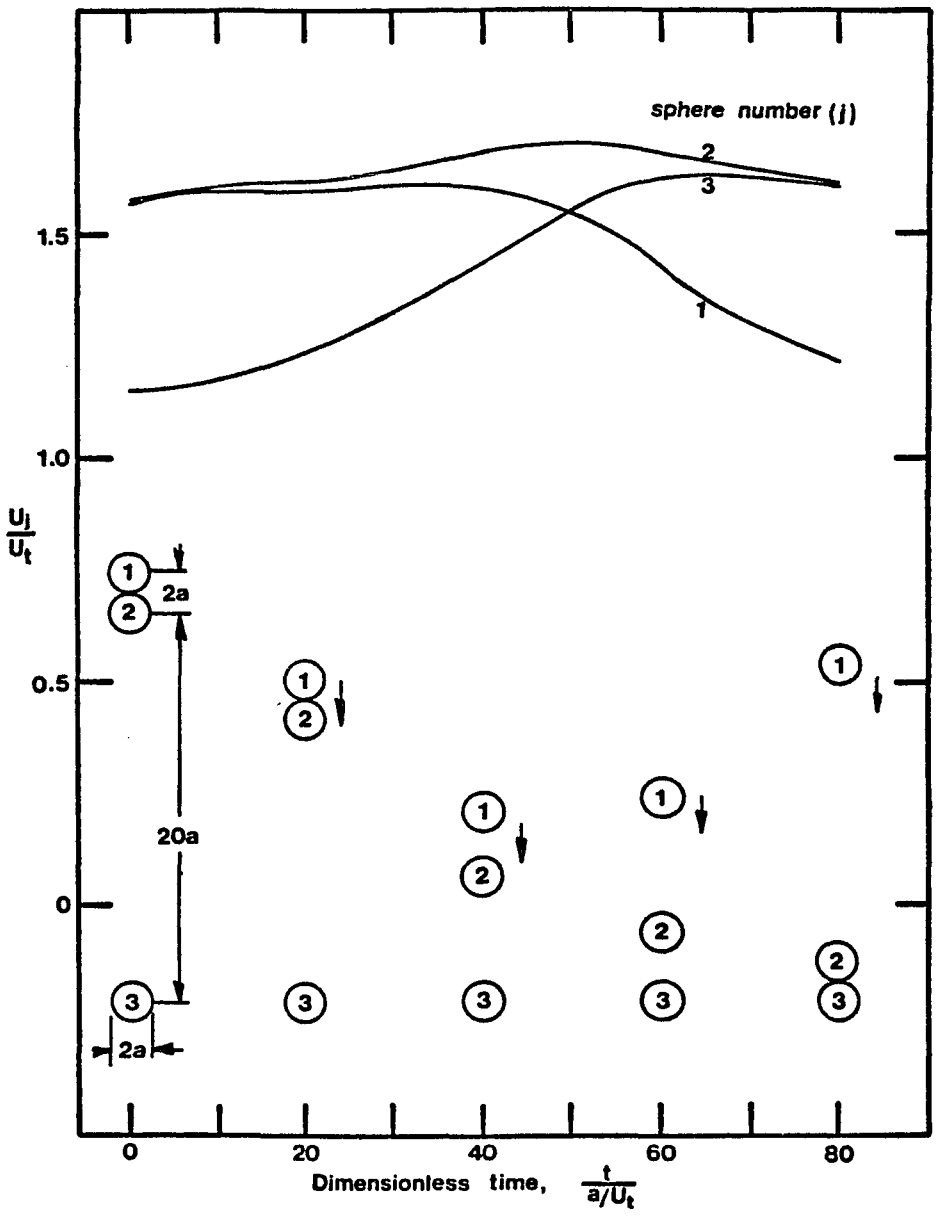

Figure 2. Velocities and configurations for a chain of three spheres falling along its line of centers in an infinite quiescent fluid (from Leichtberg, Gluckman, Weinbaum & Pfeffer, 1975).

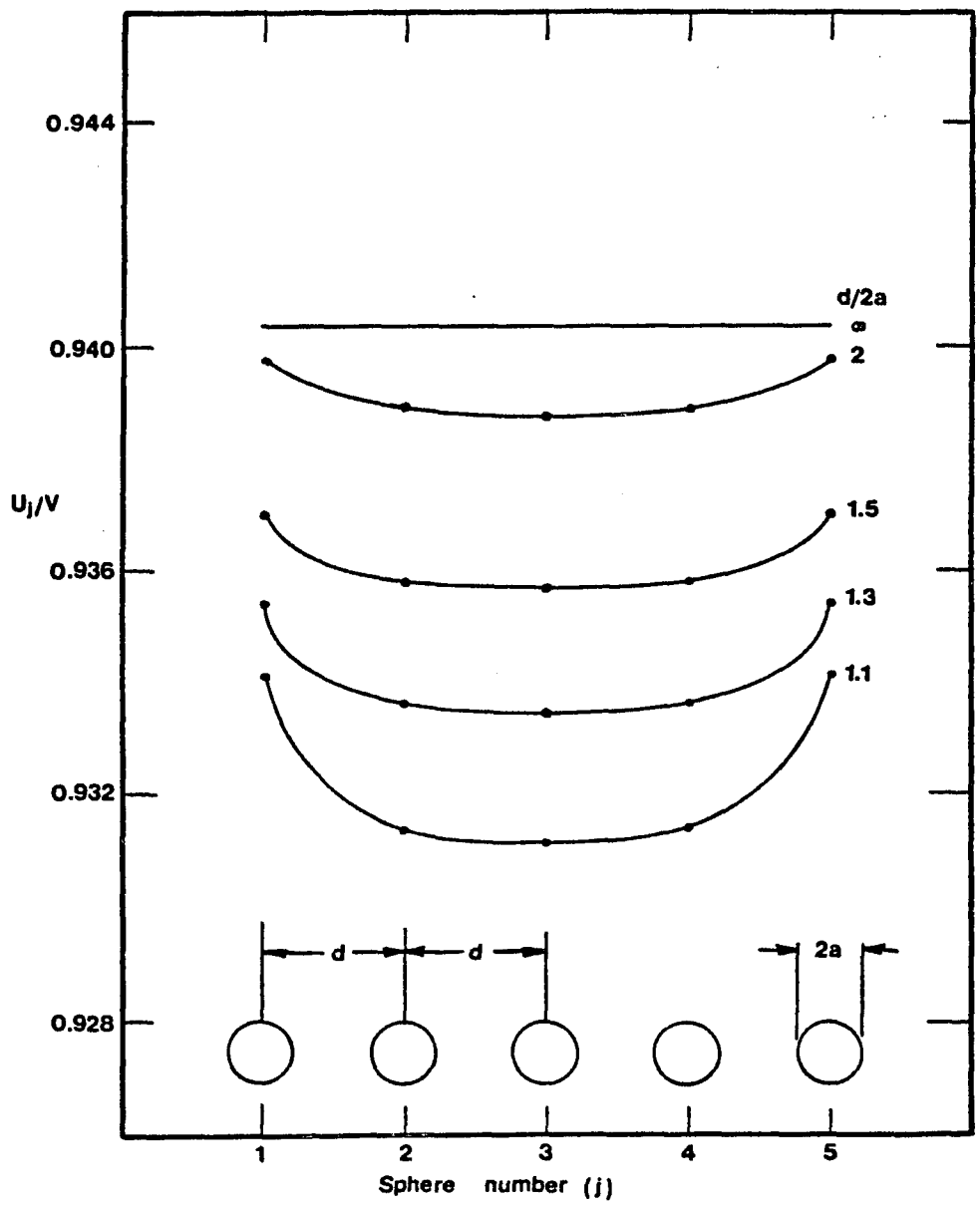

Figure 3. Cylindrically bounded motion: quasi-steady state zero-drag velocities for an equally-spaced five sphere chain of diameter ratio 0.3 and various sphere spacings (from Leichtberg, Pfeffer & Weinbaum, 1975).

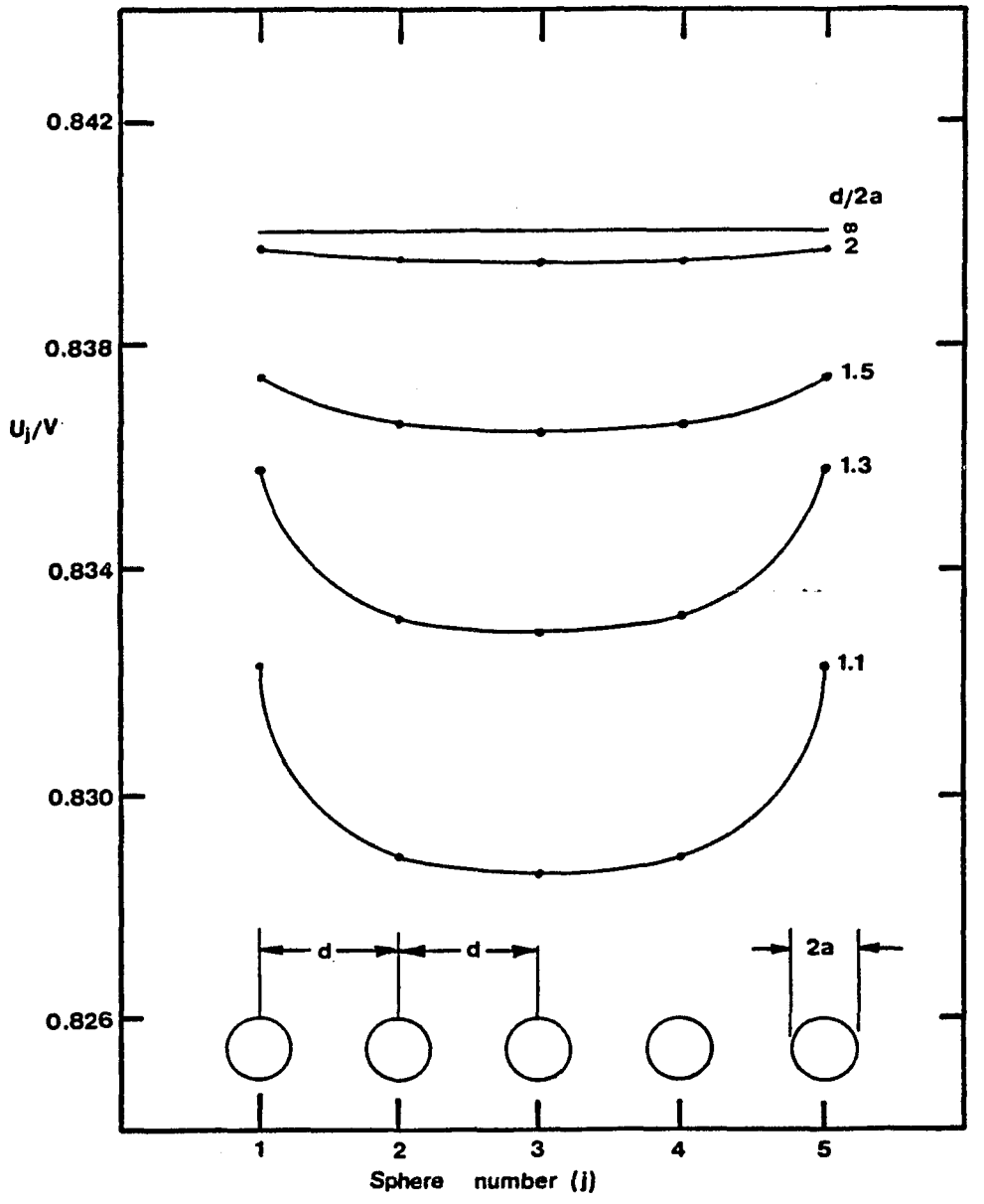

Figure 4. Cylindrically-bounded motion: quasi-steady state zero-drag velocities for an equally-spaced five sphere chain of diameter ratio 0.5 and various sphere spacings (from Leichtberg, Pfeffer & Weinbaum, 1975).

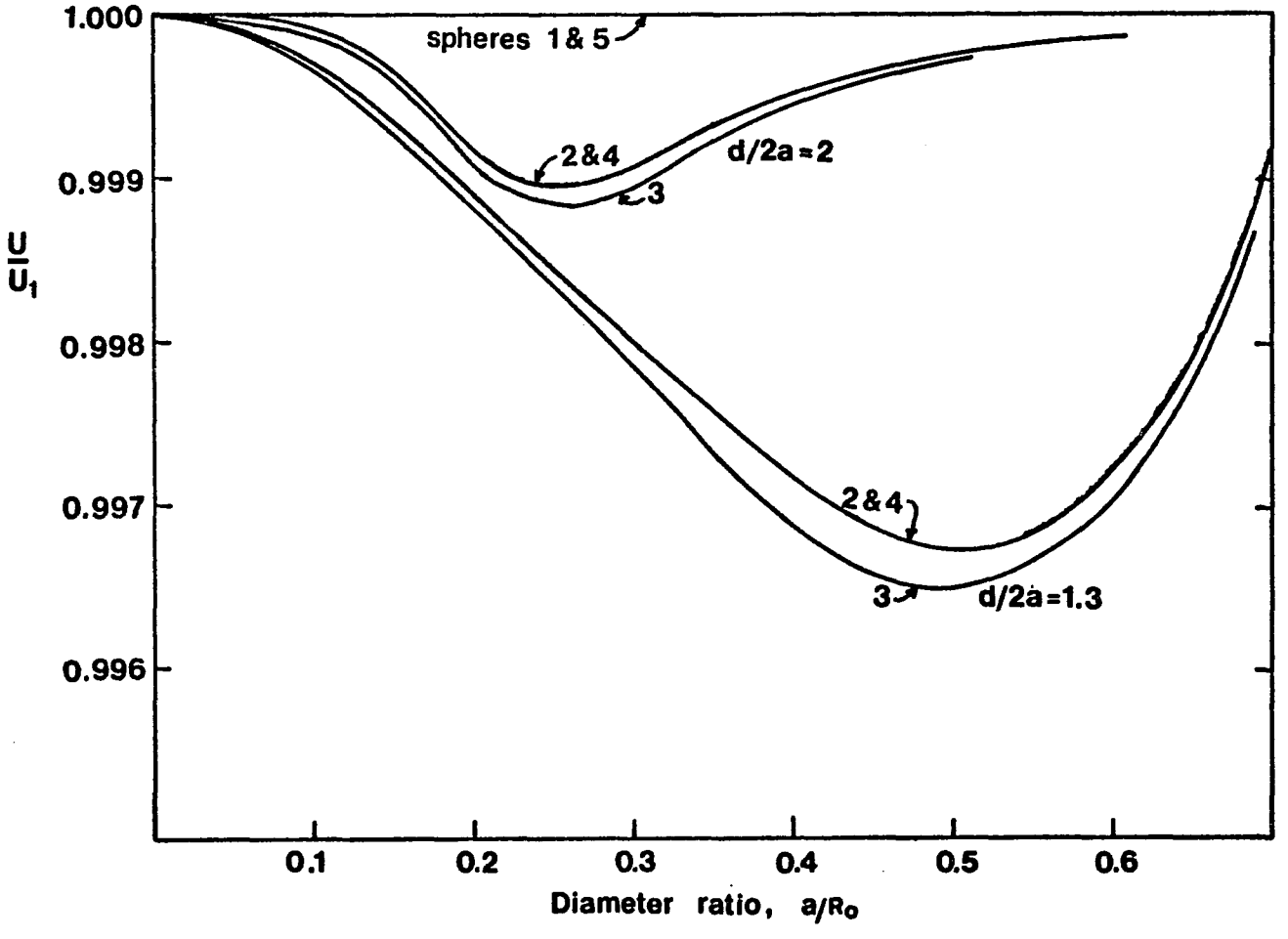

Figure 5. Sphere velocities for a five-sphere chain, normalized by the end sphere's velocity.

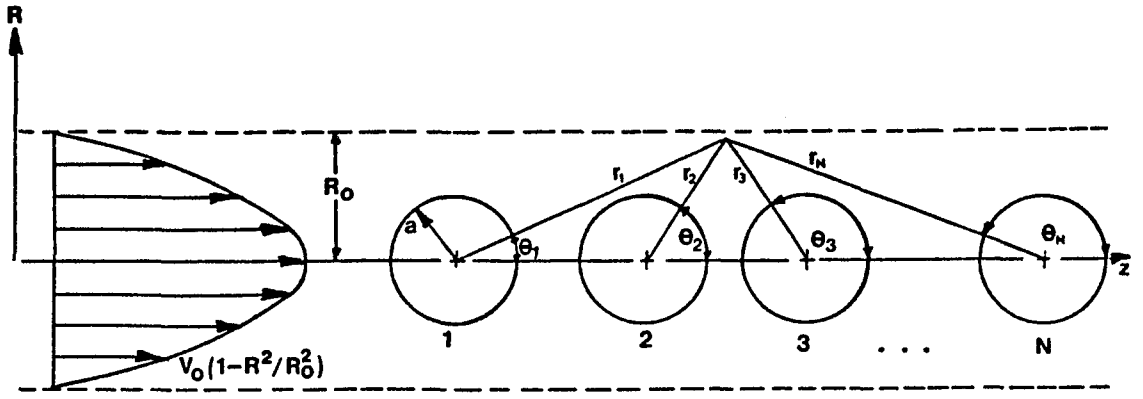

Figure 6. The system geometry.

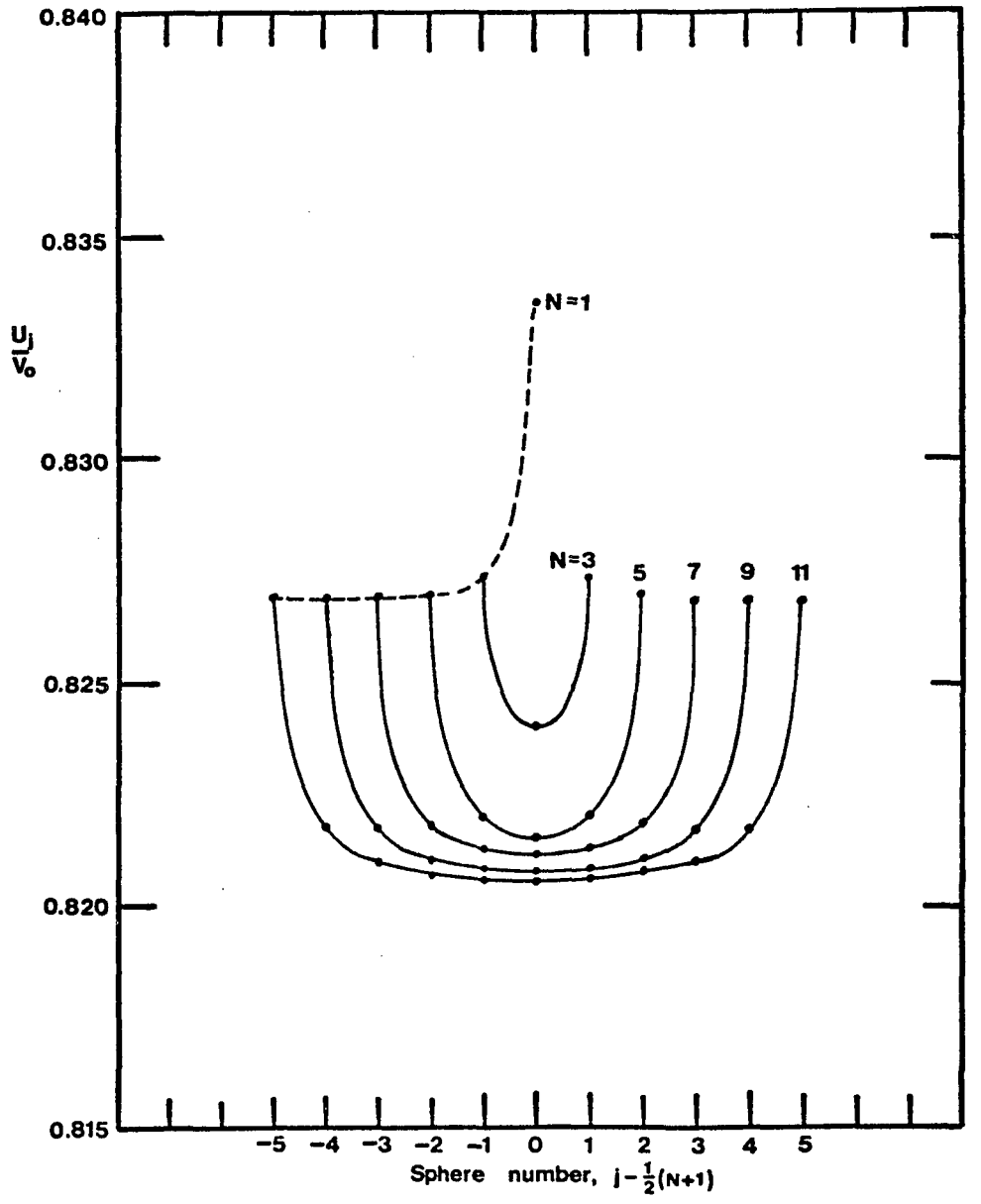

Figure 7. Sphere velocities of equally-spaced chains of various lengths. Diameter ratio $a/R_o = 0.5$; center-to-center spacing = 2 sphere diameters.

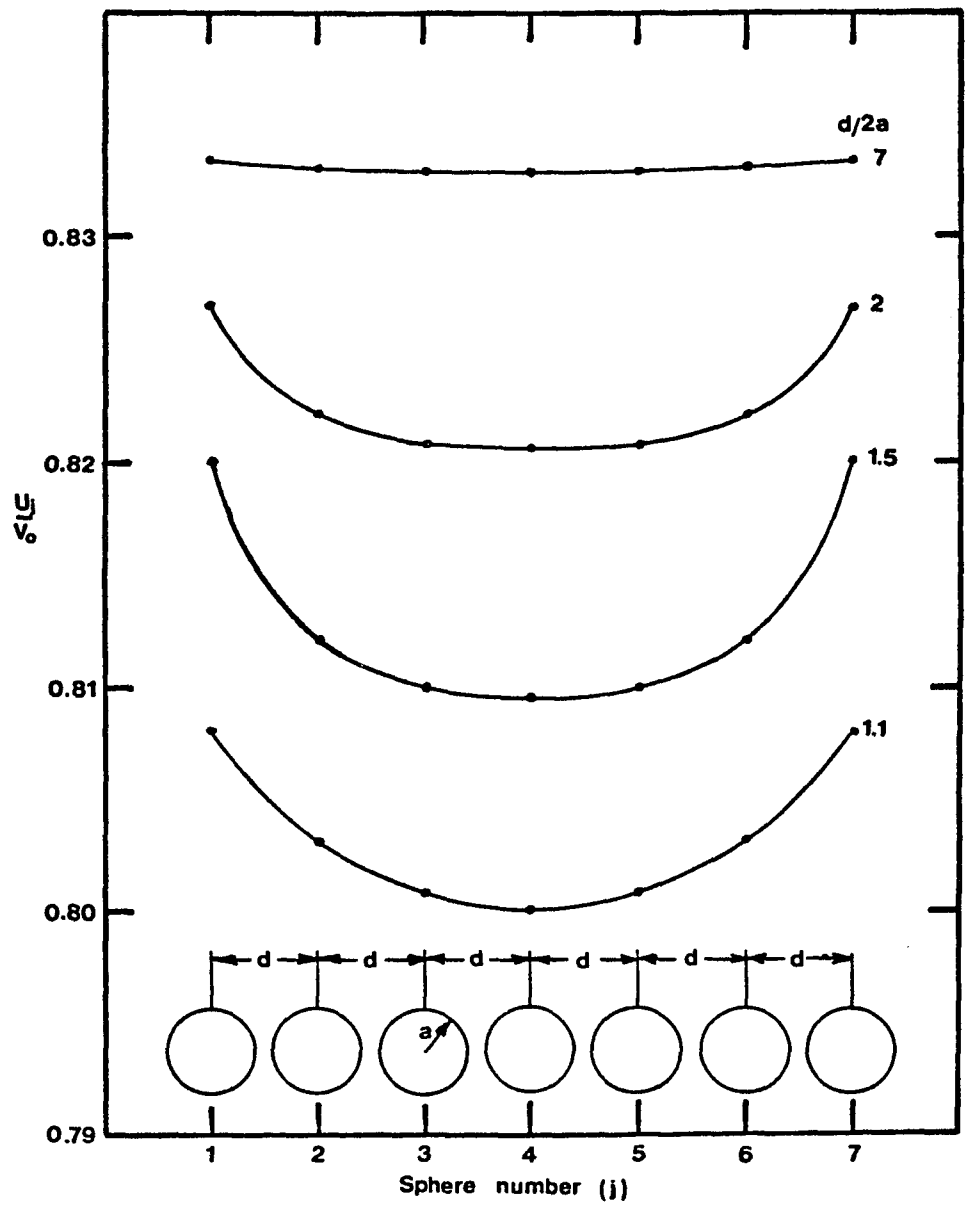

Figure 8. Sphere velocities for a chain of seven equally-spaced spheres. Diameter ratio $a/R_o = 0.5$.

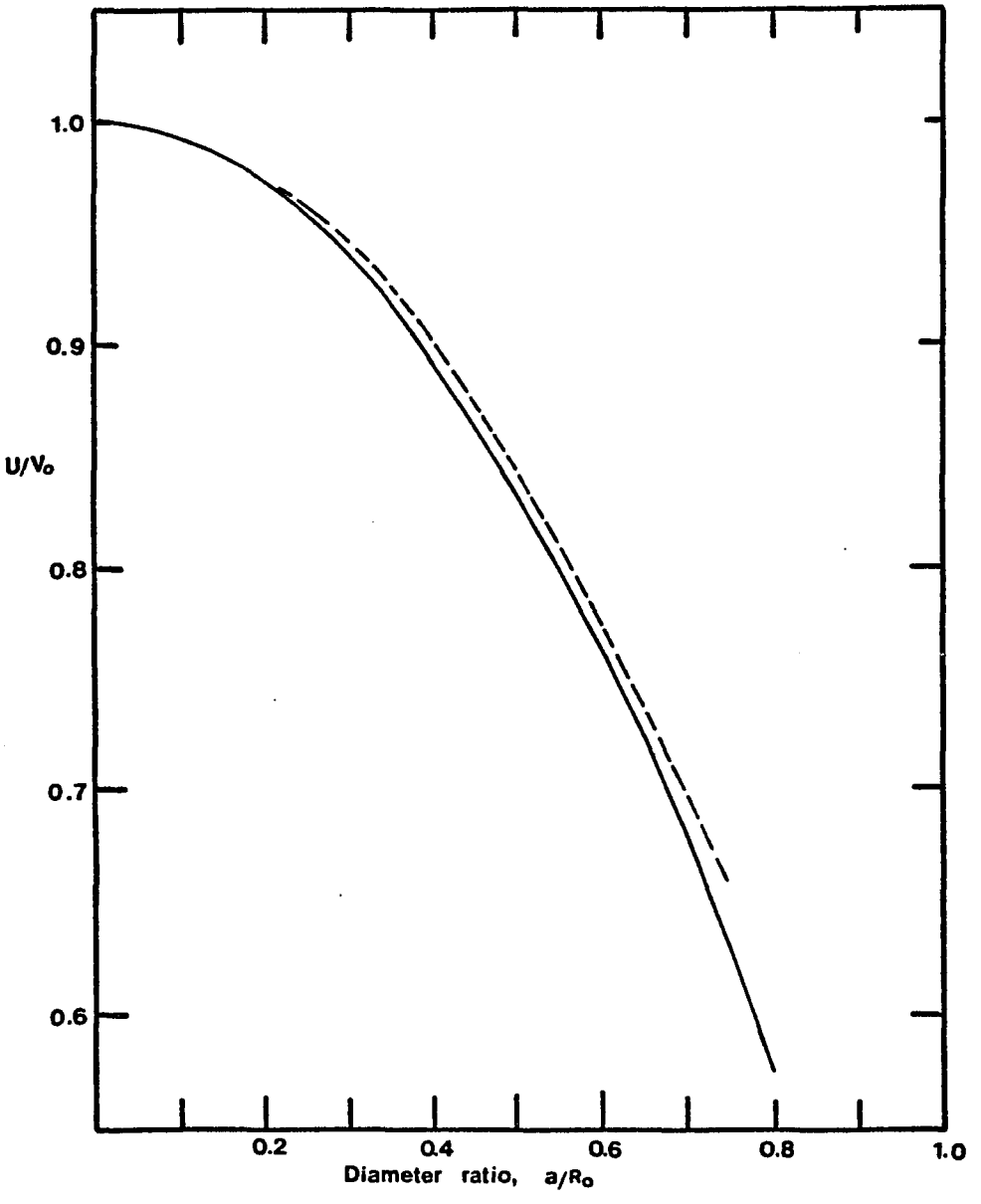

Figure 9. Zero-drag velocity vs. diameter ratio for one sphere. ——— present theory; ------ exact bounded results (from Leichtberg, Pfeffer & Weinbaum, 1975).

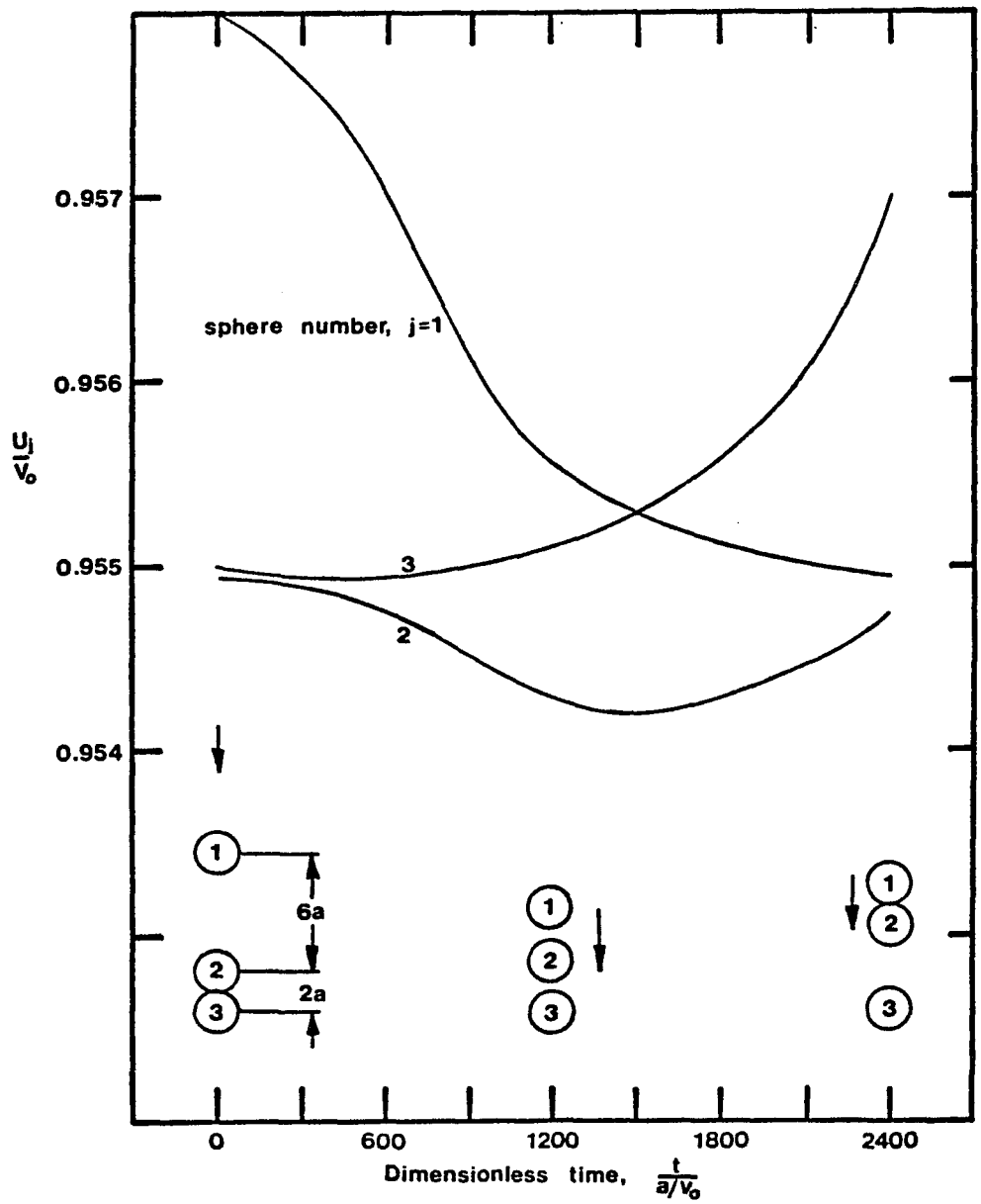

Figure 10. Velocities and configurations vs. time for a three-sphere chain. Diameter ratio $a/R_o = 0.25$.

CHAPTER V

CONCLUDING REMARKS

This study has demonstrated that it is feasible with the present generation of computers to treat the fluid-particle and particle-particle interaction problem having geometrically simple configurations. It was also shown that on the long time scale of transient interactions the Basset force plays a small but significant role, in contrast to the other acceleration-related inertia and virtual mass terms.

The application in chapter IV to blood flow was by no means an attempt to describe exactly the motion of red blood cells. Rather, the study proposed and described a long-range hydrodynamical mechanism which imparts unequal velocities to the various identical bodies of a chain of particles, such as red blood cells. This predicted behavior, together with our present understanding of the short-range forces which operate between red blood cells, provides evidence of the role played by the hydrodynamic interaction in the formation of rouleaux in the microcirculation; particularly in capillary vessels of diameters 16-80μ. The role of the short-range attraction forces is to add stability to the rouleaux.

APPENDIX

The Legendre and Gegenbauer Functions

The properties of the Legendre and Gegenbauer functions and the relationships between them will be presented.

The Legendre and Gegenbauer functions are represented by the power series,

$$P_n(x) = \frac{1}{2^n} \sum_{m=0}^{n/2} (-1)^m \binom{n}{m} \binom{2n-2m}{n} x^{n-2m} \tag{A.1}$$

$$\mathcal{Y}_n(x) = \frac{1}{\Gamma(-\frac{1}{2})} \sum_{m=0}^{n/2} (-1)^m \frac{\Gamma(n-m-\frac{1}{2})}{m!(n-2m)!} (2x)^{n-2m}, \tag{A.2}$$

where, for negative arguments,

$$P_n(-x) = (-1)^n P_n(x) \tag{A.3}$$

$$\mathcal{Y}_n(-x) = (-1)^n \mathcal{Y}_n(x). \tag{A.4}$$

These functions obey the recurrence relations

$$(n+1)P_{n+1}(x) = (2n+1)xP_n(x) - nP_{n-1}(x) \tag{A.5}$$

$$(n+1)\mathcal{Y}_{n+1}(x) = (2n-1)x\mathcal{Y}_n(x) - (n-2)\mathcal{Y}_{n-1}(x), \tag{A.6}$$

and are interrelated by

$$P_n(x) = \frac{(n+1)x\mathcal{Y}_{n+1}(x) - (n-1)\mathcal{Y}_n(x)}{1-x^2} \tag{A.7}$$

$$\mathcal{Y}_n(x) = \frac{P_{n-2}(x) - P_n(x)}{2n-1} = \frac{xP_{n-1}(x) - P_n(x)}{n-1} \tag{A.8}$$

and by their derivatives,

$$\frac{d}{dx}P_n(x) = n(n+1)\frac{\mathcal{Y}_{n+1}(x)}{1-x^2} \tag{A.9}$$

$$\frac{d^2}{dx^2}P_n(x) = n(n^2-1)\frac{\mathcal{Y}_n(x) - x\mathcal{Y}_{n+1}(x)}{(1-x^2)^2} \tag{A.10}$$

$$\frac{d}{dx}\mathcal{Y}_n(x) = -P_{n-1}(x) \tag{A.11}$$

$$\frac{d^2}{dx^2}\mathcal{Y}_n(x) = -n(n-1)\frac{\mathcal{Y}_n(x)}{1-x^2} \tag{A.12}$$

Finally, we present below the expanded form of the Legendre and Gegenbauer polynomials for orders zero through eight.

$$\begin{aligned}
P_o(x) &= 1 \\
P_1(x) &= x \\
P_2(x) &= \tfrac{1}{2}(3x^2-1) \\
P_3(x) &= \tfrac{1}{2}x(5x^2-3) \\
P_4(x) &= 1/8(35x^4-30x^2+3) \\
P_5(x) &= 1/8x(63x^4-70x^2+15) \\
P_6(x) &= 1/16(231x^6-315x^4+105x^2-5) \\
P_7(x) &= 1/16x(429x^6-693x^4+315x^2-35) \\
P_8(x) &= 1/128(6435x^8-12012x^6+6930x^4-1260x^2+35)
\end{aligned} \tag{A.13}$$

$$
\begin{aligned}
\mathcal{J}_0(x) &= 1 \\
\mathcal{J}_1(x) &= -x \\
\mathcal{J}_2(x) &= \tfrac{1}{2}(1-x^2) \\
\mathcal{J}_3(x) &= \tfrac{1}{2}x(1-x^2) \\
\mathcal{J}_4(x) &= 1/8\,(5x^2-1)\,(1-x^2) \\
\mathcal{J}_5(x) &= 1/8x\,(7x^2-3)\,(1-x^2) \\
\mathcal{J}_6(x) &= 1/16\,(21x^4-14x^2+1)\,(1-x^2) \\
\mathcal{J}_7(x) &= 1/16x\,(33x^4-30x^2+5)\,(1-x^2) \\
\mathcal{J}_8(x) &= 1/128\,(429x^6-495x^4+135x^2-5)\,(1-x^2)
\end{aligned}
\qquad \text{(A.14)}
$$

VITA

Sam Leichtberg was born in Tel Aviv, Israel on November 11, 1946 and immigrated to the United States on August 1, 1958. He attended the City College of New York where he received his Bachelor's Degree in Mechanical Engineering (1970) and his Master's Degree in Mechanical Engineering (1971). The author held an NDEA Title IV Graduate Fellowship at City College (1973-74) where he was engaged in Doctoral research. Since July, 1974, the author has held a position at Pratt & Whitney Aircraft. Sam Leichtberg is married to Judith Weiss, has one child and lives in West Hartford, Connecticut.